X-ray Studies on Short-term Softening of Black Hole Binary Swift J1753.5-0127
X線によるブラックホール連星系 Swift J1753.5-0127の短時間ソフト化の研究

Yoshikawa Akifumi
(吉川　瑛文)

Department of Physics, Tokyo University of Science
東京理科大学大学院　理学研究科　物理学専攻
E-Mail: akifumi@crab.riken.jp

High Energy Astrophysics Laboratory
理化学研究所 玉川高エネルギー宇宙物理研究室
RIKEN, 2-1 Hirosawa, Wako, Saitama 351-0198, Japan

February 20, 2015

Abstract

Black holes are the fascinating target in fundamental physics to explore the relativistic effects in strong gravitational field. The stellar mass black holes in binary system with companion stars can emit photons by releasing the gravitational energy of the accreting matter from the companion stars to the black holes. The accretion disks, which are formed around black holes with accreting material, are heated by the friction of falling material up to 10^{6-7} K, emitting X-ray at the inner most region, i.e. the vicinity of the black holes. Thus, the X-ray observations of the black holes are the proper tool to investigate the gravitational effects.

The stellar mass black hole binary Swift J1753.5–0127, which was discovered by the *Swift* satellite in 2005, showed a few times of short-term flux variation characterized by about 20 days dips in the 15–50 keV energy band. We investigated the origin of this short-term variation by using the *MAXI* and *Swift* observation data. The X-ray fluxes in the energy between 0.7 and 50 keV have been continuously monitored since July, 2009 by *MAXI* and *Swift*. In the 0.7–1.7 keV light curve, we discovered the increase of flux in the short-term variation though the 15–50 keV flux decreased. This implies that the short-term variation originated in the state change of the black hole rather than the eclipse reported in a previous study.

The X-ray spectra observed in a short-term variation period can be reproduced by a multi-color disk black-body and its Comptonized components. The temperatures ($T_{\rm in}$) and energy fluxes of the disk black-body components ($F_{\rm disk}$) changed from 0.48 to 0.2 keV and from 4.8×10^{-9} to 2.2×10^{-9} erg s^{-1} cm^{-2}, respectively. The derived inner most radius of the accretion disk ($R_{\rm in}$) from $T_{\rm in}$ and $F_{\rm disk}$ at the peak of the short-term variation is closest to the black hole, while that at the end of the variation is far. The data showed $F_{\rm disk} \propto T_{\rm in}^{0.97\pm0.02}$, which imply that $R_{\rm in}$ changed during the short-term variation. We conclude that the short-term variation originated in the state transition from low/hard state to high/soft-like state immediately followed by the opposite transition.

Contents

List of Figures

List of Tables

Chapter 1

INTRODUCTION

Black holes (BHs) are the fascinating target in fundamental physics. Schwarzshild (1916) derived the first concept of the BHs as a solution of Einstein's equation of gravitational field. The solution implies a characteristic region from which even photons cannot escape. This was the beginning of the BH studies. For a long time, the BH was just one of the solution of Einstein's equation but no substance. Wheeler (1967) proved that the event horizon, which even photons cannot escape, could be formed on the gravitational collapse of dying stars. He gave the name "Black Hole" to the region inside the event horizon. More than five decades were needed to develop observational instruments to get evidence of the BH. Oda (1971) discovered that the fast variation in the energy flux of the brightest X-ray source in the constellation Cygnus, concluding that the millisecond variation came from the BH. The study of the BH is one of the most challenging issues in high energy astrophysics to investigate phenomena in extreme gravitation.

Today, the BHs are generally classified into two categories: stellar mass BHs and massive BHs. The mass of the stellar mass BHs and massive BHs are several times and more than 10^6 times of the solar mass, respectively. Almost all galaxies contain the massive BHs in their center. On the other hand, there are a number of the stellar mass BHs in galaxies. An isolate stellar mass BH cannot emit any electromagnetic wave. A few stellar mass BHs compose a binary system with companion stars and photons can be emitted by the release of the gravitational energy of the material accreted from the companion star to the BH. The material rotates around the BH with Keplerian motion until falling to three times of the Schwarzchild radius ($R_{\rm s} = 2GM/c^2$) and forms an accretion disk. $R_{\rm s}$ is about 3 km for the BH weighting one solar mass.

The gravitational energy of the accreting material converts to the thermal energy of the accretion disk as follows. The rotation velocity of Keparian motion of falling material depends on the radius from BH.The velocity difference between neighboring materials with different radii heats the materials by friction. According to the virial theorem, a half of the released gravitational energy must convert to the kinetic energy and the rest of the energy could be the thermal energy. In the most inner region of the accretion disk, the gas can be heated up to 10^{6-7} K, emitting the X-ray photons. This is why the X-ray observations are the best to investigate BHs and the relativistic effect around them.

The X-ray spectrum below 3 keV can be described by the black-body emission from the accretion disk. The X-ray spectrum above 3 keV can be described by the inverse-Compton emission of a part of the black-body photons in the plasma ($\sim 10^{8-9}$ K) around the disk. The X-ray spectrum are classified into two categories: the high/soft and low/hard states. During the high/soft state the black-body emission dominates in the X-ray spectrum. On the other hand, during the low/hard state the inverse-Compton emission dominates. In BH binaries systems,

the state transitions between the low/hard and high/soft states within several hundreds days have been observed. Recently, instruments for the X-ray observations have been improved and the short-term variation (order of several days) have been able to be observed.

Swift J1753.5–0127 is a BH binary discovered by the *Swift* satellite in 2005, keeping the low/hard state from its discovery and state change has not been reported. In 2011, about 90% decreases in the X-ray flux between 15 and 50 keV energy band were observed, lasting about 20 days (short-term variation). Shaw et al. (2013) reported that the short-term variation due to an eclipse was feasible.However the eclipse hypothesis has not been proved because they analyzed the data only above 2 keV. In this thesis, we pursue the origin of the short-term variation observed in the BH binary Swift J1753.5–0127.

This thesis is composed of 7 chapters. In chapter 2, we review the black hole binaries and X-ray observations. In chapter 3, we review the observations of the black hole binary Swift J1753.5–0127 which is a target object of this thesis. In chapter 4, the instruments onboard *MAXI* and *Swift* are described. In chapter 5, we analyze the data of Swift J1753.5–0127 during the short-term variation.In chapter 6, we will discuss the results of the Swift J1753.5–0127 analysis. In chapter 7, we conclude this work.

Chapter 2

REVIEW OF BLACK HOLES

2.1 The basic concept of black hole

Schwarzchild derived the first basic concept of black hole (hereafter BH) from Einstein's equation for the theory of general relativity. He described the gravitational field around a spherical mass. The solution given from the general relativity implied a characteristic region from which even photons cannot escape and the region is generally called BH. The photons must go straight ahead in space-time, but if the space-time is bent by gravity the photon's trajectory seems to be bent. When the gravity is larger enough the photons cannot escape from the region. This is the birth of the concept of the BHs.

The gravitational force ($F_{\rm g}$) can be described by using the classic Newtonian mechanics as

$$F_{\rm g} = m \cdot \frac{GM}{r^2}. \tag{2.1}$$

M, m, r, G are the mass of the object which makes the gravitational potential, the mass of the object which is effected by the gravity, distance between the objects, and the gravitational constant. The gravitational potential can be written by $(2GM/r)^{1/2}$. If m is put at an infinite distance from the M object, the objects get to light speed (c) near the M object, because the potential can be strong in the local minimum around the region ($r = 0$). The Schwarzschild radius ($R_{\rm s}$), where the velocity of m reaches c can be described as

$$R_{\rm s} = \frac{2GM}{c^2}. \tag{2.2}$$

In the vicinity of the BH, general-relativistic effects are essential; e.g., the gravitational redshifts, and bending of light, because the space-time of around $R_{\rm s}$ cannot be solved by the classical Newtonian. Schwarzschild solved the space-time of around $R_{\rm s}$, assuming point mass and uniformly space, as follows,

$$\mathrm{d}\tau = \left(1 - \frac{R_{\rm s}}{r}\right)^{1/2} \mathrm{d}t. \tag{2.3}$$

d τ and d t are the time effected by general-relativistic and the Newtonian time.

2.2 The observational study of black hole binaries

2.2.1 The energy radiation from the vicinity of black hole

Alone BH cannot emit any energy. When gas falls on a compact object, some of the gravitational energy of the gas is released. This is the mass accretion process in astronomy. The accreting matter must have finite angular momentum and it is expected to form a disk around the BH, called an accretion disk which releases the gravitational energy as thermal emission.

For instance, suppose one electron of mass $m_{\rm e}$ gravitationally falls to a BH from infinity, then the gravitational energy released is approximately given as $Gm_{\rm e}M/r = m_{\rm e}c^2 \cdot (R_{\rm g}/r)$, which is comparable to the electron rest-mass energy of $m_{\rm e}c^2 \sim 100$ keV unless r is much larger than the gravitational radius $R_{\rm g}$ (=1/2R_s). Consequently, the accreting matter is expected to emit mainly in the X-ray band. X-ray observations provide the most powerful tool for discovering and studying accreting BHs.

2.2.2 The first evidence

The most famous, proto-type black hole candidate is Cygnus X-1 (Hereafter Cyg X-1) which is one of the handful X-ray sources discovered by the X-ray observation of *Uhuru*. *Uhuru* was the world's first X-ray satellite and found rapid and intense variability from the source as shown in figure 2.1. Oda et al. (1971) wrote the first paper to suggest that Cyg X-1 could contain a BH on the basis of its peculiar characteristics including in particular the rapid variability on time scales of a few hundred seconds down to milliseconds. The variability indicates that the object has an extremely small size, less than $c\delta t \sim 300$ km, and the energy source is probably mass accretion. Based on these observations results, they argued that
The existence of variations in intensity by a factor of 2 in 800 seconds requires that at least 50 percent of the emission occur in a region smaller than 1 a.u. The existence of persistent 70-ms pulsations compels us to invoke stellar rotation as the underlying timing mechanism, almost independently of whether these pulsations remain rigorously periodic over very long time or persist only for several tens of second time. Further, the rapid rotational period requires that the rotating star be a collapsed object, such as a neutron star or a black hole (Oda et al., 1971).

Webster et al. (1972) and Bolton et al. (1972) discovered the optical counterpart of Cyg X-1, the supergiant HD226868, which lay (prominently) in the X-ray error box of Cyg X-1. The star forms a binary system, with an optically invisible massive body that is likely to be the X-ray emitter. Employing the measured orbital period of $P = 5.6$ days and the Doppler velocity of of $A = 75$ km s^{-1} of HD 226868, the orbital mass-function of the Cyg X-1 system was then determined as

$$f(M) = \frac{M_{\rm X}^3 \sin^3 i}{(M_{\rm X} + M_{\rm c})^2} = \frac{A^3 P}{2\pi G}, \tag{2.4}$$

where $M_{\rm X}$ and $M_{\rm c}$ are the masses of the compact object and the companion star, respectively, while i is the inclination angle of the system. The mass function can be estimated to be 0.25 $M_\odot$. With a help of the optically estimated inclination of ~ 30 °, and the companion mass $M_{\rm c}$ $\sim 30\ M_\odot$ also estimated optically, this relation yields a compact-object mass of $M_{\rm X} \geq 9.5\ M_\odot$ (Paczynski et al., 1974). Since this exceeds the upper mass limit for a neutron star ($\sim 3.2\ M_\odot$; e.g., Kalogera & Baym, 1996) the X-ray emitter in Cyg X-1 has become to be regarded as a BH.

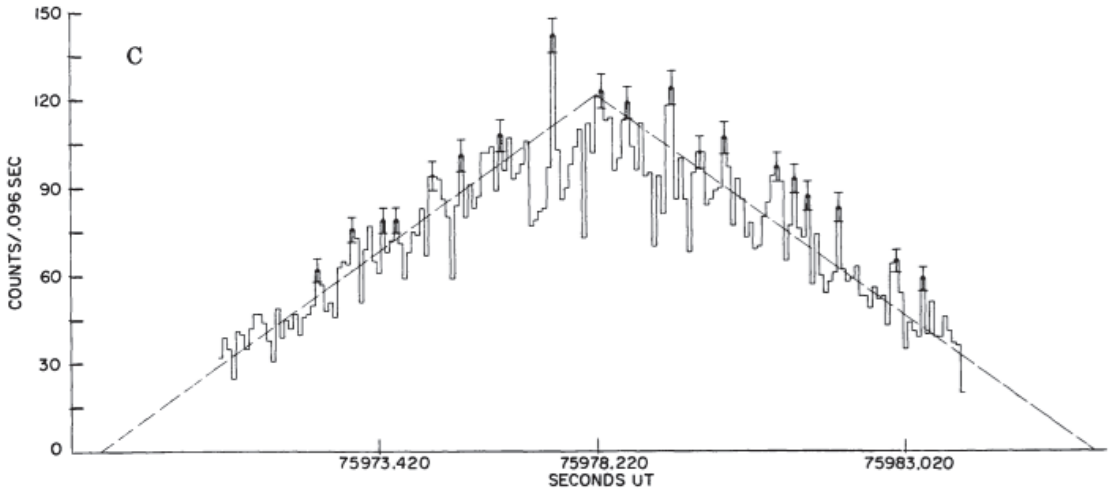

Figure 2.1: The X-ray light curve of Cyg X-1 for 10 seconds with a bin size of 0.096 seconds, taken with the *Uhuru* satellite on 1971 March 6. The dashed lines are the time-dependent detector response (Oda et al., 1971).

2.3 Black hole binary systems

The X-ray radiation from a BH is controlled by the mass accretion process. The source material for the accretion process is the companion star of a binary system. A binary system is a system of two objects in the universe (usually stars) which are so close that their gravitational interaction causes them to orbit about a common center of mass. A binary system with a BH is called a black hole binary (BHB) system. A Roche lobe is the region of space around a star in a binary system within which orbiting material is gravitationally bound to that star. A three-dimensional representation of the Roche potential of a binary star with mass ratio $M_2/M_1 = 0.25$ is shown in figure 2.2 (a) and (b).

There are two major classes of binary system, separated by the mass of companion star. A high-mass X-ray binary (HMXB) is close binary system containing a high mass companion star ($\geq$ 10 $M_\odot$), while the mass of companion stars in low-mass X-ray binary (LMXB) is lower than 5 $M_\odot$. The number of LMXBs reported so far is larger than that of HMXBs, which is presumably believed due to the longer lifetime of lighter companion stars. Table 2.1 summarizes examples of BHs in HMXB and LMXBs systems. Figure 2.3 shows a schematic sketch of 16 black hole binaries in the Milky Way with reasonably accurate dynamical data. According to X-ray observations over the last four decades, BH in HMXB is in many cases persistently bright, while that in LMXB is transient (Remillard & McClintock, 2006). Examples of the light curves of a LMXB and HMXB are shown in Figure 2.4.

The mass accretion onto the BH in LMXBs, is believed to be provided by ”Roche lobe overflow” from a relatively light companion star. The companion star in the LMXB fills the ”Roche lobe”, which is an equipotential surface formed by the gravity field of each object. The two gravitational fields have a contact point at the Lagrangian point 1 (L_1). The companion star transfers material to the compact object though L_1 as shown in figure 2.2. This is called the Roche lobe overflow model as shown in figure 2.5. They are too faint to observe in the X-ray band for most of the time, but occasionally strong X-ray outbursts are observed. The interval

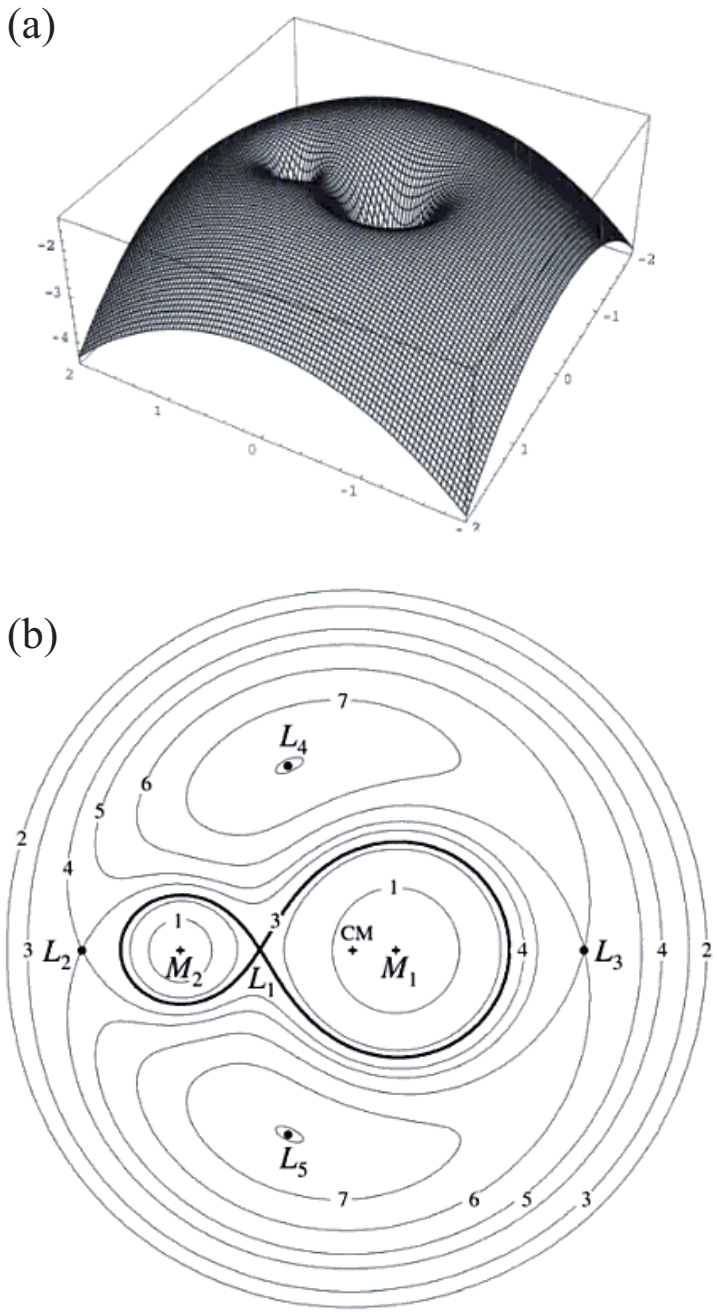

Figure 2.2: (a) The surface of the Roche potential for a binary system with mass ratio M_2/M_1 = 0.25. The more massive star produces the larger dip on the surface. (b) The Roche lobe for the same binary system as (a). The center of mass and Lagrange points L_1–L_5 are plotted in the figure. The solid lines show the equipotential 1–7, and the equipotential 3 shows the Roche lobe. The inner Lagrange point (L_1) is formed at the cross of the two Roche lobes. These figures are taken from (Frank et al., 2002).

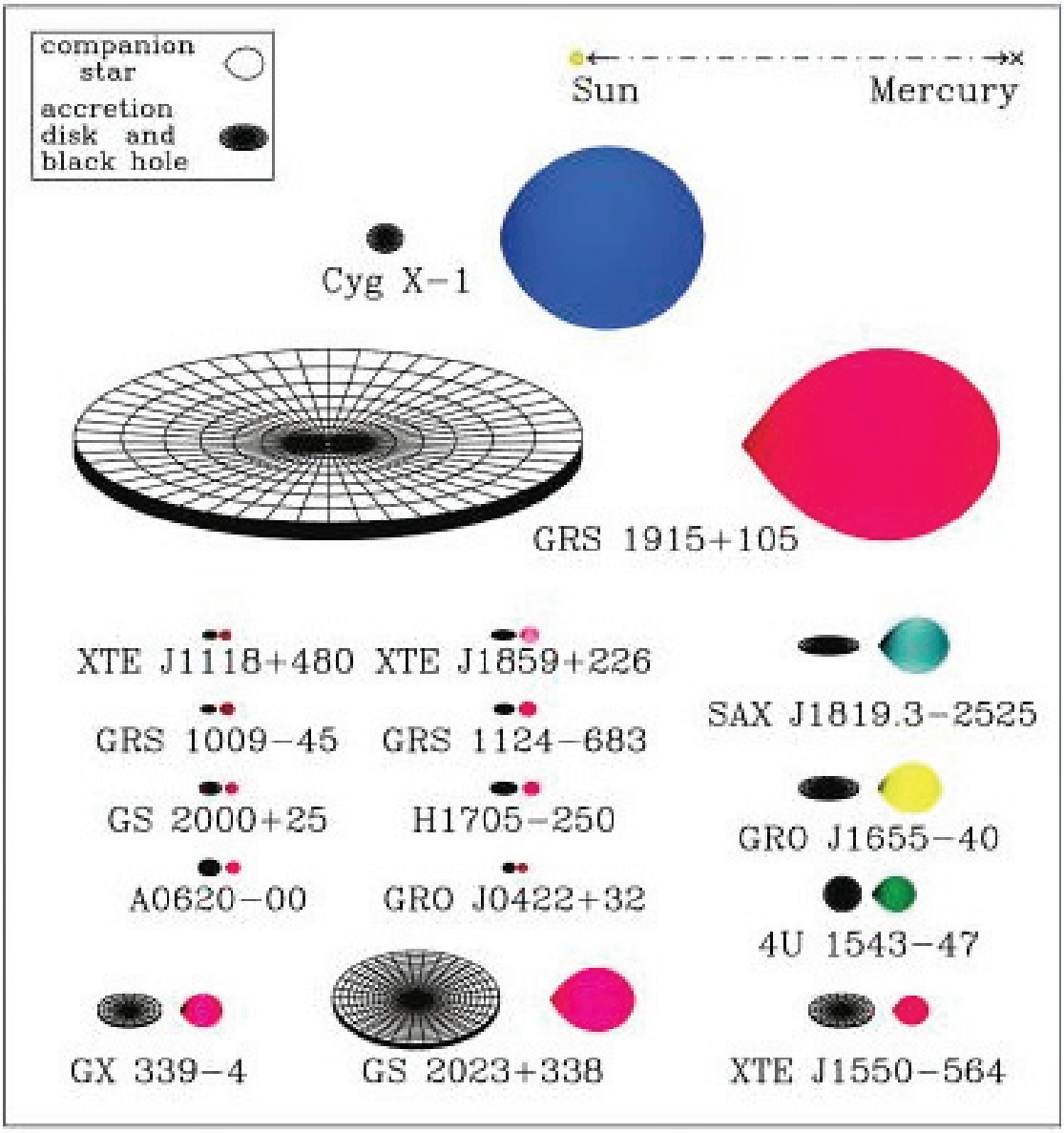

Figure 2.3: Scale drawing of various black hole binary systems (Remillard & McClintock, 2006).

Table 2.1: The examples of black holes binaries (Kato et al., 2008).

Source	M_x [M_{sun}]	P [d]	$f(M)$ [M_{sun}]	d [kpc]	Companion
HMXBs					
Cyg X-1	> 9.5	5.6	0.244±0.005	2.0±0.1	O9.7Iab
SS 433	∼9.0	13.1	3.0±0.6	5.0±0.5	A5/A7I
LMC X-3	5.9–9.2	1.70	2.3±0.3	50±2.3	B3V
LMC X-1	4.0–10.0	4.23	0.14±0.05	50±2.3	O7III
LMXBs					
GRO J0422+32	3.2–13.2	0.21	1.19±0.02	2.6±0.7	M2V
A 0620-003	8.7–12.9	0.325	2.72±0.06	1.2±0.1	K4V
1009-45	6.3–8.0	0.325	3.17±0.12	5.0±1.3	K7/M0V
1118+480	6.5–7.2	0.17	6.1±0.3	1.8±0.5	K5/M0V
GS 1124-684	6.5–9.2	0.43	3.01±0.15	5±1.3	K3/K5V
1543+475	7.4–11.4	1.13	0.25±0.01	7.5±0.5	A2V
1550-564	8.4–10.8	1.54	6.86±0.71	5.3±2.3	G8/K8IV
GRO J1655-40	6.0–6.6	2.62	2.73±0.09	3.2±0.2	F3/F5IV
H1705-25	5.6–8.3	0.52	4.86±0.13	8±2	K3/7V
1819-25	6.8–7.4	2.82	3.13±0.13	7.4±12.3	B9III
GRS 1915+105	> 10.0	33.5	9.5±3.0	11–12	K/MIII
GS 2000+25	7.1–7.8	0.35	5.01±0.12	2.7±0.7	K3/K7V
GS 2023+338	10.1–13.4	6.47	6.08±0.06	2.2–3.7	K0III

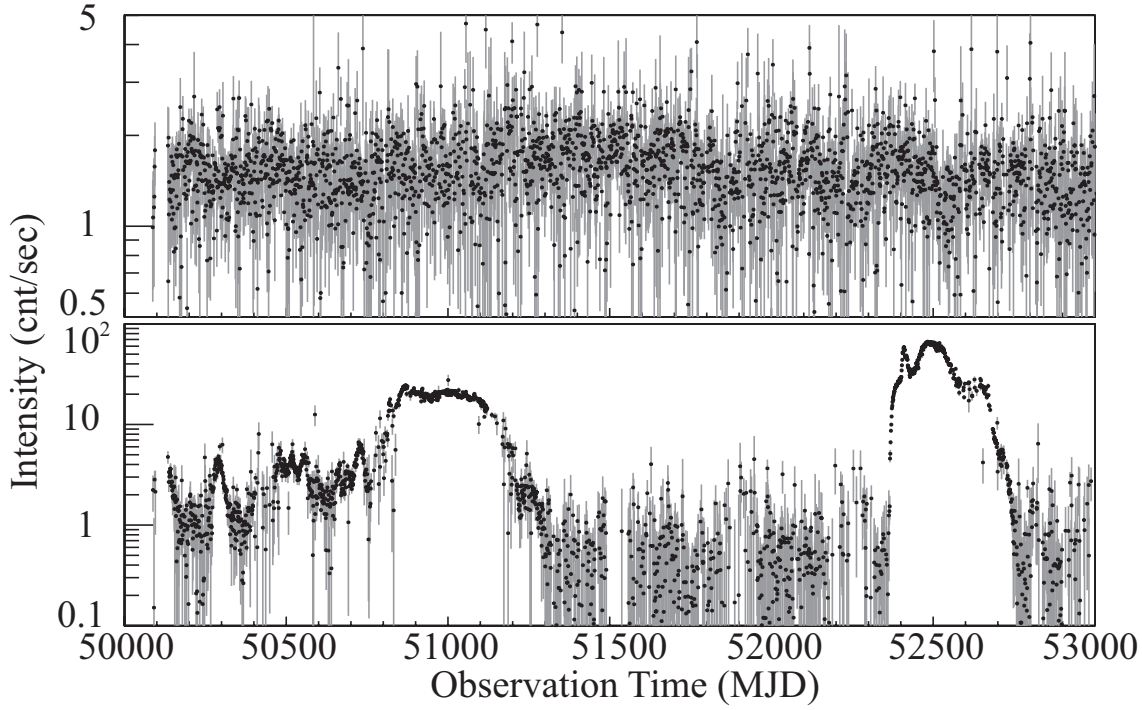

Figure 2.4: (Top) Light curves of the HMXB LMC X-1 and (bottom) the LMXB GX 339-4 in the energy range of 1.2–15 keV. The data were obtained by the *RXTE* satellite.

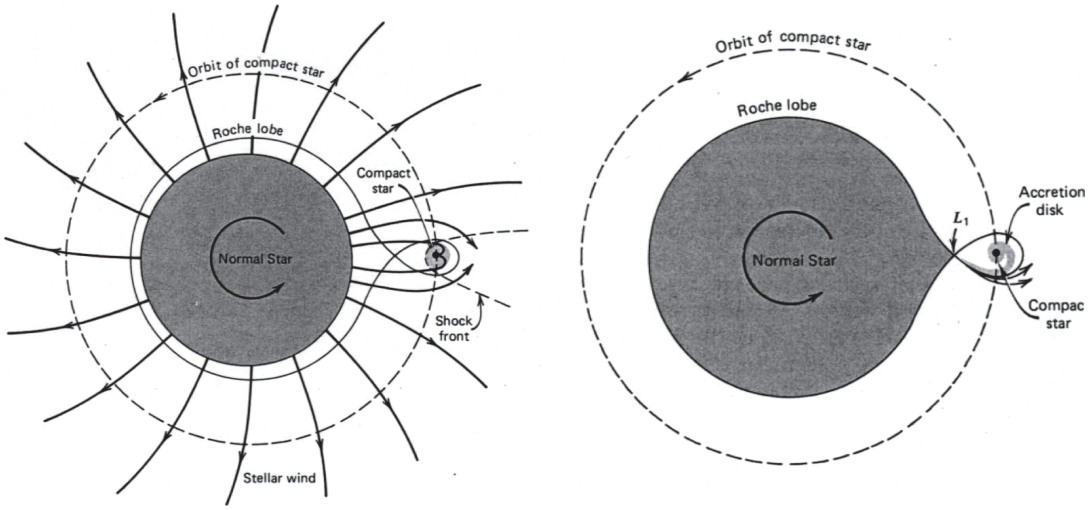

Figure 2.5: (Left) The schematic view of mass accretion in HMXBs and (right) that in LMXBs. The mass accretion in HMXBs is controlled by the stellar wind from the companion star.

between the outburst is random from a few months to tens of years or more. The outburst is believed to be triggered by mass accretion from the low mass companion star. There are known to be a few sources that do not follow the empirical trend (1E1740.7–2942:Cui et al., 1997, Ramadevi & Seetha, 2007 and GRS 1758–258: Kuznetsov et al., 1999), though their properties have not yet been studied in detail due to lack of observations.

The mass transfer mechanism of HMXBs is different from that of LMXBs and is more complex than that of LMXBs. Mass accretion onto a BH in the HMXBs is provided by the stellar wind from the massive companion star as shown in figure 2.5. Since high mass stars usually have a strong stellar wind, the material can be transferred to the compact object without filling the Roche lobe. The light curve of HMXB is persistent as shown in figure 2.4 but some HMXB sources are transient. This is called the wind-fed model. Only a few BHB belongs to this group (e.g., Cyg X-1, LMC X-1, and X-3).

2.4 Characteristics of an accretion disk

2.4.1 Disk formation

Material from a companion star is transferred into a BH, forming an accretion disk. The accretion disk is a system of energy radiation, releasing the gravitational energy of accreting material to thermal energy by its viscosity. The size of the disk is on the order of the Sun's radius (10^{8-9} m) and its thickness at 10^2 R_s from the center is 0.1 R_s.

The angular velocity (v_K), the angular velocity (ω_K) and the angular momentum (l_K) of the Keplerian disk motion are written as

$$v_K = \sqrt{GM/r}, \tag{2.5}$$

$$\omega_K = \sqrt{\frac{GM}{r^3}}, \tag{2.6}$$

$$l_{\rm K} = rv_{\rm K} = \sqrt{GMr}, \tag{2.7}$$

where r is the radius of the disk. When the accreting material rotating around a BH falls from an outer region to the event horizon ($R_{\rm in}$), the inner material faster in velocity accelerates the slower outer material by viscosity. The difference of the velocity depends on the radius and the viscosity heats up the accreting material. Thus, the matter in the disk is heated up and begin to radiate photons, transporting the angular momentum from the inner region to the outer region.

2.4.2 Inner most stable circular orbit (ISCO)

In the Newtonian case, the effective potential $V_{\rm N}$ of the motion of a particle around a BH can be written as

$$\frac{V_{\rm N}(r)}{m} = -\frac{M}{r} + \frac{(J/m)^2}{2r^2}, \tag{2.8}$$

where $J = mr^2/c(\mathrm{d}\phi/\mathrm{d}\tau)$ is the angular momentum of the particle, $\mathrm{d}\phi/\mathrm{d}\tau$ is the angular velocity, τ is the proper time, r is the radius, and m is the particle mass. M is defined as $GM_{\rm BH}/c^2$ where the $M_{\rm BH}$ is the mass of BH. Henceforth, M is used as the system of unit with $G = C = 1$. The effective potential leads to the classical Kepler motion. Figure 2.6 shows the effective Newtonian and Shwarzchild potentials with $J = 4$. The effective Newtonian potential tells us that the particle cannot fall to the BH. On the other hand, the effective potential introduced by Schwarzschild ($V_{\rm S}$) is given as

$$\left(\frac{V_{\rm S}(r)}{m}\right) = \left(1 - \frac{2M}{r}\right)\left(1 + \frac{(J/m)^2}{r^2}\right) = 1 - \frac{2M}{r} + \frac{(J/m)^2}{r^2} - \frac{2M}{r^3}(J/m)^2. \tag{2.9}$$

$V_{\rm S}$ is derived from the equation 2.9 and shows possibility to fall into the BH. Figure 2.7 is the $V_{\rm S}$ for various Js, which shows that the change of $V_{\rm S}$ is due to the decrease of the angular momentum. When the J decreases below $12^{(1/2)}$, the particle cannot rotate around the BH and then falls at $r = 6M$. The J of $12^{(1/2)}$ is obtained by the calculation equation of $dV(r)/dr = d^2V(r)/d^2r$. The radius of the stable circular motion can be written as

$$r = \frac{(J/m)^2}{2M}\left[1 \pm \left(1 - \frac{12M^2}{(J/m)^2}\right)^{1/2}\right]. \tag{2.10}$$

J/m must be larger than $J/m = 12^{1/2}M$.

In the case of a standard accretion disk around non-rotating BHs, the accretion disk is truncated at an innermost disk radius ($r_{\rm in}$) which is defined as $r_{\rm in} = 3R_{\rm s}$. $r_{\rm in}$ is proportional to the BH mass and we can estimate the BH mass from a measurement of $r_{\rm in}$. The materials cannot steadily rotate around the BH ($< r_{\rm in}$) due to general relativistic effects. Thus, the radius $r_{\rm in}$ is called the inner most stable circular orbit (ISCO). Once the accreting material goes through the ISCO, the material falls immediately to the event horizon carrying its angular momentum to a BH.

There are three parameters that define the characteristics of BHs: $M_{\rm BH}$, charge ($Q_{\rm BH}$), and angular momentum ($J_{\rm BH}$). Especially, $M_{\rm BH}$ and $J_{\rm BH}$ affect the general relativity around BHs. In the case of rotating BHs, $r_{\rm in}$ for a particle orbit becomes smaller than $3r_{\rm s}$, due to an effect of the outward-directed Coriolis force. A rotating BH is called a Kerr BH and its $J_{\rm BH}$ is not equal to zero. In the real world astronomical objects are more or less spining. The angular momentum (a) of a black hole is introduced as $a = J/Mc$. Furthermore, to express the spin parameter a_*,

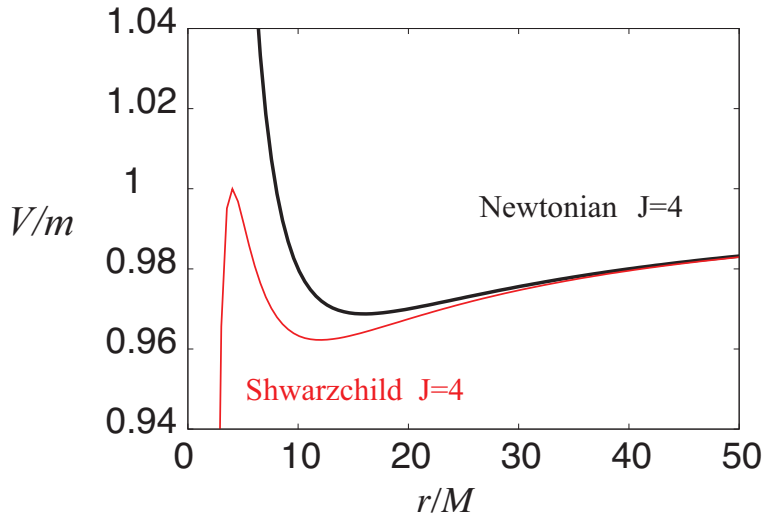

Figure 2.6: Effective Newtonian (black) and Schwarzchild (red) potentials, as a function of r for J = 4. The units of r and $V(r)$ are M, and that of J is m.

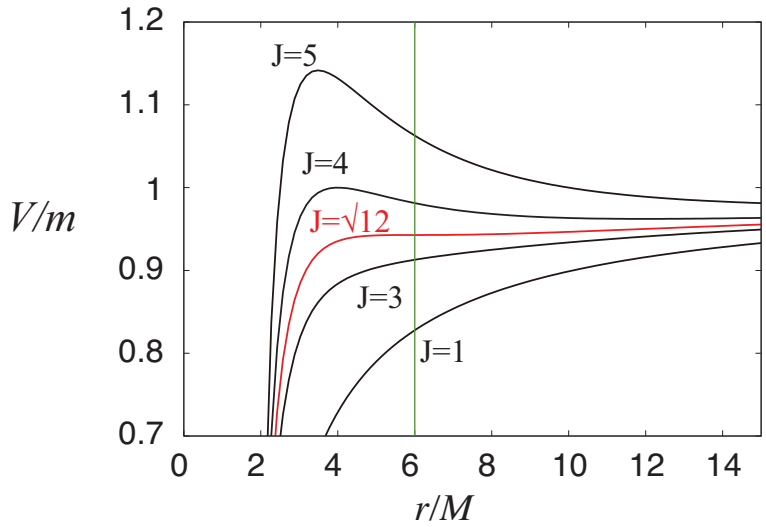

Figure 2.7: Effective Schwarzchild potentials, as a function of r for J = 1, 3, $12^{1/2}$ (red), 4, 5. The units of r and $V(r)$ are M, and that of J is m. The green line is drawn at $r = 6\,M$.

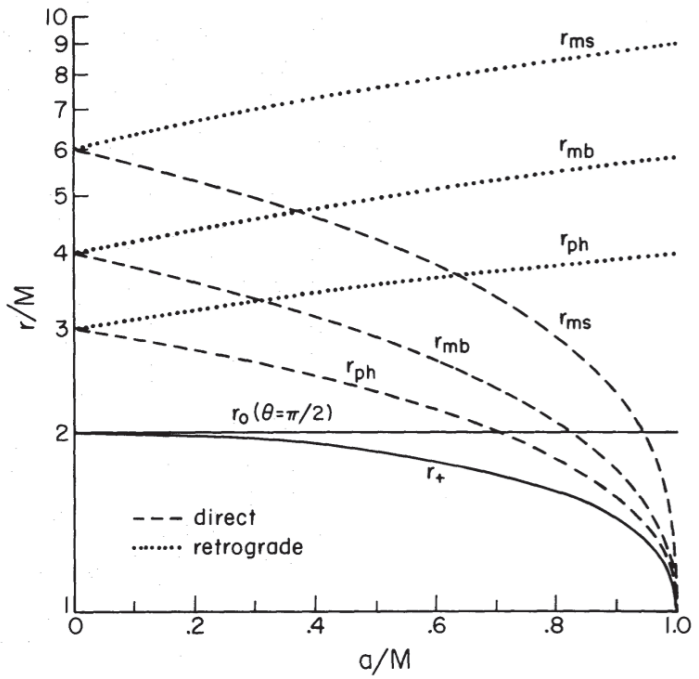

Figure 2.8: Radii of circular and equatorial orbits around a Kerr BH of mass M, as a function of the specific angular momentum a. The lines are plotted with the unit of $M \equiv GM/c^2$. Dotted and dashed curves (for direct and retrograde orbits) show the radius of the the innermost stable ($r_{\rm ms}$), innermost bound ($r_{\rm mb}$), and photon orbit ($r_{\rm ph}$). Solid curves indicate the event horizon (r_+) and the equatorial boundary of the ergosphere (r_0). The figure is taken from Bardeen et al. (1972).

a_* is defined as $a_* = c^2/GM \cdot a$. The inner radius ($r_{\rm in}$) of the accretion disk around a Kerr BH can be written as,

$$r_{\rm in} = \frac{r_{\rm g}}{2}\left(1 + \sqrt{1 - a_*^2}\right). \tag{2.11}$$

Since a_* must be non-negative and the maximum value of a is GM/c^2.

Figure 2.8 shows the radii of equatorial orbits around a Kerr BH. The faster the spin, the smaller r_{in} is. If a_* is one, $r_{\rm H}$ becomes $r_g/2$. A BH with the maximum spin value is called a maximally rotating black hole. The maximum value of a_* is believed to be 0.9998 (Kozlowski et al., 1978). For the Schwarzschild black hole ($a_* = 0$), $r_{\rm ms} = 6\,M$, while for the extreme Kerr black hole ($a_* = 1$), $r_{\rm ms} = M$ (direct orbit) or $r_{\rm ms} = 9M$ (retrograde orbit). A marginally bound circular orbit is the innermost (unstable) circular orbit. For $a_* = 0$, $r_{\rm mb} = 4M$, while for $a_* = 1$, $r_{\rm mb} = M$ (direct orbit) or $r_{\rm mb} = 5.82M$ (retrograde orbit). A photon circular orbit, which is the innermost (unstable) circular orbit. For $a_* = 0$, $r_{\rm ph} = 6M$, while for $a_* = 1$, $r_{\rm ph} = M$ (direct orbit) or $r_{\rm ph} = 4M$ (retrograde orbit).

2.4.3 Radiation energy

According to the virial theorem, the gravitational potential (V) can be written as $\langle K \rangle = 1/2\langle V \rangle$ where $\langle K \rangle$ is the average of the kinetic energy. The radiation process of the accretion disk is

thermal emission. The luminosity (L) can be expressed as,

$$L \approx \frac{1}{2}\frac{GM\dot{M}}{r_{\rm in}}. \tag{2.12}$$

Equation 2.12 is derived by the integration of the gravitational energy along the radius. The kinetic energy is believed to be carried into the ISCO. The luminosity of the accretion disk of a non-rotating BH (L_d) is $L_d = 1/12\dot{M}c^2$. L_d can be written as an efficiency (η) of the mass accretion rate ($\dot{M}$) as,

$$L_d = \eta\dot{M}c^2. \tag{2.13}$$

For a non-rotating BH, the value of η is 1/12. In the case of a maximally rotating BH, the efficiency is 0.42.

When we study accreting black holes with different M, it is convenient to normalize their luminosity to the Eddington limit. The limit is the maximum achievable luminosity of radiation, when the force of radiation acting outward is balanced by the gravitational force acting inward. The Eddington luminosity ($L_{\rm E}$) is expressed as

$$L_{\rm E} = 4\pi cGMm_{\rm H}/\sigma_{\rm T} = 1.25\times10^{39}\left(\frac{M}{10M_{\rm sun}}\right){\rm ergs}^{-1}, \tag{2.14}$$

where $\sigma_{\rm T}$ is the Thomson cross section. The critical mass-flow rate is defined as

$$\dot{M}_{\rm crit} = \dot{M}_{\rm Edd}\cdot\eta = \frac{L_{\rm E}}{c^2} = 1.40\times10^{17}\frac{M}{M_\odot}{\rm gs}^{-1}. \tag{2.15}$$

$\dot{M}_{\rm crit}$ is the critical mass-accretion rate and $\dot{M}_{\rm Edd}$ is the mass-accretion rate of the Eddinton limit. To reveal the mass-accretion rates from the X-ray flux, we usually use the ratio of bolometric luminosity to the $L_{\rm E}$.

2.5 Standard accretion disks

Many *theoretical* accretion disk models have been developed to explain the X-ray spectrum or the dramatic intensity variations. We can obtain the disk temperature ($T_{\rm disk}$), the inner radius ($r_{\rm in}$) and the disk luminosity (L) from the X-ray spectrum, assuming a model which may explain the spectrum. We refer the three standard model widely used in the study of the accretion disks: the standard disk (Shakura & Sunyaev, 1973), the radiatively inefficient accretion flow (RIAF; Yuan et al., 2003), and the slim disk (Kawaguchi et al., 2003). In particular, we focus on the standard disk model because the model can generally explain the X-ray spectrum during the high/soft state.

Figure 2.9 shows the thermal equilibria between the vertically-integrated surface density ($\sum$) and the mass accretion rate ($\dot{M}$) and summarizes the relation of those models (Abramowicz et al., 1995). The standard disk is assumed the geometry that an optically-thick and geometrically-thin disk and located at the right-bottom region. The model is optimized for the spectrum of the high/soft state when the blackbody radiation is dominant. The slim disk model is optimized for a spectrum which is close to the Eddington luminosity, for example Ultra Luminosity X-ray sources. Thus the slim disk is located at the region where $\dot{M}$ is larger than the standard disk. The model optimized for the low/hard state is the RIAF model which is located at the left curve. In

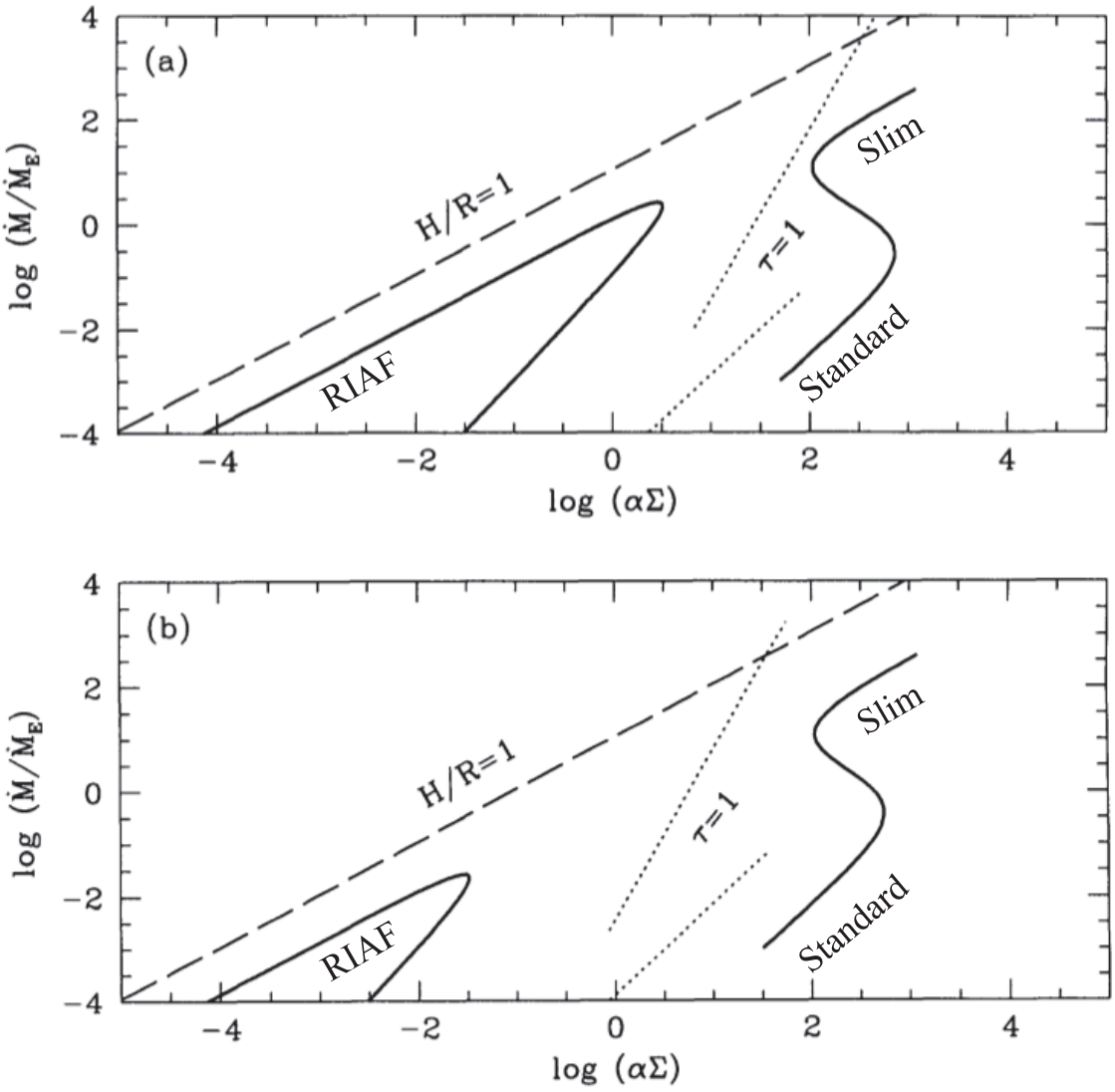

Figure 2.9: Thermal equilibria for accretion disks with a viscosity parameter (α) of 0.1 (a) and 0.01 (b) (Abramowicz et al., 1995). The left solid line and right solid S-shaped line are the optically thin and thick accretion disk solution, respectively. The dotted lines show $\tau = 1$ calculated by assuming that the gas pressure or the radiation is dominant. The left and right side lines show the inverse-Compton scattered and the optically-thick. M and $R_{\rm in}$ are assumed to be 10 $M_\odot$ and 5 $R_{\rm g}$, respectively.

the low/hard state $\dot{M}$ decreases, and the RIAF model can explain the spectrum of galactic black holes and low luminosity galactic nuclei.

The standard accretion disk (α-disk) model was established in the early 1970's owing to theoretical efforts by Lynden-Bell, Pringle, Rees, Shakura, Sunyaev, Novikov, Thorne, and others. Theoretical research of accretion disks has developed mainly based on this α model. To introduce the standard accretion disk of (Shakura & Sunyaev, 1973), we have to make the following assumptions:

1. The disk mass is ignored and the gravitational field is determined only by $M_{\rm BH}$.
2. The disk exists in the equatorial plane of the BH.
3. The disk is steady.
4. The disk is axisymmetric
5. The disk is geometrically thin: the ratio of thickness (H) to radius (r) is below one.
6. Keplerian roatation is dominant: the drift velocity (v_ϕ) is smaller than the rotation velocity (v_r).
7. Hydrostatic balance holds in the vertical direction.
8. The disk is optically thick in the vertical direction.
9. Magnetic fields are ignored in global systems.
10. The component of the viscous stress tensor is proportional to the pressure.

2.5.1 Thermal energies

The potential energy of accreting gas is first converted to thermal energy via viscous processes, and is then released as radiation. Since the viscous heating rate per unit volume is $\rho\nu(rd\Omega/dr)^2$ where ρ is the density, ν is the kinematic viscosity and Ω is the angular velocity the vertically integrated heating rate per unit surface are is

$$Q^+_{\rm vis} = \int_{-\infty}^{+\infty} \rho\nu(rd\Omega/dr)^2 dz = \frac{9}{4}\nu\sum\Omega^2 = -\frac{3}{2}T_{r\phi}\Omega, \tag{2.16}$$

where $\Omega = \Omega_{\rm K} \propto r^{-3/2}$. z is the vertical axis or the disk depth. Cooling is due to radiation from the disk surface. Since the disk is effectively optically thick in the vertical direction.

$$\tau = \overline{\kappa}\rho H = \frac{\overline{\kappa}\sum}{2} >> 1, \tag{2.17}$$

where $\tau(=\overline{\kappa}\sum/2)$ is the optical depth and $\overline{\kappa}$ is the Rosseland-mean opacity. In addtion it is assumed that the disk gas emits a blackbody spectrum with an effective temperature of $T_{\rm eff}$.

Further, we assume that the main energy transfer inside the disk is due to radiation. The radiative flux in the z-direction is

$$F(z) = -\frac{4ac[T(z)]^3}{3\kappa(z)\rho(z)}\frac{\partial T}{\partial z}, \tag{2.18}$$

at each height z, where a is the radiation constant ($\rho = ac/4$) and T is the temperature inside the disk. Under the one-zone approximation, we can then express the cooling rate in terms of the temperature T_c at $z = 0$ as

$$Q^{-}_{\rm rad} = 2F(H) = 2\frac{4acT_c^4}{3\tau} = \frac{32\rho T_c^4}{3\tau}. \tag{2.19}$$

Finally, the local energy balance at each radius is given by

$$Q^{+}_{\rm vis} = Q^{-}_{\rm rad}. \tag{2.20}$$

where heating is due to the viscosity and cooling is via the spatial diffusion of the blackbody radiation. For this to be efficient, the thermal timescale needs to be much shorter than the matter diffusion timescale; $t_{\rm th} << t_{\rm vis}$.

The viscosity in the accretion disk plays two important roles: transport of angular momentum and heating of the disk plasma. The dominant sources of viscosity are assumed to be chaotic magnetic fields and turbulence in the gas flow.

$$t_{r\phi} = \rho \nu r \frac{d\Omega}{dr} = -\alpha p, \tag{2.21}$$

or

$$T_{r\phi} = \nu \sum r \frac{d\Omega}{dr} = -\alpha \Pi, \tag{2.22}$$

where α is the viscosity parameter ($\alpha \leq 1$), and p is the total pressure. The α prescription is sometimes expressed in terms of ν.

Since the cooling rate is the amount of emergent energy flux from a unit area of the surface, it is also expressedas

$$Q^{-}_{\rm rad} = 2F = 2\sigma T_{\rm eff}^4, \tag{2.23}$$

where σ is the Stefan-Boltzmann constant, and the factor 2 represents radiation from the two sides of the disk. The flux (F) of the disk can be written as

$$F = \sigma T_{\rm eff}^4 = \frac{3GM\dot{M}}{8\pi r^3}\left(1 - \sqrt{\frac{r_{\rm in}}{r}}\right). \tag{2.24}$$

The emergent local flux from the surface of the disk is thus independent of the magnitude of the viscosity parameter, α, and is proportional to r^{-3} at $r >> r_{\rm in}$.

$$T_{\rm eff} = \left[\frac{3GM\dot{M}}{8\pi r^3}\left(1 - \sqrt{\frac{r_{\rm in}}{r}}\right)\right]^{(1/4)}. \tag{2.25}$$

2.5.2 The energy spectrum of the accretion disk

The effective temperature ($T_{\rm eff}$) of the disk has radial dependence in the accretion disks. We approximate $T_{\rm eff}$ at a radius from equation 2.25, as follows

$$T_{\rm eff} = T_{\rm in} r^{-3/4}. \tag{2.26}$$

The approximation ignores a term $(1 - \sqrt{(r_{\rm in}/r)})$ of equation 2.25. Thus, the disk is hotter in the inner region than in the outer one. The total disk spectrum is composed of multi-color

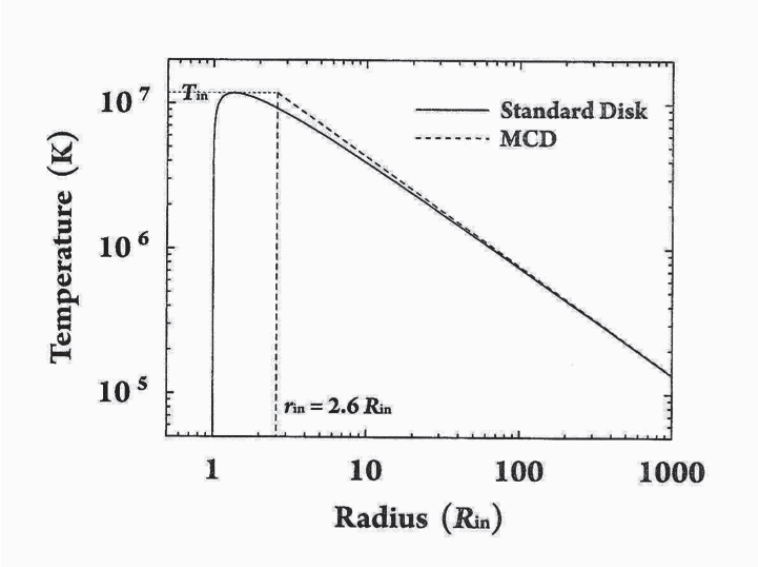

Figure 2.10: The effective temperature as a function of the radius. The solid line shows the standard disk model and the dashed line shows the MCD model. The figure is taken from Yoshida et al. (2009).

blackbody spectra; high-energy photons mainly come from the inner portion of the disk, and low-energy photons originate from the outer portions. Multiple temperatures of the accretion disk is usually designated as *multi-color* from the X-ray spectra. The heat generated in the accretion disk is radiated from the surface as black body radiation. $T_{\rm eff}$ can be given by the equation as a function of M, $\dot{M}$ and r.

Figure 2.10 shows a disk temperature of the standard disk and the multi-color disk (MCD) model. In the case of a non-spinning BH with $M_{\rm BH} \sim 10\,M_{\odot}$ and $\dot{M} \sim 0.1\,M_{\rm Edd}$, the maximum temperature ($T_{\rm eff}^{\rm max}$) at $r = (7/6)^2 R_{\rm in}$ can be written as

$$T_{\rm eff}^{\rm max} = \left(\frac{3GM_{\rm BH}\dot{M}}{8\pi\sigma R_{\rm in}^3}\right)\cdot 6^{3/2}\cdot 7^{-7/4}. \tag{2.27}$$

The value of $T_{\rm eff}^{\rm max}$ is calculated as 1.18×10^7 K. On the other hand, the disk temperature of the MCD model ($T_{\rm eff}^{\rm MCD}$) is approximated as

$$T_{\rm eff}^{\rm MCD} = \left[\frac{3GM_{\rm BH}\dot{M}}{8\pi\sigma r^3}\right]^{1/4} = T_{\rm in,eff}\left(\frac{r}{r_{\rm in}}\right)^{-3/4}, \tag{2.28}$$

where $T_{\rm in,eff} \equiv T_{eff}^{max}$ and $r_{\rm in} \equiv (7/6)^2\cdot 7^{1/3} R_{\rm in} \sim 2.6\,R_{\rm in}$.

The black body radiation can be written as follows

$$B_\nu(r) = \frac{2h}{c^2}\frac{\nu^3}{exp[h\nu/k_{\rm B}T_{\rm eff}(r)]-1}. \tag{2.29}$$

The observed flux S_ν of the disk is calculated by integrating the surface intensity. Thus S_ν can be written as follows,

$$S_\nu = \frac{\cos i}{D^2}\int_{r_{\rm in}}^{r_{\rm out}} B_\nu(r) 2\pi r {\rm d}r. \tag{2.30}$$

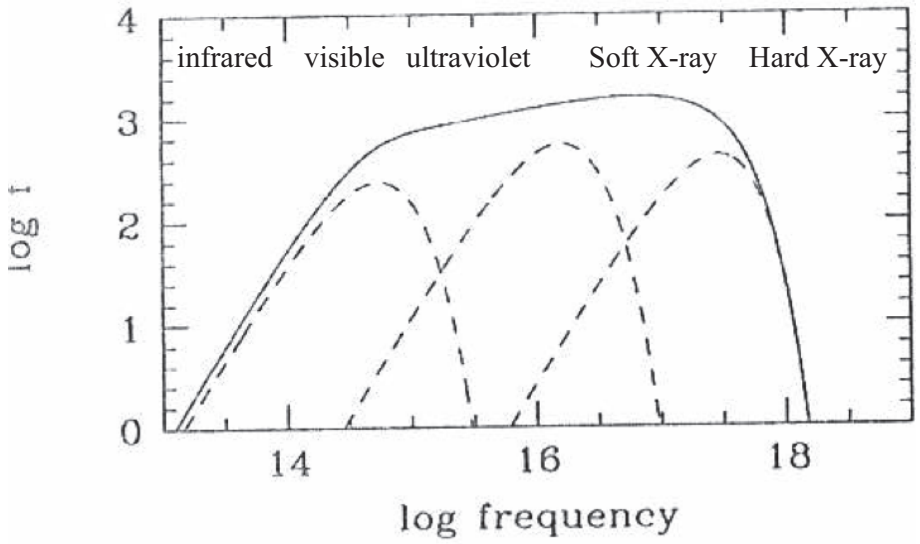

Figure 2.11: Typical spectrum of the standard accretion disk. $M_{\rm BH}$, $\dot{M}$, $r_{\rm in}$ and $r_{\rm out}$ are assumed to be 10 $M_\odot$, 10^{18} g s^{-1}, 3 $r_{\rm s}$=9$\times$10^6 cm, and $r_{\rm out}$=10^{11} cm, respectively. The figure is taken from Kato et al. (2008).

As a result of this integration, we can observe the equation as

$$S_\nu \propto \nu^{1/3}, \tag{2.31}$$

for

$$\frac{k_{\rm B}T_{\rm in}}{h}\left(\frac{r_{\rm in}}{r_{\rm out}}\right) \ll \nu \ll \frac{k_{\rm B}T_{\rm in}}{h}. \tag{2.32}$$

The equation S_ν expresses the middle part of the continuum spectra from the standard disk. Figure 2.11 shows the spectrum of a *multi-color* disk corresponding to the disk during the high/soft state. There is a Wien cut-off in the high-frequency region because an inner edge of the disk exists. On the other hand, in the low-frequency region there is a Reyleigh-Jeans slope due to radiation from the outer region. The spectrum with the characteristics is called the disk-black body spectrum.

2.5.3 Disk structure

The solved structure of the standard accretion disk is summarized in figure 2.12. The region is divided into three regions (the inner, middle and outer regions) by the opacity and gas pressure.

2.5.4 Timescales of the accretion disk

The variation of the accretion disk is characterized by dynamical, thermal and viscous timescales. The dynamical timescale (t_ϕ) is the one on which in homogeneities on the disk surface rotate or

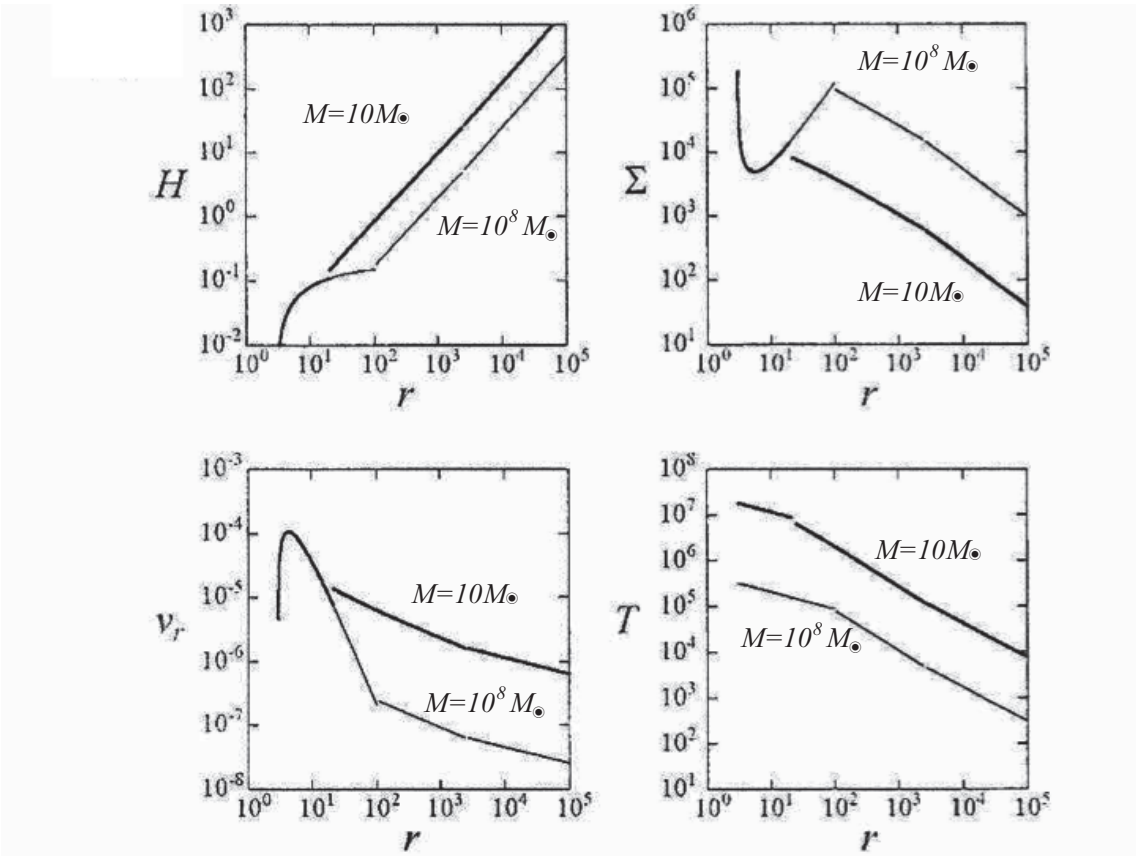

Figure 2.12: Typical solution of a standard accretion disk of M=10 $M_\odot$, $\dot{M}$=1 $M_\odot$, and α=1 for thick solid curves, and that of M=10^8 $M_\odot$, $\dot{M}$=10 $M_\odot$, and α=1 for solid curves. The unit of the radius is the Schwarzschild radius ($R_{\rm s}$) (top-left panel). The disk half-thickness with the unit of $R_{\rm s}$, (top-right panel) the surface density with the unit of g cm^{-2}, (bottom-left panel) the radius velocity with the unit of light velocity (c), and (bottom-right panel) the temperature in the unit of K are plotted. The figure is taken from Kato et al. (2008).

hydrostatic equilibrium in the vertical direction is established.

$$t_\phi \sim \frac{r}{v_\phi} \sim \frac{1}{\Omega_{\rm K}}, \tag{2.33}$$

where r, v_ϕ and $\Omega_{\rm K}$ are radius, the velocity in a radial direction and angular momentum. The viscous timescale ($t_{\rm visc}$) is the timescale on which matter diffuses through the disk under the effect of viscous torques. In other words, the $t_{\rm visc}$ is the drift timescale.

$$t_{\rm visc} \sim \frac{r}{v_r} \tag{2.34}$$

where v_r is the drift velocity.

The $t_{\rm visc}$ is much longer than t_ϕ as follows

$$t_{\rm visc} \gg t_\phi. \tag{2.35}$$

The $t_{\rm visc}$ is much also longer than the hydrostatic timescale ($t_{\rm hyd}$) over which the vertical disk structure varies as follows

$$t_{\rm visc} \gg t_{\rm hyd} = \frac{H}{c_{\rm s}}, \tag{2.36}$$

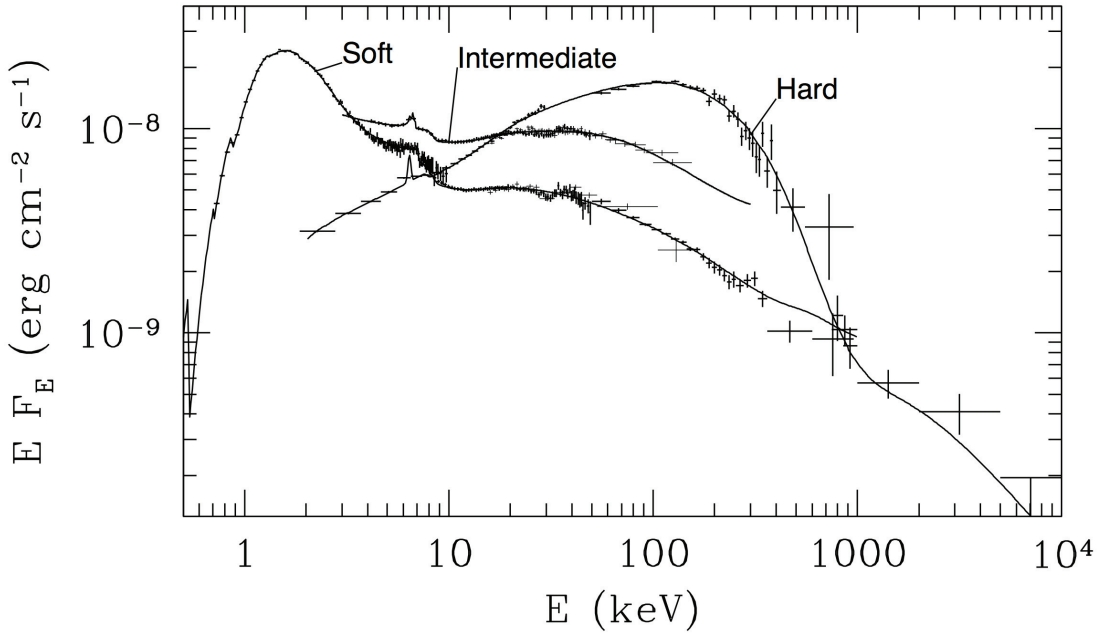

Figure 2.13: Typical spectrum during the high/soft and low/hard state. The figure is taken from (Marek et al., 1999).

where c_s is the speed of sound and H is the depth of the disk.

The thermal timescale (t_{th}) is the timescale for re-adjustment to thermal equilibrium in the disk as follows

$$t_{th} \sim \frac{1}{\alpha \Omega_K}. \tag{2.37}$$

These timescales also have another relation as follows,

$$t_\phi \sim \alpha t_{th} \sim (H/r)^2 t_{visc}. \tag{2.38}$$

The numerical solution of t_{visc} is given as,

$$t_{visc} \sim 3 \times 10^5 \alpha^{-4/5} \dot{M}_{16}^{-3/10} M_1^{1/4} R_{10}^{5/4} \mathrm{s}, \tag{2.39}$$

where the units of $\dot{M}_{16}$, R_{10} and M_1 are 10^{-16} g s^{-1}, R 10^{-10} cm^{-1} and M/M_{sun}, respectively. The t_{visc} will be $\sim$ a day if the BH mass is 10 $M_\odot$.

2.6 X-ray spectrum of black hole binaries

It is known that black hole candidates have two spectral states, a high/soft state and a low/hard state as shown in figure 2.13. The high/soft state shows an X-ray spectrum which is roughly described by thermal emission, and the low/hard state is roughly described by powerlaw emission. Both timing and spectral properties vastly change as the X-ray flux suddenly increases (the X-ray outburst evolves). The intermediate state appears in between the low/hard and high/soft state during which the spectrum shows disk emission but prominent steep powerlaw emission as well.

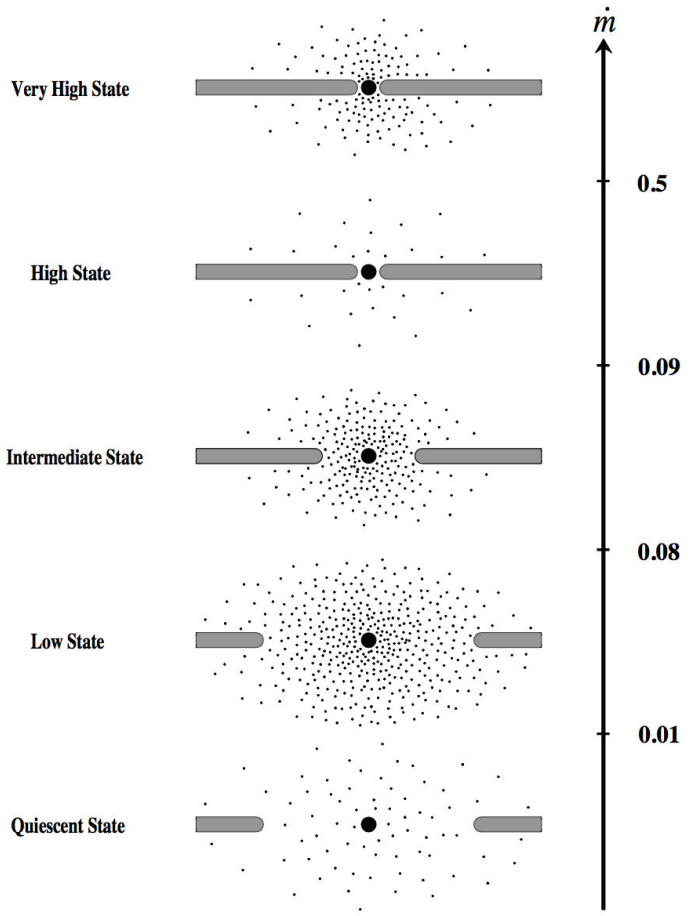

Figure 2.14: A schematic view of the configuration of the accretion rate in different spectral states (Esin et al., 1991) as a function of the total mass accretion rate $\dot{m}$.

X-ray emission from BHBs comes from the release of gravitational energy of accreting matter falling into a black hole. The state change depends on the mass accretion rate from the companion star. The mass accretion onto the black hole in HMXBs is believed to be provided by the stellar wind while that in LMXBs by Roche lobe overflow. When the mass accretion rate is greater than that of the high/soft state, the spectrum was believed to become a very high state. The very high state is an X-ray luminosity comparable to or higher than that of the high soft state. Figure 2.14 shows the configuration of the disk and the Corona for several $\dot{M}$s.

2.6.1 The high/soft state

In the high/soft state, which is usually observed in the middle of the outburst, time variability is quite suppressed, and the energy spectrum is soft and well described by thermal disk emission (cf., Multi-Color Disk model (MCD) developed by Mitsuda et al., 1984 and Makishima et al., 1986) accompanied by a steep powerlaw with a photon index of $\sim$2.5. A conceivable picture of this state is that the optically thick and geometrically thin disk, the so-called standard disk (Shakura & Sunyaev, 1973) as shown in figure 2.14 second pannel, is extended down to the inner most stable circular orbit (ISCO). This is strongly supported by the fact that the innermost

disk radius estimated from the temperature and luminosities of the thermal disk emission model is found to be remarkably constant over a wide range of luminosity (Makishima et al., 1986). Since the ISCO depends only on the BH mass and spin, this method can constrain the BH spin if the distance, the inclination, and the BH mass are given (Makishima et al., 2000). The accretion geometries such as a disk-corona configuration and their evolution as a function of time and mass accretion rate have been discussed by many authors (Remillard & McClintock, 2006), but it is still unclear why the phenomenological state is related to the outburst phase, and if the trend can be universally seen in all LMXBs.

2.6.2 Low/hard state: Comptonized radiation

In the low/hard state, mostly observed at the beginning and the end of the outburst, the X-ray spectrum is approximately a powerlaw with a photon index of 1.5–1.8 and a high-energy cut-off at ∼100 keV, which is interpreted as inverse-Compton X-ray emission from the hot corona around the black hole (Remillard & McClintock, 2006). The inverse-Compton process radiates with the radiative cooling rate ($Q_{\rm rad}$) as follows,

$$Q_{\rm rad} = \left(\frac{4k_{\rm B}T_{\rm e}}{m_{\rm e}c^2}\right)\sum \kappa_{\rm es} E c, \tag{2.40}$$

where E, $\kappa_{\rm es}$, $k_{\rm B}$, $T_{\rm e}$, $m_{\rm e}$, c are the radiation energy density, the electron-scattering opacity (=σ_T/m_p), Boltzmann constant, temperature of electron, mass of electron and light speed, respectively. The Compton y-parameter is defined as follows,

$$y = \left(\frac{4k_{\rm B}T_{\rm e}}{m_{\rm e}c^2}\right) Max(\tau_{\rm es}, \tau_{\rm es}^2), \tag{2.41}$$

where the $\tau_{\rm es}$ is optical depth (= $n_{\rm e}$ σ_T l) the $Max(\tau_{\rm es}, \tau_{\rm es}^2)$ is the number of scatterings ($N_{\rm s}$).

A more precise condition for repeated scattering to change the spectrum of the radiation field can be obtained as follows: The change in the energy of a typical photon after $N_{\rm s}$ scatterings,

$$\frac{E'}{E} = \left(1 + \frac{4k_{\rm B}T_{\rm e}}{m_{\rm e}c^2}\right) \simeq exp\left(\frac{4k_{\rm B}T_{\rm e}N_{\rm s}}{m_{\rm e}c^2}\right) = exp(y). \tag{2.42}$$

In general when y is over 1, the total photon energy and the spectrum will be significantly altere; whereas for y below one the total energy is not much changed.

Figure 2.15 shows the spectrum resulting from unsaturated Comptonization. We assumed that measurement of only the shape of an unsaturated Compton spectrum with a soft photon source determines both the electron temperature and the scattering optical depth of the source. The emergent intensity in the power-law regime satisfies

$$I_\nu \sim I_{\nu_s}\left(\frac{\nu}{\nu_s}\right)^{3+m}, \tag{2.43}$$

where m is can be written using the y-parameter as follows

$$m = -\frac{3}{2} \pm \sqrt{\frac{9}{4} + \frac{4}{y}}. \tag{2.44}$$

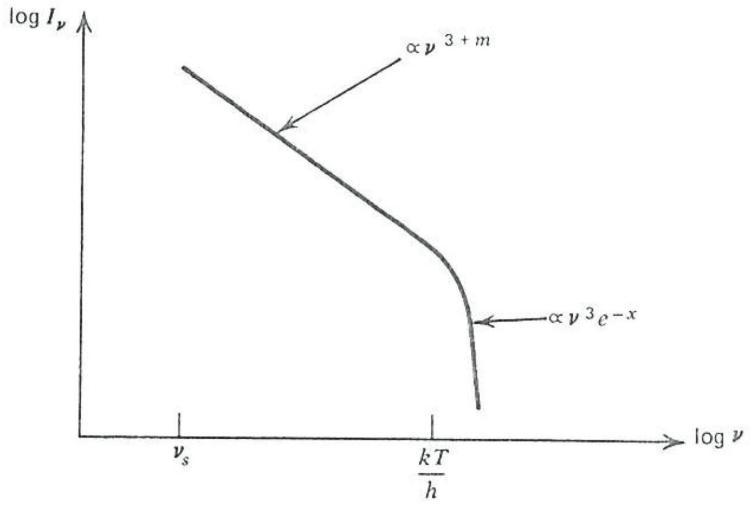

Figure 2.15: Spectrum produced by unsaturated Comptonization of low energy photons by thermal electrons (Rybichi & Lightman ., 1979).

The input energy is significantly amplified for $m > -4$, that is, $y > 1$. The value of $k_B T/h$ corresponds to the temperature of a thermal electron. The configuration of the low/hard state is believed to be a spread Corona and a diffused accretion disk as shown in figure 2.14 fourth panel.

2.6.3 The very high state

The very high state shows a steep powerlaw like component (typically $\gamma \sim 2.5$, Esin et al. 1991) and an X-ray luminosity comparable to or higher than that of the high soft state. The spectrum is considered to be a mixture of a weak disk component and a strong Comptonized component. Figure 2.16 shows the spectrum during the very high state of XTE J1550-564 (Kubota et al., 2004). The hard component extends to the energy of 100 keV and the accretion disk component is exists.

2.7 Remaining issues on the spectral analysis

To investigate the environment surrounding the BH, we usually fit the radiation models (the multi-color disk model, the Comptonization models and so on) to the X-ray spectrum. The X-ray spectrum during the low/hard can be explained well by a powerlaw spectrum with a break energy corresponding to the temperature of the Corona electron. However it is very difficult to form the model to explain the X-ray spectrum during the high/soft state, because the two continuous component of the accretion disk and the Corona have to be resolved from the continuous X-ray spectrum.

2.7.1 The disk and hard components

In the high/soft state the X-ray spectrum below 3 keV can be roughly explained by the multi-color disk but there is a hard X-ray excess over 3 keV. When we estimate the accretion disk from

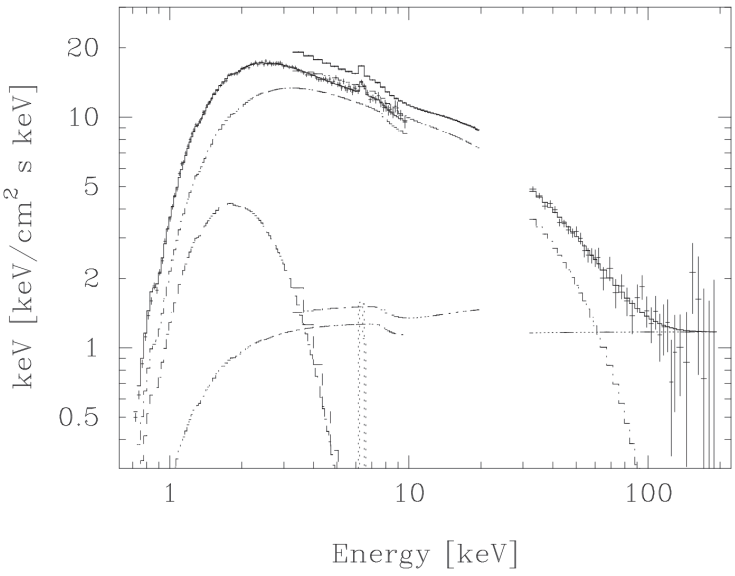

Figure 2.16: The spectrum during the very high state of XTE J1550-564 (Kubota et al., 2004). The accretion disk component is smaller than the hard component extending to 100 keV.

the X-ray spectra between 0.6 keV and 10 keV, we usually use a phenomenological powerlaw model for the hard excess. Figure 2.17 shows the X-ray spectrum between 0.5 keV and 10 keV and the accretion disk and the powerlaw components during the high/soft state (Dotani et al., 1997). The X-ray spectrum can be well described by the accretion disk and powerlaw models.

It is difficult to explain the wide band energy X-ray spectrum by fitting a model, because the hard radiation needs to be explained in the spectrum. Figure 2.18 shows the energy spectrum observed by *NuSTAR* and *Suzaku* and two types of model to explain the spectrum. The two models include the accretion disk, the hard component and a reflection component and both fitting results are acceptable. The disk model of Model A is different from that of Model B: the accretion disk of Model B includes relativistic effects. There is a different configuration of the hard component between Model A and B: the low energy dip.

2.7.2 The reflection component

The X-ray spectrum from BHs, also includes Fe-K emission and a reflection component. Figure 2.13 shows the the Fe-K emission and the refection components need to explain the X-ray spectrum as shown in figure 2.18. When the inverse-Compton emission around the disk illuminates the disk and the photons are reflected by the disk material, the fluorescence iron-K lines at 6.4 keV and a K absorption edge of iron near 7.1 keV appear. In particular, during the low/hard state there are the significant iron lines and an absorption edge. The reflection model includes the iron lines, the absorption edge and the continuum which explains the Compton emission reflected by the disk. To investigate the relativistic effect near the BH, some studies use the reflection component and the iron lines.

Today, the method of fit analysis is standard and we need to solve the degeneracy between the disk, the hard component and the reflection to separate the accretion disk from the X-ray spectra. In this paper, we tried to investigate the accretion disk paying attention to the spectral

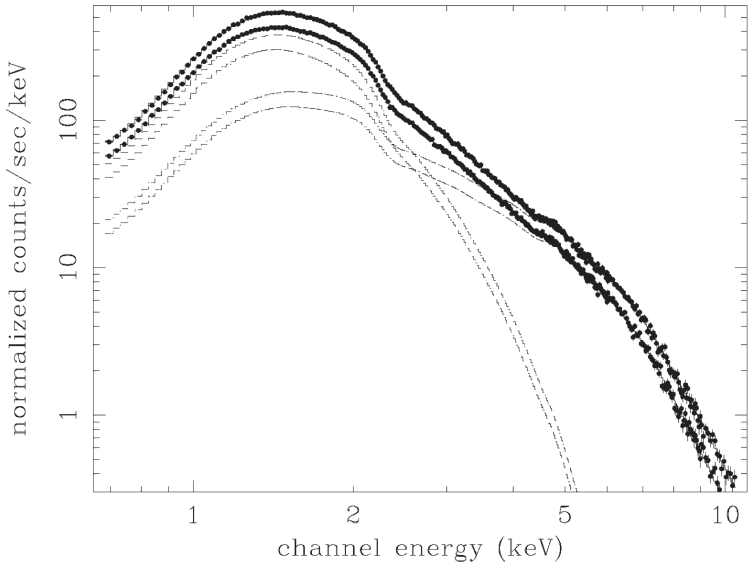

Figure 2.17: The energy spectra of Cyg X-1 observed by *ASCA* during the high/soft state in May 30th and 31th 1996 and the best-fit models of the accretion disk and powerlaw components (Dotani et al., 1997).

change with the timescale of $\sim$ days.

2.8 X-ray polarimetry observation

2.8.1 Polarized X-ray from the accretion disk

The X-ray emitted by the disk black body are scattered on the disk surface. The X-ray from the accretion disk are polarized by the Thomson scattering on the surface of the disk. The cross section of the Thomson scattering is depending on the polarization angle of incident X-ray. The incident X-rays are more likely to be scattered to the direction which forms 90° with its polarization direction. In the case of the Thomson scattering, very large polarization fractions can be achieved when the scattering angle is near 90° with its travel direction. The polarization angle of the X-ray from the accretion disk is parallel to the disk, because the X-ray is scattered to observers. Figures 2.19 show ray-traced image of direct radiation from a accretion disk around the BH. Figures 2.19 (a) shows the Ray-traced image without returning radiation. The returning radiation is emitted by an accretion disk and returns to the disk surface due to gravitational focusing around the BH. The gravitational focusing is one of relativistic effects. The polarization angle is parallel to the disk in figure 2.19 (a). The yellow area shows relativistic beaming of the accretion gas moving towards the observer.

Figures 2.19 (b) shows the Ray-traced image with the returning radiation. The polarization angles are not only parallel but also verticality to the accretion disk. The X-ray polarized to verticality to the accretion disk can not be observed without any effects, because the X-rays polarized to verticality are scattered to the direction of 90° with respect to the observer. The X-ray polarized to verticality can be bend and returned to the disk surface by the gravitational focusing, because there should be the BH on the scattered direction of the X-ray polarized to

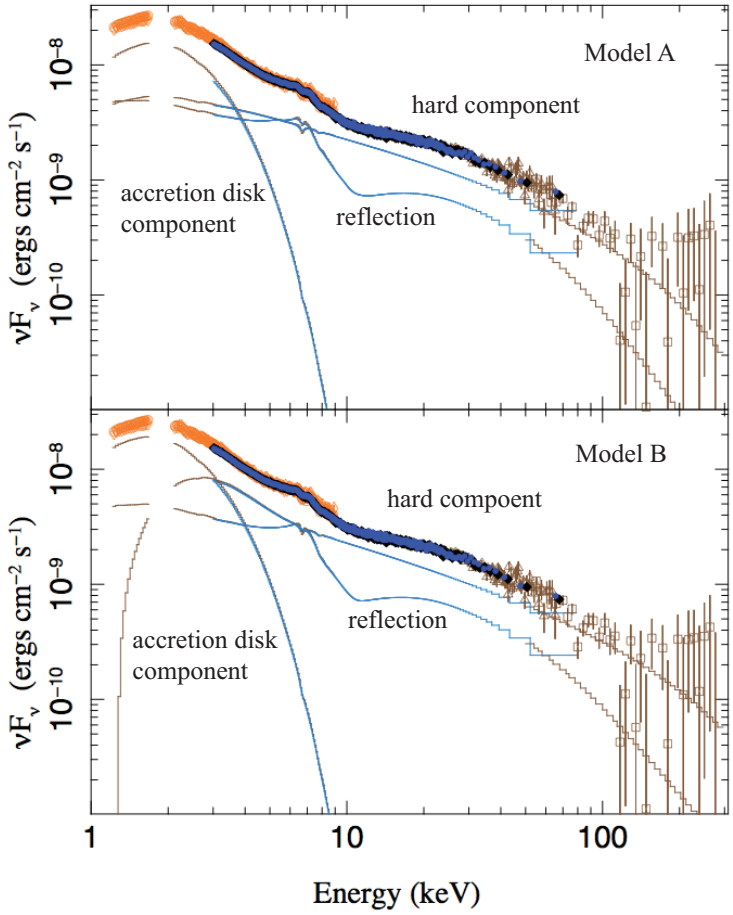

Figure 2.18: The energy spectra of Cyg X-1 observed by *NuSTAR* and *Suzaku* (Tomsick et al., 2014). Both of the two best-fit model include three components; the accretion disk, the hard component and reflection components. The disk model of the Model A is different from that of Model B.

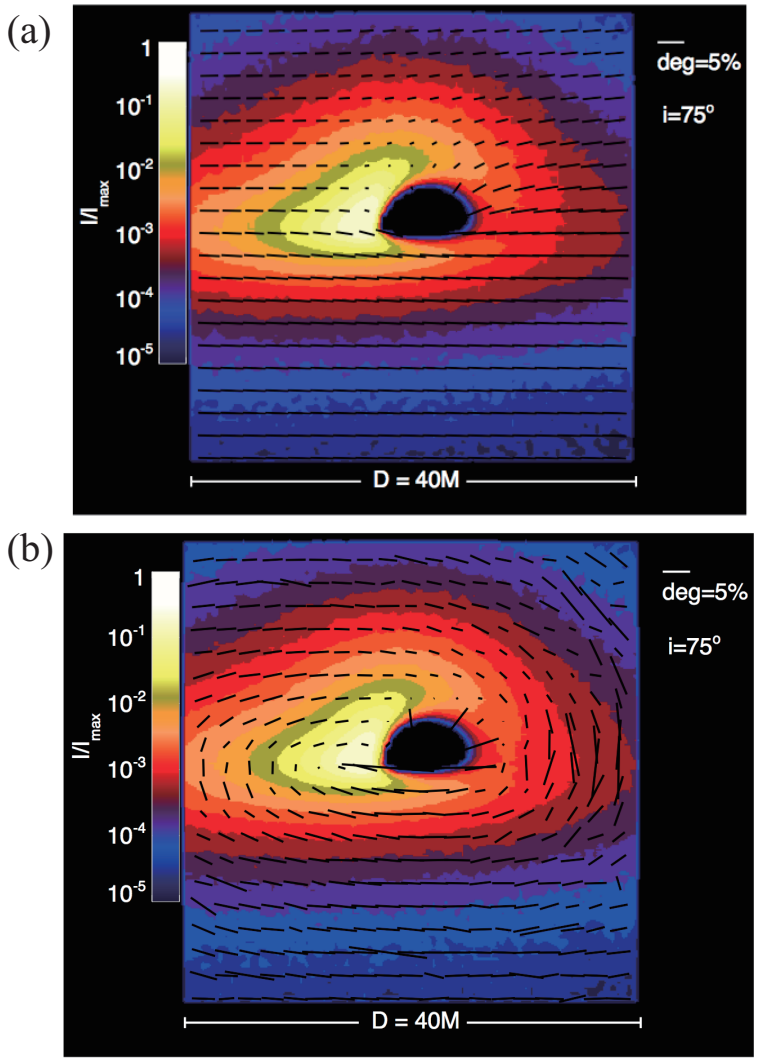

Figure 2.19: Image of radiation traced from a thermal disk without (a) and with (b) the gravitational focusing (Schnittman & Krolik , 2009). The black lines show the polarization angle of X-ray. Photons which are emitted by the inner disk are bent by the BH. and are scattered of the opposite side of the disk towards the distant observer.

verticality. The X-rays returned are scattered on the disk surface and observed to be polarized to verticality. The verticality X-ray which cannot be observed without the gravitational focusing. The X-ray polarization from the accretion disk is depending on the BH spin, because the magnitude of the gravitational focusing is depending on the distance from the BH and the inner radius of the disk is depending on the BH spin (§2.4.2).

Figure 2.20 shows polarization degree and angle for a range of BH spin. The X-rays which is polarized to be parallel to the accretion disk is dominant without the BH spin. On the other hand, the X-ray polarization with the maximum spining is verticality to the disk because the gravitational focusing bents a number of X-rays polarized to verticality and the X-ray polarized are scattered on the disk surface. Thus, the polarization fraction of the energy band between 0.6 and 2 keV decreases as the spin parameter increases. In case of the maximum spining, the polarization angle of the X-ray in the energy band over 2 keV became to be 90°. High-energy photons from the hotter inner parts of the disk are more likely to return to the disk than the low-energy photons emitted at larger radii since they experience stronger gravitational deflection. As the spin increase, the inner radius of the accretion disk moves closer to the event horizon and the polarization angle of the X-ray reaching the observer becomes vertically.

2.8.2 The *PRAXyS* mission

The goal of the *PRAXyS* (Polarimeter for Relativistic Astrophysical X-raY Sources) mission is to observe X-ray linear polarization from astrophysical sources such as BHs, neutron stars, supernova remnants in the energy band between 2 and 10 keV. X-ray polarization has important information of the magnetic field, general relativity or the reflection plane structure near the astrophysical sources. The X-ray polarization observation have been not performed since the observation of the *OSO-8* mission because it is difficult to detect the X-ray polarization technically. Recent advances in the gas detector technology, notably the development of Micropattern Gaseous Detectors (MPGDs), have enabled exploitation of polarimetry.

Important radiative processes of X-ray polarization are Thomson scattering and synchrotron radiation. The X-rays affected by the scattering or the X-ray emitted by the synchrotron process are highly polarized. In the case of Thomson scattering, very large polarization fraction can be achieved and the polarization angle is perpendicular to the plane formed by the incident and reflected rays. The polarization degree of the synchrotron radiation depends on the orientation of the magnetic field.

The polarimetry contains information of emission mechanism and radiation transport that imaging and spectroscopy cannot probed. X-ray polarization is essentially free from the foreground depolarization, because the wavelength of the X-ray is shorter and cross sections against materials are very small. The X-ray polarization will open a new observational window in astrophysics.

2.8.3 X-ray polarimeter

The collision process between material and X-ray in the energy band of 2-10 keV is mainly the photoelectric absorption. In the case of the *OSO-8* mission, Bragg reflection is used to detect the X-ray polarization. The quantum efficiency of Bragg reflection is much lower than that of the photoelectric absorption, and the X-ray polarization was detected only in a bright synchrotron source, Crab Nebula (Weisskopf., 1976). To improve the detection efficiency of the X-ray, utilization of the photoelectric absorption effect is the best. However, measuring polarization

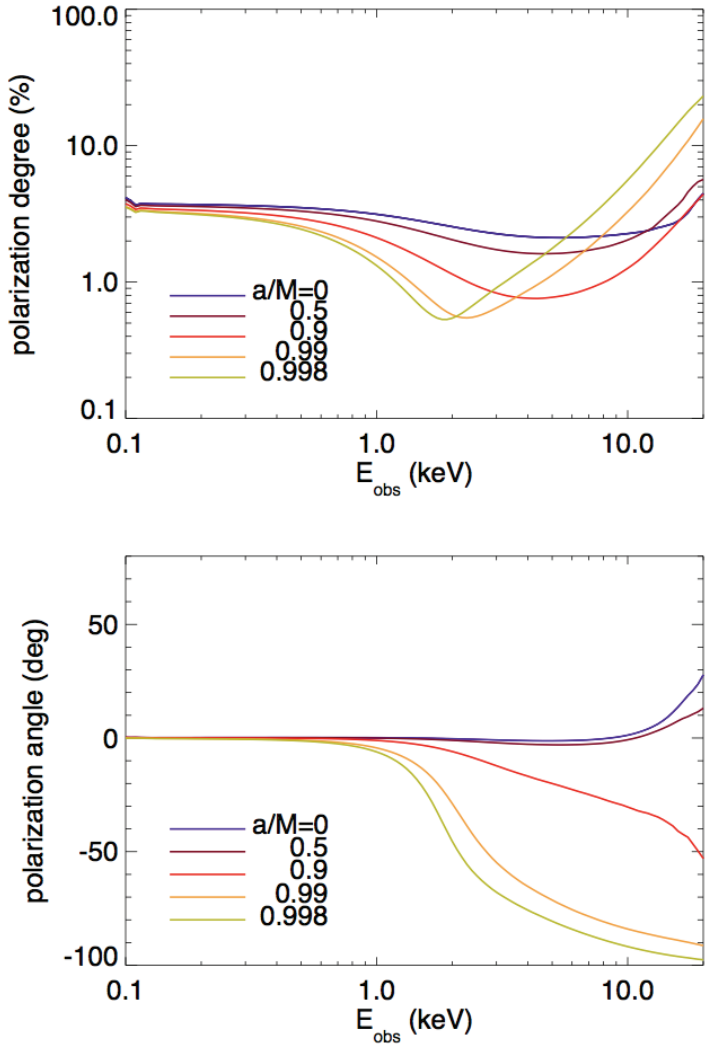

Figure 2.20: Polarization degree and angle as a function of the energy of X-ray for a range of BH spin parameter (Schnittman & Krolik , 2009). The parameter of inclination angle, BH mass and the eddington ratio are 75°, 10 $M_{\odot}$ and 0.1.

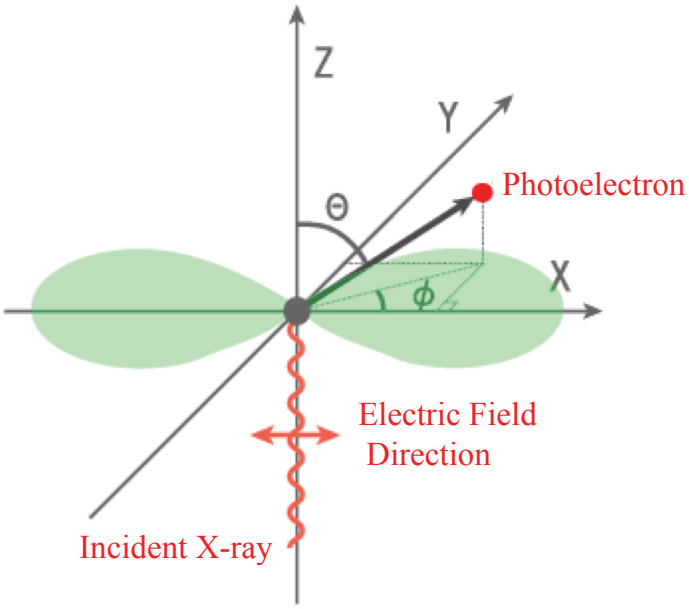

Figure 2.21: The picture on the photoelectric absorption process. The Z axis is the direction of the incident X-ray, the X axis is the direction of the electric field. θ is the angle between the directions of the incident X-ray and the photoelectron. ϕ is the angle between the directions of the electric field of X-ray and the photoelectron.

with the photoelectric absorption effect is technically difficult, because it is necessary to trace a very short track ($\sim$1 mm) of emitted photoelectrons.

Figure 2.21 shows the schematic view of the photoelectric absorption process. The sensitivity of photoelectric polarimeters arises from the angular distribution of the initial directions of the photoelectron track. The differential cross-section ($d\sigma/d\Omega$) of the photoelectric absorption effect can be written as follows,

$$\frac{d\sigma}{d\Omega} \propto \frac{\sin^2\theta\cos^2\phi}{(1-\beta\cos\theta)^4} \tag{2.45}$$

where θ is the angle between the directions of the incident X-ray and the photoelectron, ϕ is the angle between the directions of the electric field of X-ray and the photoelectron projected in the X-Y plane and β is the ratio of the electron velocity (v) to the light speed (c).

The photoelectron is suffered form the multiple Coulomb scattering in the material. The length of the photoelectron track is too short in the solid material to measure the track, since the density is large and the mean free path is short. To make longer the track length, the *PRAXyS* mission used the gas (100% pure dimethyl ether under 190 Torr) as the target material. When the X-ray of 5.9 keV absorbed by the gas the photoelectron track length is $\sim$1.6 mm. *PRAXyS* carries two X-ray polarimeters, which use Time Projection Chamber (TPC) technique, located at the foci of grazing incidence mirrors. Figure 2.22 shows the diagram of the TPC polarimeter of the *PRAXyS* mission.

The photoelectron goes through gas ionizing the atomic of the gas. The shape of the electron path which is created by the photoelectron in the gas implies the direction of the electric field of the X-ray. The photoelectron tracks drift in a uniform electric field, perpendicular to the photon direction, to a multiplication stage which is read out by continuously sampled strip electrodes.

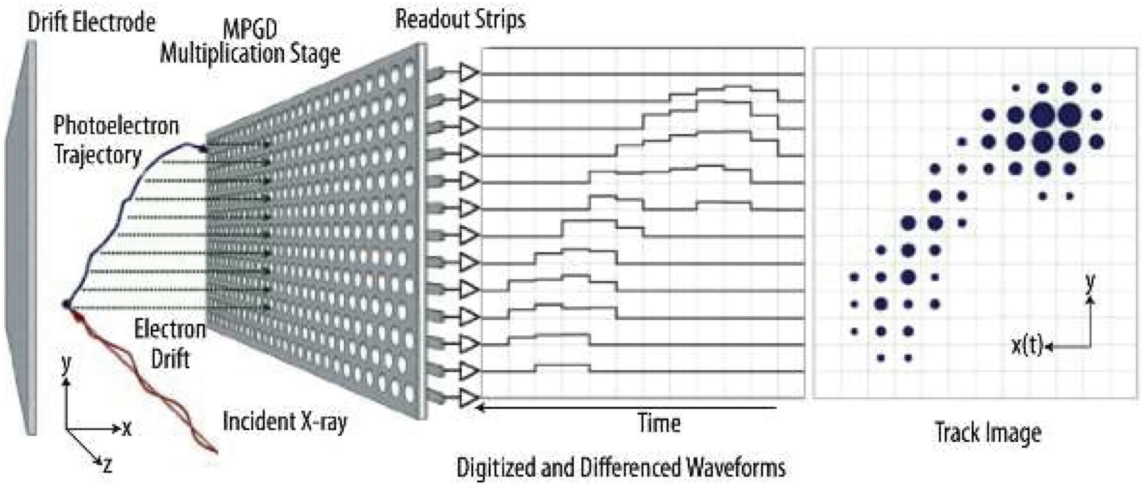

Figure 2.22: Schematic diagram of the TPC polarimeter of the *PRAXyS* mission. See the text for detail.

The time series from adjacent strips from an image of the track.

2.8.4 Gas electron multiplier

Total charge of the electron path which the photoelectron ionized is too small to read out. Gas electron multiplier (GEM) is used to multiple charge of the electron path keeping the shapes and is one of MPGDs. The GEM structure is parallel plate capacitor which are vacated a lot of through holes. Figure 2.23 shows the sectional and surface view of GEM. High energy astrophysics laboratory at RIKEN develops the techniques to provide the GEM optimized for using at the satellites orbits and supplied the GEMs to the *PRAXyS* mission. The GEMs are provided by the laser etching techniques (Tamagawa et al., 2009). When the electrodes GEM are applied voltage, the strong electric fields accelerate the electron in the gas and electronic avalanche occurs in the holes. Figure 2.24 shows one of electric-field simulations. Electrons of the path are multiplied by each through holes of the GEM and the shape of the electrode path are kept.

The GEM can be broken by discharge between the electrodes. When the discharges happens between the electrodes, the insulator is carbonated and there is permanent conduction between the electrodes. To improve the weakness against the discharge, we replaced the copper of the GEM electrodes with a resistive material. The electric resistance of the electrode can reduce the discharge current. We use a conductive plastic as the resistive materials. The GEM which is composed by the resistive material are called Resistive Electrode GEM (RE-GEM) (Yoshikawa et al., 2012). The development of RE-GEM is succeeded to multiply charges. The *PRAXyS* mission choose the GEM which is composed by the copper electrodes, because there is not enough time to optimize the RE-GEM for the mission. The RE-GEM might be used in the next missions.

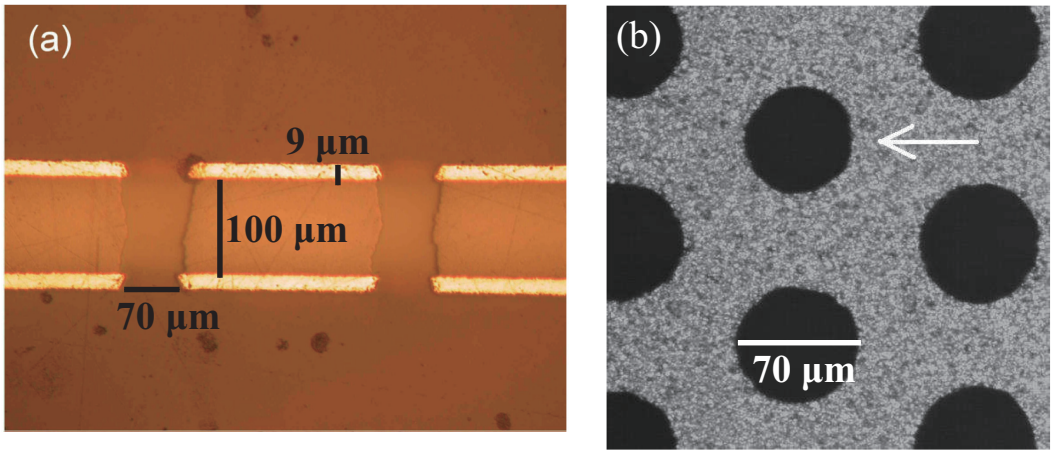

Figure 2.23: The GEM cross-section and surface view (Tamagawa et al., 2009). The thicknesses of insulator and electrode are 100 μm and 9 μm, respectively. The radius of through hole is 70 μm.

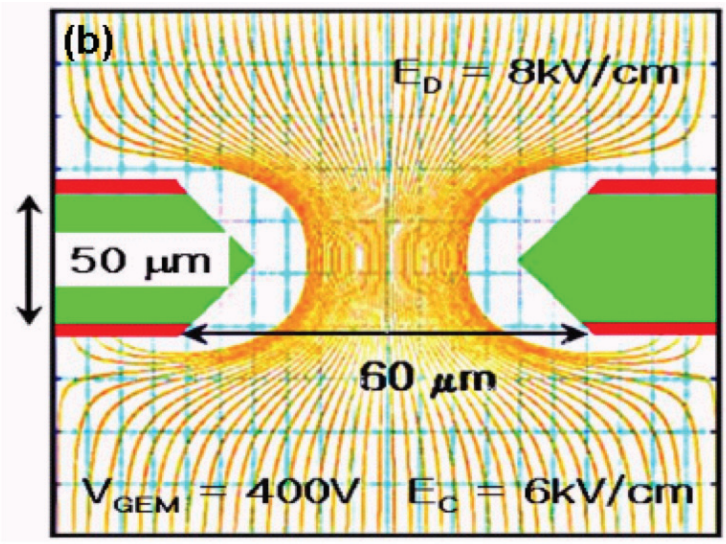

Figure 2.24: The electronic field of the through hole of GEM (Han & Kang , 2002). Yellow lines are electronic fields, red area are electrodes and green ares are insulator of GEM. The voltage between electrodes is 400 V and the electric field above and below GEM are 8 kV/cm and 6 kV/cm.

Chapter 3

REVIEW OF SWIFT J1753.5-0127

3.1 Discovery

Swift J1753.5–0127 was discovered with the Burst Alert Telescope (BAT) on-board *Swift* on May 30th 2005 (Palmer et al., 2005 and Burrows et al., 2005) The light curve of the BAT is shown in figure 3.1. The source flux peaked at $\sim$200 mCrab (2.4×10^{-11}erg cm^{-2} s^{-1} in the energy range from 2 to 10 keV) on July 9th 2005, and then gradually decreased for more than six months. Since 2006, the flux gradually increased again to as bright as $\sim$20 mCrab. Such a long lasting outburst is highly unusual in LMXBs.

The optical observation to find a bright optical counterpart of Swift J1753.5–0127 was performed on July 2nd 2005 (Halpern P. J., 2005), and the discovered counterpart with R$\sim$15.8 magnitude indicated the system to be a LMXB. Furthermore, the increase flux of a Hα line, which is typical for a LMXB in outburst, is detected. The optical star exhibits Hα line emission from the disk of circumstellar gas. The Hα measurements provide very useful information on the physical state of the disk by measuring the doppler shift. Double-peaked Hα lines originate in the outer region at distances from hundreds to thousands of R_s from the BH. The non-detection of any emission lines were obtained by the optical observation on July 3 (Torres et al., 2005a). The spectra showed a blue continuum with Hα line being the only emission line detected. It had an equivalent width (EW) of 3 $\AA$ and a full width at half maximum (FWHM) of 2000 km s^{-1} (Torres et al., 2005a).

The broad double-peaked Hα emission line was detected with EW of 3 $\AA$ on July 7, 10 11 and 12, which implies double-peaked separation of 1200 km s^{-1} and FWHM around 2000 km s^{-1} (Torres et al., 2005a). The broad double-peaked line had almost disappeared on August 11. The binary orbital period is reported to be 3.23 hrs (Zurita et al., 2008), which is the third shortest one of all the BHBs.

3.2 Failed state transition

A number of high energy studies of this source to investigate state transitions have been published. Figure 3.2 shows the light curve of the outburst and the observation epoch of the astronomy satellites. An analysis of *RXTE* observations of the outburst were reported in Ramadevi & Seetha, 2007 and the X-ray spectrum was found to be consistent with a power-law ($1.6 < \Gamma < 1.8$). Cadolle Bel et al. (2007) analyzed simultaneous *RXTE* and *INTEGRAL* data, which were also obtained during the 2005 outburst. The combined spectrum (3–400 keV) could be fit with

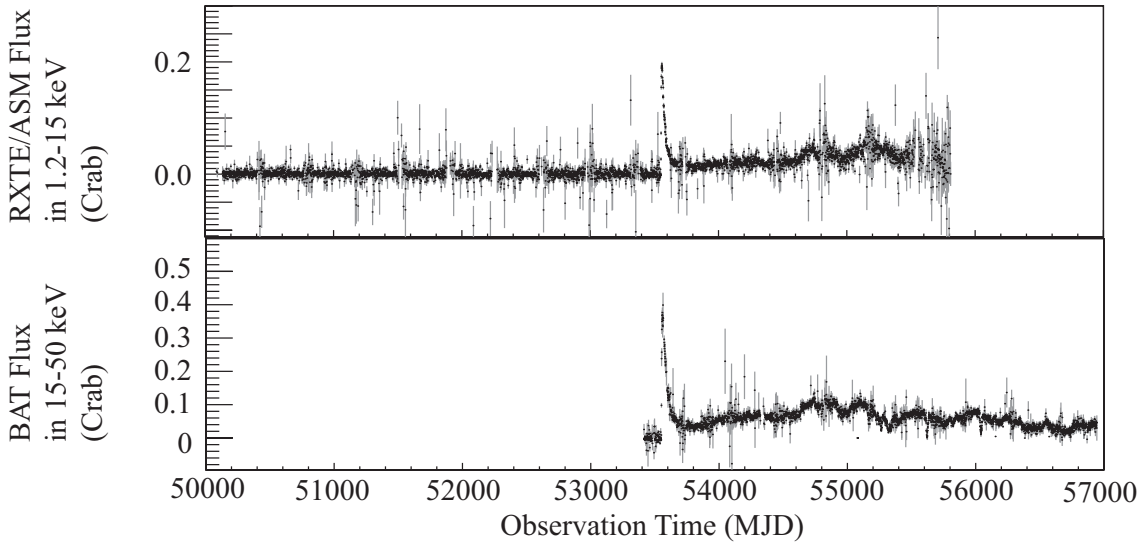

Figure 3.1: (Top) The light curve in the 1.2-15 keV energy band observed by the ASM. (Bottom) The light curve in the 15-50 keV energy band observed by the BAT. On May 30th 2005 (MJD 53551), Swift J1753.5–0127 was discovered by the detection of the outburst. Crab is the flux unit of 2.4×10^{-8}erg cm^{-2} s^{-1} in the energy range from 2 to 10 keV.

a Comptonization model modified by the disc reflection (kT ∼0–0.5 keV, kT_e ∼150 keV, τ ∼1), where kT, kT_e and τ are the temperatures of the black body, that of the electrons and the optical depth, respectively.

Spectroscopy of Swift J1753.5–0127 by *Suzazku* after the outburst revealed that the X-ray spectrum was explained by a typical low/hard spectrum model: powerlaw with a photon index ∼ 1.7 (Reynolds et al., 2010). *XMM-Newton* observations also show the low/hard X-ray spectrum (Miller et al., 2006). Figure 3.3 shows the count spectrum observed by the *Suzaku* satellite and the ratio of the best fit model to the data (Reynolds et al., 2010). The radiation components of the accretion disk is much smaller than the energy flux of the source during 0.6-2.0 keV. The temperature of the accretion disk was obtained to be 0.2 keV and the energy flux of the accretion disk was reported to be 3.9×10^{-10} erg s^{-1} cm^{-2} (Reynolds et al., 2010). They suggests the existence of the cooling disk in the low/hard state after the outburst (Miller et al., 2006 and Reynolds et al., 2010).

The state transition and the state quiescent of Swift J1753.5–0127 has not been reported since the outburst on May 2005. A failed transition during the outburst has been reported (Ramadevi & Seetha, 2007). Figure 3.4 shows the X-ray hardness-intensity diagram (HID) and light curves for the failed transition during the outburst, covering the above pointed observation. The hardness ratio did not remain constant during the whole outburst and the source softened between July 2009 (#5 in figure 3.4) and May 2010 (#7) (Soleri et al., 2013). The flux during 2005 outburst (#2) was larger but the hardness ratio was still larger, which means the photon from the disk was not large. The inner disk temperature ($T_{\rm in}$) and the photon index during the outburst of 2005 was estimated to be 0.2–0.4 keV and 1.6–1.8, respectively (Ramadevi & Seetha, 2007, Miller et al., 2006 and Sarkar et al., 2008). The inner cool disk which explains a lower temperature and the inner radius of the accretion disk was discussed (Miller et al., 2006, Ramadevi & Seetha, 2007 and Sarkar et al., 2008).

The column density ($N_{\rm H}$) of interstellar absorption has not been fixed observationally. Sev-

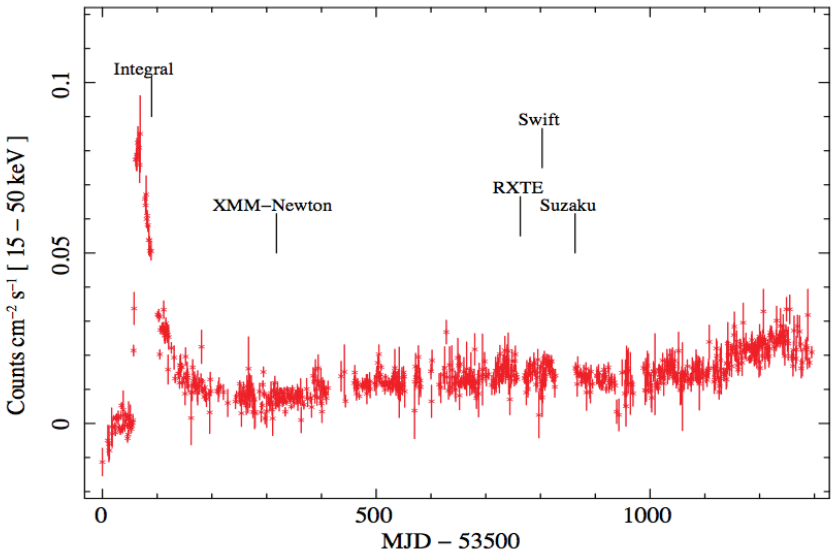

Figure 3.2: The light curve observed by the BAT (Reynolds et al., 2010) and the observation time of the *Integral* (Cadolle Bel et al., 2007), *XMM-Newton* (Miller et al., 2006), *RXTE* (Durant et al., 2009), *Swift* and *Suzaku* (Reynolds et al., 2010) satellites.

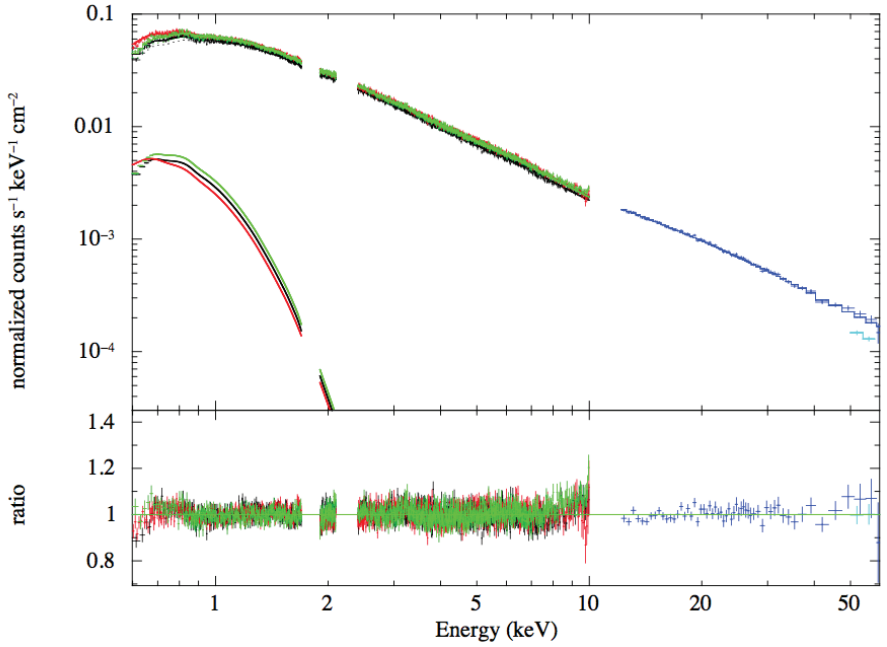

Figure 3.3: The count spectrum of Swift J1753.5–0127 observed the *Suzaku* satellite (Reynolds et al., 2010). The solid lines show the radiation components of the accretion disk.

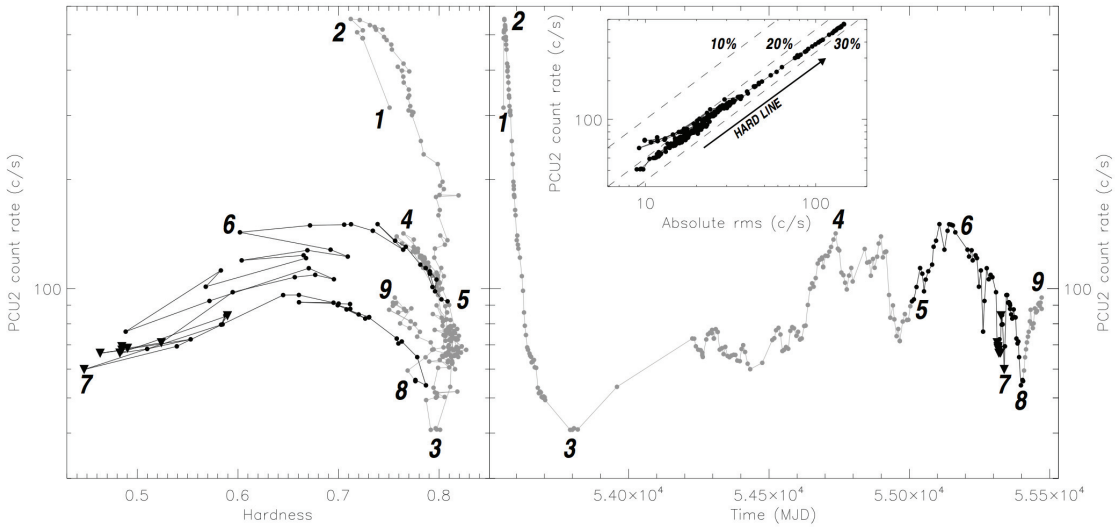

Figure 3.4: (Left) X-ray hardness-intensity diagram (HID) and (right) light curves (3.3–6.1 keV) of Swift J1753.5–0127 observed by RATE (Ramadevi & Seetha, 2007). The hardness is defined as the ratio of counts in the bands between 6.1 and 10.2 keV and 3.3 and 6.1 keV.

eral values of $N_{\rm H}$ were reported being $N_{\rm H} = 0.17\times10^{22}$ cm^{-2} (Miller et al., 2006) and $N_{\rm H} = 0.20-0.31\times10^{22}$ cm^{-2} (Reynolds et al., 2010). Zurita et al., 2008 reported that the distance was 5.9 kpc. The distance to the source and an inclination angle of the disk are also not determined because the optical and radio observations are not enough to define them (Cadolle Bel et al., 2007). The source $N_{\rm H}$ is comparable to or below the total galactic column density of this source direction, so that the source is located at 10 kpc or less.

3.3 Binary system

An orbit period ($P_{\rm orb}$) is reported to be 3.23 hrs (Zurita et al., 2008), which is the third shortest of all the BHBs: the first and second ones are MAXI J1659–152 ($P_{\rm orb}$ ∼2.4 hrs: Kuulkers et al., 2013) and Swift J1357.2-093313 ($P_{\rm orb}$ ∼2.8 hrs: Corral-Santana et al., 2013). The orbit period of Swift J1753.5–0127 is shorter than the other BHB systems (table 2.1). The short-periods can be obtained from the superhump modulation on the light curve of R-band (0.65 to 1.0 μm wave length). The changing shape and amplitude of the light curves would be explained by the changes in the shape or size of the disk and resonance between the Keplerian orbits and the orbital motion of the companion (Zurita et al., 2008 and Patterson et al., 2005).

The relation between mass ratio ($q = M_2/M_1$), $P_{\rm orb}$ and the disk precession ($P_{\rm prec}$) are obtained in Patterson et al. 2005. Some values of $P_{\rm prec}$ were reported to be ∼29 day (Zurita et al., 2008) and 420 day (Shaw et al., 2013) and the values of q are estimated to be 0.025 and 0.002, respectively. If the mass of a typical BH is ∼10 $M_\odot$ (table 2.1), the mass of the companions star is below 0.5 $M_\odot$.

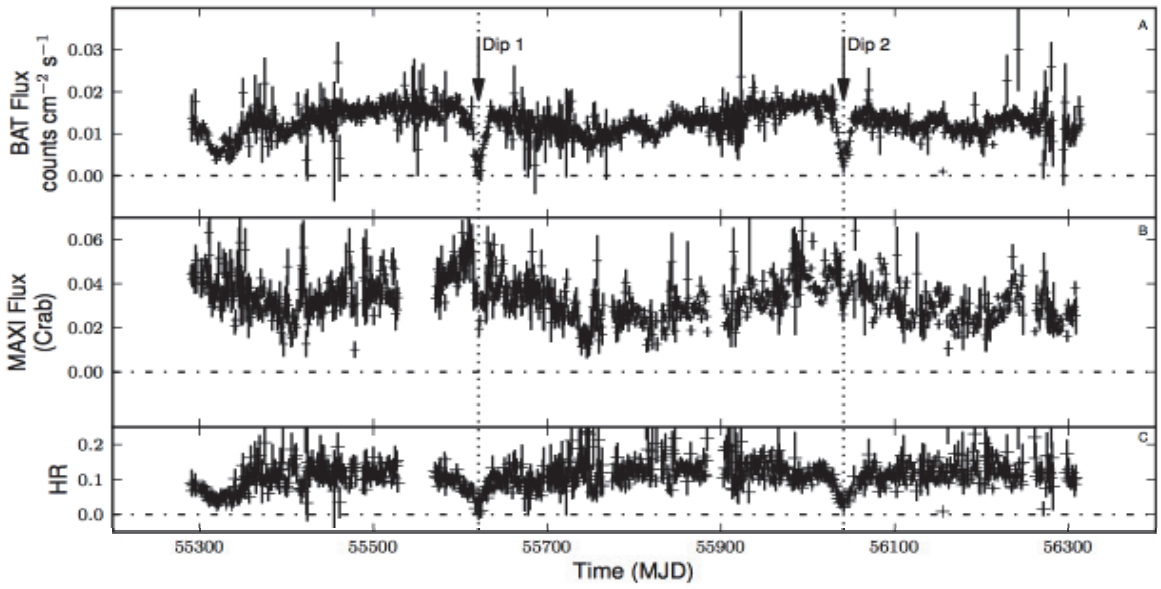

Figure 3.5: (A) The BAT light curve in energy range of 15–50 keV with a day binning (Shaw et al., 2013). (B) The light curve of 2–20 keV obtained by the GSC with a day binning. (C) The hardness ratio (HR) of the intensity in the energy range of 15–50 keV to that of 2–20 keV. Crab is the flux unit of 2.4×10^{-8}erg cm^{-2} s^{-1} in the energy range from 2 to 10 keV.

3.4 Hard X-ray dips

Dips in the energy ranges of 15–50 keV and 2–20 keV lasting for several tens days at Feb. 28th 2011 (MJD 55620) and Apr. 4th 2012 (MJD 56040) were observed by the BAT and GSC, as shown in figure 3.5. Shaw et al. 2013 reported a 420 day modulation associated with X-ray dips of the light curves as a possible eclipse by the warped disk. They also reported that the dips in the energy range of 15–50 keV (hard-dip) could be attributed to a warped disc structure that obscures the hard X-ray emitting region entirely while leaving the softer region mostly visible (Shaw et al., 2013). The humps in the light curves in 2–4 keV (soft-hump) with several ten days were reported in 2009 (Negoro et al., 2009 and Negoro et al., 2010). Shaw et al. 2013 have not searched the X-ray below 2 keV. If there were the soft humps at Feb. 28th 2011 and Apr. 4th 2012, the soft-humps and hard-dips could not be explained by the eclipse. To investigate the short-term variation which corresponds to the hard dips in the energy ranges of 15–50 keV and 2–20 keV lasting for several tens days, the key of this study is to analyzed the observation data below 2 keV.

Chapter 4

INSTRUMENTATION

4.1 *MAXI*

4.1.1 Mission Characteristics

In Sep. 2009, the Monitor of All-sky X-ray Image (MAXI: Matsuoka et al., 2009) started its operation on board the International Space Station (ISS), carrying Gas Slit Camera (GSC: Mihara et al., 2011 and Sugizaki et al., 2011) and Solid Slit Camera (SSC: Tsunemi et al., 2010 and Tomida et al., 2011). Figure 4.1 shows a schematic view of MAXI. The ISS flies a low earth orbit (perigee of 336 km and apogee of 346 km), and an orbital inclination of 52°, corresponding to an orbital period of about 92 minutes. MAXI is designed to detect new transients and monitor the radical changes of flux from sources (e.g., Nakahira et al., 2013). In fact, MAXI has detected several outbursts from new BHBs during the three years since the launch (e.g., MAXI J1659–125, Negoro et al., 2010; MAXI J1543-564, Negoro et al., 2011), also providing us with X-ray data continuously over the entire period of an outburst.

4.1.2 GSC

The GSC contains six units of a conventional slit camera. The slit camera is composed of 12 position sensitive proportional counters with six carbon anodes. Each unit consists of two one-dimensional proportional counters and slit & slat collimation (figure 4.2). The GSC covers an energy range of 2.0–20.0 keV with an energy resolution (FWHM) of 18% at 5.9 keV. The GSC is capable of detecting a 25 mCrab and 8 mCrab source at an exposure of one orbit and one day ($\sim$15 orbits), respectively. For each unit, field of views (FOVs) of the ISS scanning direction (θ) and slit direction (ϕ) are 1.5° and 80°, respectively, as shown in figure 4.3. Six counters are placed in the horizontal direction, thus they are called GSC-H, while the others in the zenith direction, called GSC-Z, as shown in figure 4.4. Therefore two units of both the GSC-H and GSC-Z cover a very wide angular range of 160° for the slit direction.

Although the proportional counters are one-dimensional (the slit direction) cameras, we can see a two-dimensional image, which is obtained with the triangular response of a slat collimator according to the ISS movement. An intersection of the slit image and the triangular response image corresponds to a source location in the sky (figure 4.5). The image in figure 4.5 is pointed spread function (PSF).

The GSC covers about 76% and 96% of the sky for one orbit and one day observation, respectively. There are still inaccessible regions of the two polar region (10°) and the solar

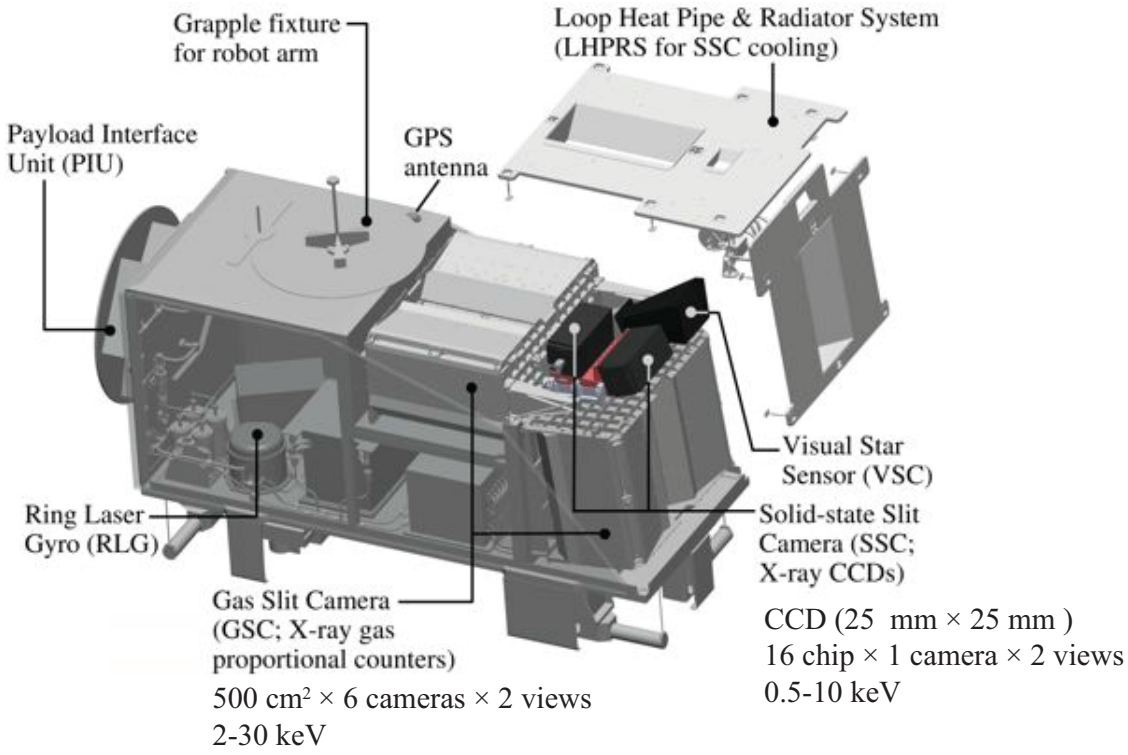

Figure 4.1: A schematic view of MAXI (Matsuoka et al., 2009). The volume is $1.85 \times 0.8 \times 1$ m^3 and the wight is 520 kg (GSC 160 kg and SSC 11 kg).

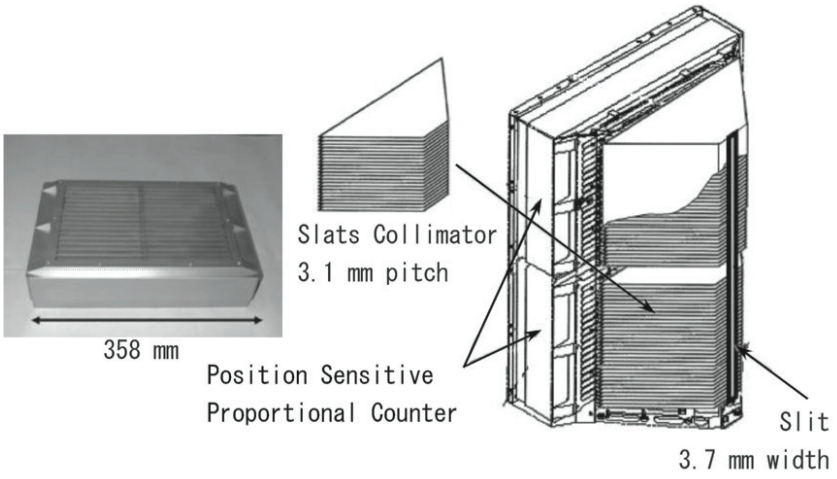

Figure 4.2: A schematic view of the unit of the GSC (Matsuoka et al., 2009). Two counter are set in the unit. The collimator is placed on the unit.

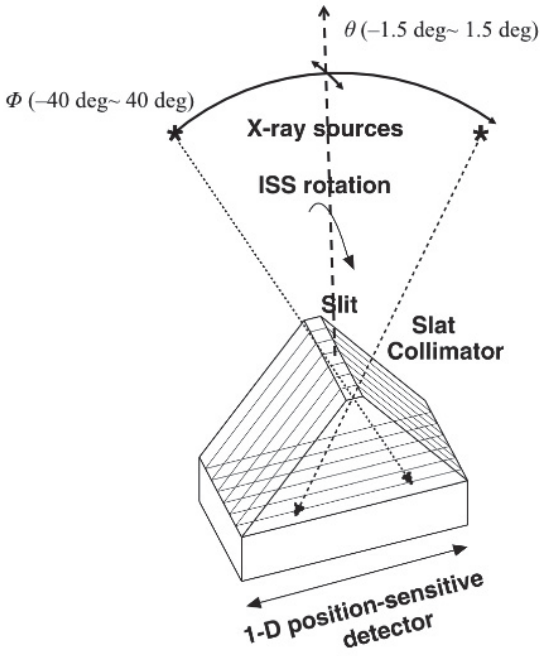

Figure 4.3: Definition of the angle θ and ϕ (Matsuoka et al., 2009).

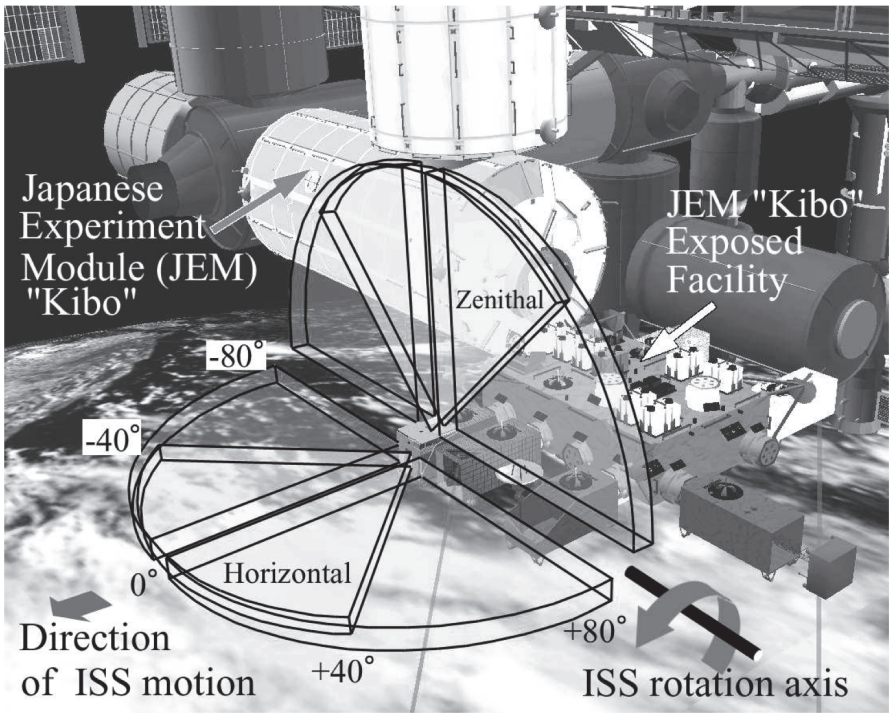

Figure 4.4: FOVs of the GSC-H and GSC-Z onboard MAXI (Ueno et al., 2009).

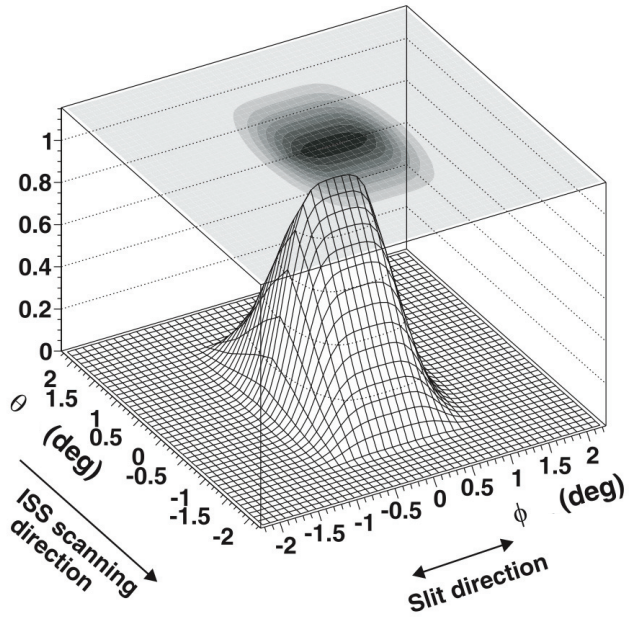

Figure 4.5: Typical sample of PSF (Matsuoka et al., 2009). A slit collimator has a triangle response.

vicinity ($\pm 4^{\circ}$), The polar region corresponds to unobservable regions around end directions of the ISS pitch axis. Thus, the GSC does not always monitor all X-ray sources: there are always unobservable regions.

The gas counters of the GSC consist of two layer to distinguish X-ray events from cosmic-ray events. X-ray events are detected in one layer, while the cosmic-ray events are detected in both layers simultaneously (so-called the anti-coincidence). Exceptionally, events detected at the counter edge ($\phi \sim \pm 40^{\circ}$) cannot be distinguished, because cosmic-rays that cause such events interact only with upper layer.

The proportional counters are filled with a gas mixture of 99% Xe and 1 % CO_2 by volume at 1.4 atm, and its quantum efficiency is shown in figure 4.6. The gas of CO_2 is used as quencher. The efficiency for X-rays between 4 and 10 keV is above 80 %. The edge structure at 34.6 keV is caused by Xe K-edge absorption. The counters detect incident X-ray photons from vertical to the $\pm 40^{\circ}$ slat direction.

4.1.3 SSC

The SSC is a slit camera with an array of 32 X-ray CCD chips each of which is one inch square. The energy range of the SSC is 0.5–12 keV with an energy resolution (FWHM) of $\sim$ 150 eV at 5.9 keV. The pixel number for the X-ray CCD chip is 1024×1024, and the pixel size is 24 μm × 24 μm. The effective area is $\sim$ 25 mm×25 mm. A SSC unit comprise 16 X-ray CCDs chips aligned in a 2×8 array as shown in figure 4.7. The total X-ray detection area of the SSC (32 CCD units) is about 200 cm^2. The CCD is sensitive to optical and infrared light that degrades the performance of the X-ray detection. In order to avoid to detect optical and infrared light, aluminum of 0.2 μm thickness is coated on the CCD surface.

Each SSCU has a collimator and slit unit (CSU). Figure 4.8 is a schematic view of the CSU.

Table 4.1: Specification of MAXI slit cameras.

	GSC: Gas Slit Camera	SSC: Solid-state Slit Camera
X-ray Detector Type	one-dimensional PSPC; Xe (99%)+ CO_2 (1%)	X-ray CCD; 1024×1024 pixels
A number of Modules	12 of PSPC	32 of CCD
X-ray Energy Range	2–30 keV	0.5–12 keV
Energy resolution	18% (5.9 keV)	150 eV (5.9 keV)
Total Geometrical Area	5350 cm^2	200 cm^2
Absolute time resolution	0.1 ms (minimum)	5.8 s (nominal)
Weight	160 kg	11 kg
Slit area for camera unit	20.1 cm^2	1.35 cm^2
Field of View	$1^\circ.5 \times 160^\circ$	$1^\circ.5 \times 90^\circ$
Detector position resolution	1 mm	0.025 mm (pixel size)
Localization accuracy	$0^\circ.1$	$0^\circ.1$

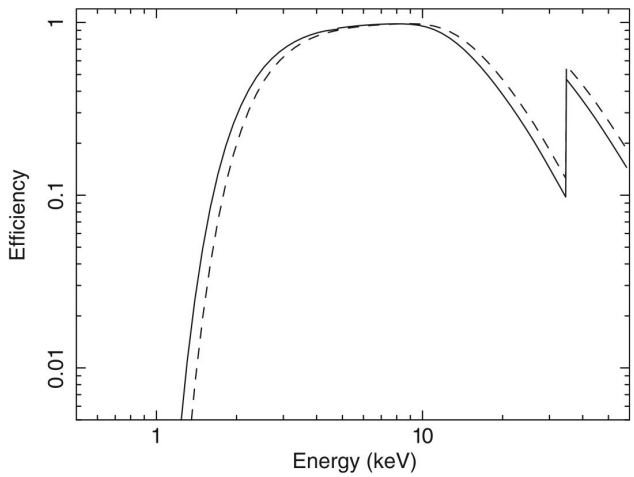

Figure 4.6: X-ray Detection efficiency of the GSC by energy (Matsuoka et al., 2009). The solid and dashed lines indicate the efficiency for normal-incident X-rays and that of incident X-rays from 40°.

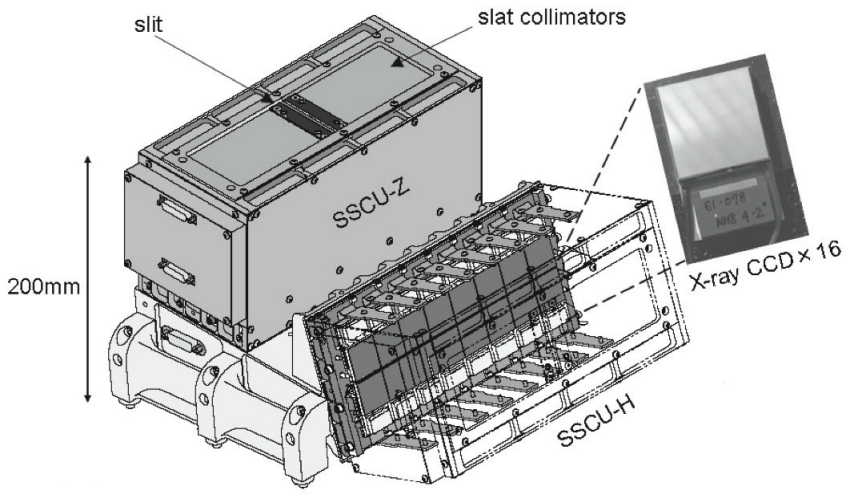

Figure 4.7: Schematic view of a SSCU. The unit is made of aluminum. The SSCU is 224×112×124 mm, and 3.9 kg including a collimator and slit unit.

The collimator consists of thin sheets made of phosphor bronze with the thickness of 0.1 mm. There are 24 sheets with 2.4 mm interval that are placed 5.0 mm above the CCD units. The surface of the collimator sheet is chemically etched to suppress the X-ray reflection, and plated with black chromium to suppress the optical light. The collimator sheet pitch determines the narrower FOV to be $3^{\circ}.0$ in bottom-to-bottom (θ_1 in figure 4.8). A scan of an object with constant flux forms a triangular response, whose full width at the half maximum (FWHM) is $1^{\circ}.5$.

The combination of eight CCD units and the slit determine the FOV to be $1^{\circ}.5 \times 90^{\circ}$ (θ_3 in figure 4.8). The slit of the SSC consists of two tungsten bars with sharp edges. The width between the two edges is 2.7 mm. The angular resolution depends on the acquisition angle which is the angle between the incident X-ray direction and the normal of the slit plane. For larger acquisition angles, angular resolution becomes better, while the effective area becomes smaller by a cosine factor.

About 29% of the entire sky is not covered by the SSC in an orbit scan, because of the polar region and the solar vicinity. It takes about 70 days to cover the unobservable region, depending on the orbital precession period of the ISS. The region of the solar vicinity is too bright to block optical light with the aluminum coat on the CCD surface. Then it takes about a half year to obtain an actual all-sky image. Figure 4.9 shows the effective area of the SSC.

4.2 *Swift* satellite

4.2.1 Mission Characteristics

To investigate gamma-ray bursts (GRBs) which are the most powerful explosions in the universe, the *Swift* satellite was launched on Nov. 20th 2004, mounting the burst alert telescope (BAT), the X-ray Telescope (*Swift* XRT) and UV/Optical Telescope (UVOT). Figure 4.10 shows a schematic view of the *Swift* satellite. The *Swift* operation during ten years contributed to our

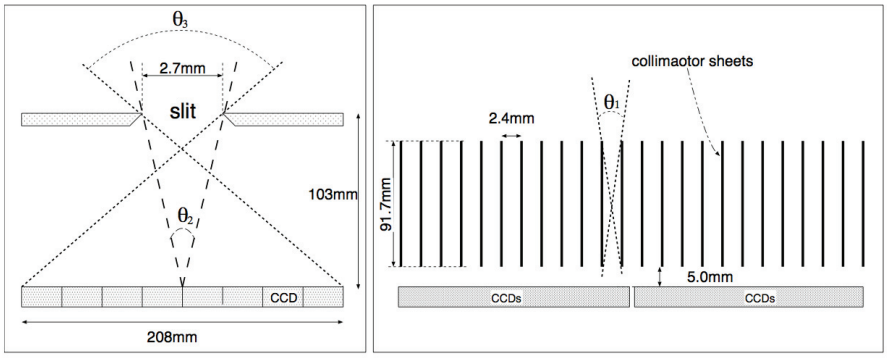

Figure 4.8: Schematic view of a collimator and slit unit (CSU) in an SSCU (Tomida et al., 2011). The left figure shows the positional relation between the slit and CCDs. The right figure, perpendicular to the left figure, shows the 24 collimator sheets and CCDs.

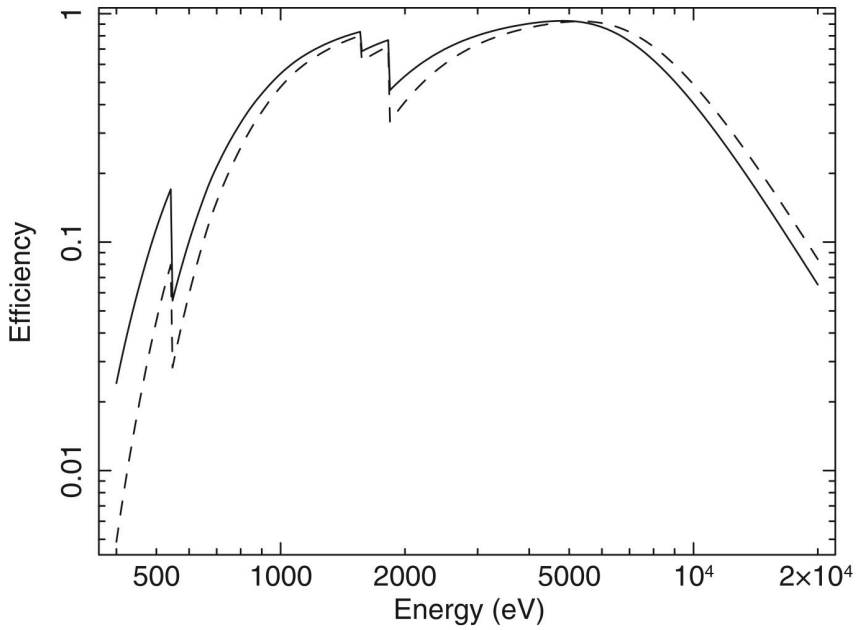

Figure 4.9: The efficiency of the SSC (Tsunemi et al., 2010). The dashed line shows the efficiency at the incident angle 0°. The solid line shows the efficiency at the incident angle 40°.

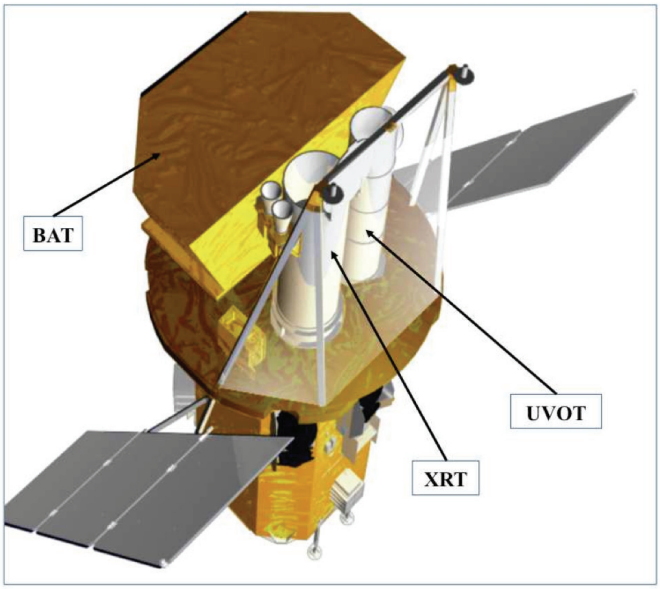

Figure 4.10: A schematic view of *Swift* satellite (http://www.swift.psu). The BAT, XRT and UVOT are located on the same side.

understanding of an impressive variety of targets including AGNs, supernovae, pulsars, microquasars, novae, variable stars, comets, and much more, because the multi-wavelength instrumentation and fast scheduling capabilities are very useful for the violent variation of high energy astrophysics.

The BAT is a highly sensitive large FOV instrument designed to provide critical GRB triggers and 4-arcmin localization accuracy, using a coded mask and CdZnTe pixel sensors. The *Swift* XRT is an X-ray CCD imaging spectrometer designed to measure the position, spectrum, and brightness, using photon counting techniques. The UVOT is UV/optical telescope co-aligned with the *Swift* XRT, using photon counting techniques which is more similar to typical X-ray telescopes than to typical optical telescopes.

4.2.2 *Swift* XRT

The *Swift* XRT assembly consists of X-ray mirrors and X-ray CCDs. Figure 4.11 and 4.12 show a schematic view and a photograph of the *Swift* XRT. The mirror modules consist of 12 concentric gold-coated Ni shells, focusing X-rays on the surface of the CCD with a focal length of 3500 mm. The CCD is CCD-22, which is designed for the *EPIC MOS* instruments on XMM and its imaging area is $\sim 24\times24$ mm^2. The number of CCD pixels is 600×602 and the size is 40×40 mm^2. The basic parameters of the *Swift* XRT configuration is summarized in table 4.2.

Figure 4.13 shows the PSF measured by calibration sources which were positioned at 130 m from the mirrors. Two point sources were displaced by 20 arcsec. The PSF is a shape with FWHM of about 7 arcsec, fitted by a single gaussian function for the distribution. Figure 4.14 shows an example of the PSF profiles at 7 arcmin off-axis. The PSF is slightly blurred on axis and better at 7 arcmin off-axis due to the fact that the CCD is intentionally offset along the optical axis from the best on-axis focus.

There are four read out modes of the *Swift* XRT:Photodiode (PD), Windowed Timing (WT),

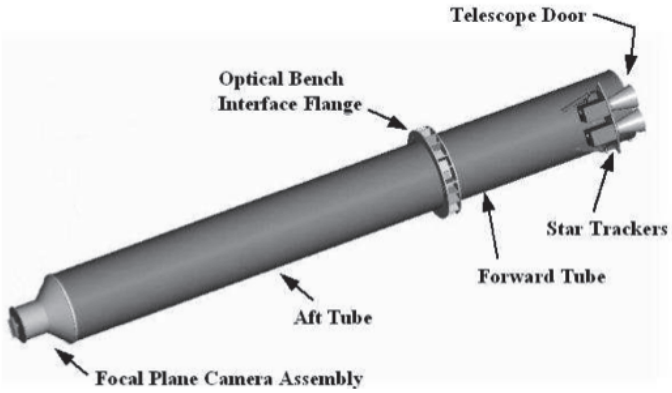

Figure 4.11: A schematic view of the *Swift* XRT (http://www.swift.psu).

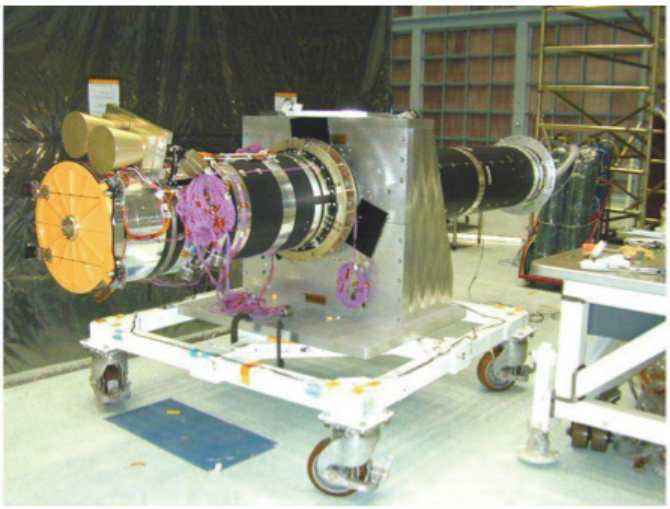

Figure 4.12: A photograph of the *Swift* XRT (http://www.swift.psu).

Table 4.2: Specification of the *Swift* XRT of the *Swift* satellite (David N. Burrows, 2005).

Telescope:	Wolter I (3.5 m focal length)
Detector:	e2v CCD-22
Detector Format:	600 × 600 pixels
Pixel Size:	40 μm × 40 μm
Readout Modes:	Image (IM)
	Photodiode (PD)
	Windowed Timing (WT)
	Photon-Counting (PC)
Timing Resolution:	2.5 s(IM)
	0.14 ms (PD)
	1.8 ms (WT)
	2.5 s (PC)
Pixel Scale:	2.36 arcsec/Pixel
Field of View:	23.6 × 23.6 arcminutes
PSF:	18 arcsec HPD @1.5 keV
	22 arcsec HPD @8.1 keV
Position Accuracy:	3 arcsec
Energy Range:	0.2–10 keV
Energy Resolution:	140 eV@5.9 keV (at launch)
Effective Area:	∼124 cm^2 @1.5 keV
	∼20 cm^2@8.1 keV
Sensitivity:	2×10^{-14} erg cm^{-2} s^{-1} in 10^4 seconds.
Operation:	Autonomous

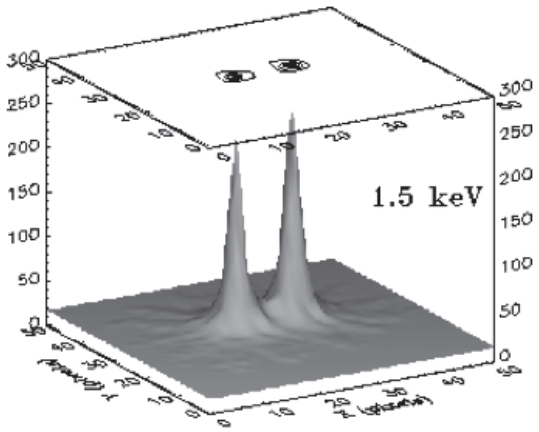

Figure 4.13: The *Swift* XRT image of two point sources displaced by 20 arcsec, made during the mirror calibration (http://www.swift.psu.edu/xrt/optics.html).

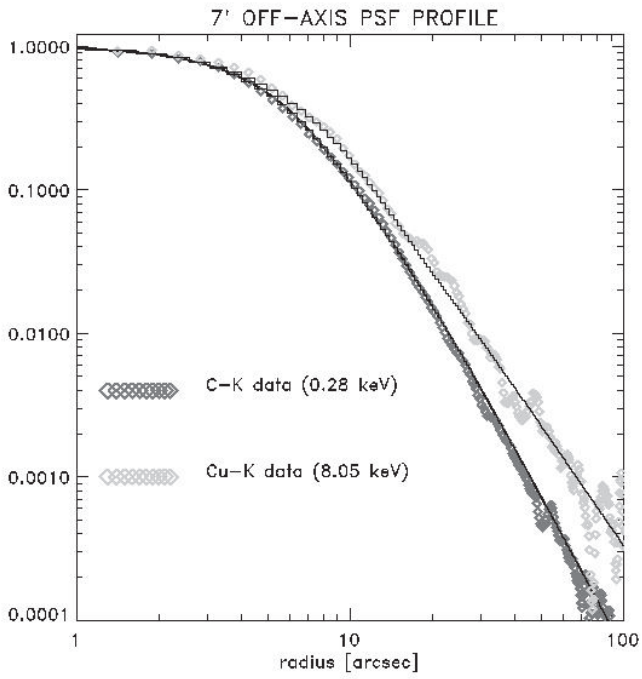

Figure 4.14: An example of PSF profile on the focus plane of CCD at 7 arcmin off-axis of 0.28 keV and 8.05 keV. (http://www.swift.psu.edu/xrt/images/psf.jpg).

Imaging (IM) and Photon-counting (PC) modes. The PD mode is designed to produce accurate timing information for extremely bright sources, such as GRBs. The PD mode can produce a light curve with high time resolution of 0.14 ms. Charge is accumulated in the serial register during each parallel transfer. The charge is integrated from the entire field of view. Flux below 2 Crabs can be managed in this mode.WT mode is a high gain mode to achive high resolution timing (1.8 ms) with one dimension position information and spectroscopy. A 200 column window covers the central 8 arcminutes of the FOV with the WT mode. This mode can measure flux below 1 Crab without pile-up. The IM mode is a normal imaging exposure and readout, similar to PC mode. The PC mode mainly retains full imaging and spectroscopic resolution, but the time resolution is only 2.5 s. Pile-up occurs when the CCD in the PC mode is irradiated by flux over 1 mCrab.

The effective area was measured at five energy points (C-K:0.28 keV, Al-K:1.49 keV, Ti-K:4.51 keV, Fe-K:6.40 keV, Cu-K:8.05 keV) before the launch. The effective areas of PD and WT modes are shown in figure 4.15 and 4.16. The effective area achieved $\sim$124 cm^2 at 1.5 keV and $\sim$20 cm^2 at 8.1 keV. The energy resolution for the flight CCD is shown in figure 4.17. The difference between the calculated fano-limited resolution and the measured resolution is increased below about 500 eV, because below approximately 500 eV the effects of charge trapping and loss to surface states become significant.

4.2.3 BAT

The BAT localizes and defines the position of the event from the image pattern of the mask. The sensor is sensitive to energies of 15-150 keV and is composed of 32,768 pieces of 4 mm square

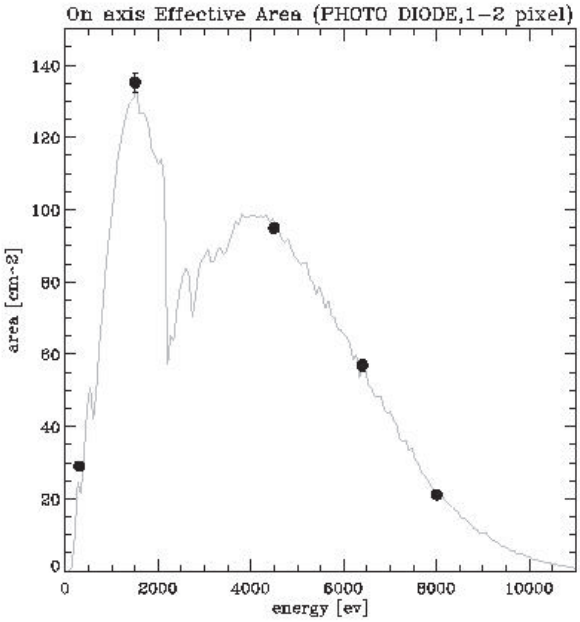

Figure 4.15: The effective area of *Swift* XRT simulated (solid line) and measured (black points) performing in PD mode (http://www.swift.psu.edu/xrt/optics.html).

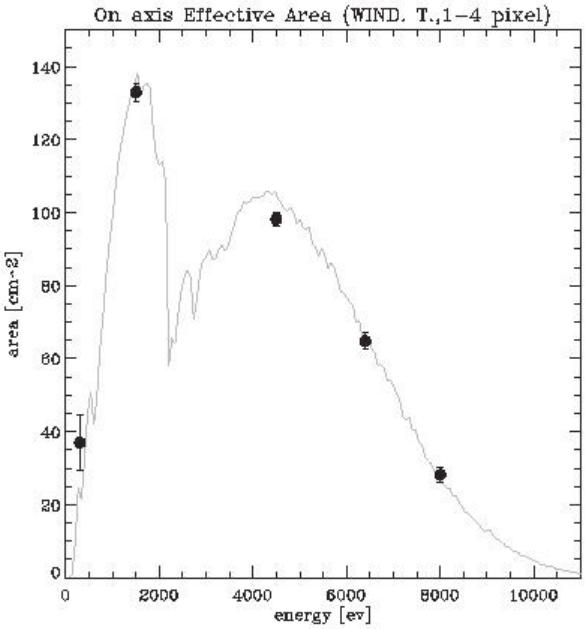

Figure 4.16: The effective area of *Swift* XRT simulated (solid line) and measured (black points) performing in WT mode (http://www.swift.psu.edu/xrt/optics.html).

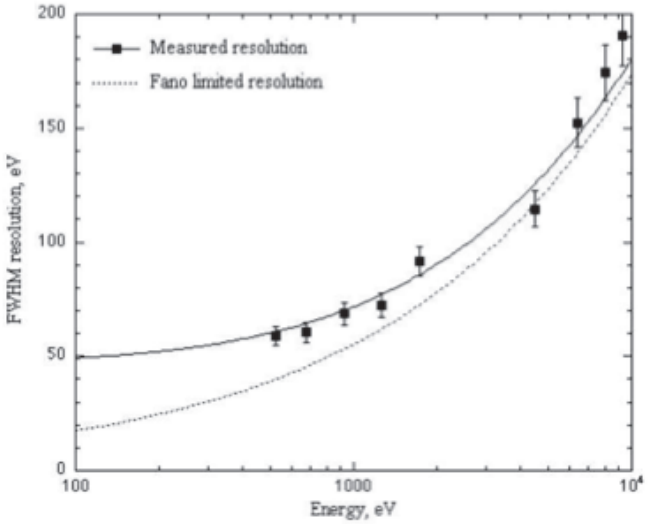

Figure 4.17: The energy resolution of the CCD in the *Swift* XRT with the IM mode (http://www.swift.psu.edu/xrt/fpca.html). The dashed line is the ideal (Fano-limited) resolution. The solid line is the predicted resolution.

CdZnTe (CZT) and the geometrical area is 5200 cm^2. The thickness of the CZT piece is 2 mm. The coded-mask located 1 meter behind the CdZnTe sensor is composed of ∼52,000 lead tiles, as shown in figure 4.18. The Pd_{67} tiles are 5 mm square and 1 mm thick. The coded pattern is completely random and the surface is 2.4 m × 1.2 m with a 50% filing factor, which yields the wide FOV of $100^{\circ} \times 60^{\circ}$. The FOV of the sensor depends on the location of the source, as shown in figure 4.19.

The basic properties of BAT are summarized in table 4.3. A typical spectrum of ^{57}Co is shown in figure 4.20. The energy resolution achieved is ∼7 keV (FWHM) at 122 keV. A point spread function of 17 arcmin. For detection of a point source with 5σ, the exposure time required is shown in figure 4.21.

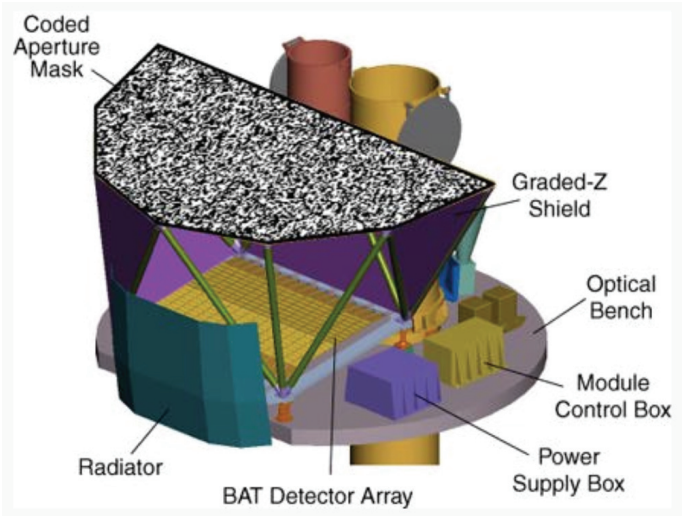

Figure 4.18: A schematic view of the BAT. The coded mask of the random pattern is located 1 m from the CdZnTe.

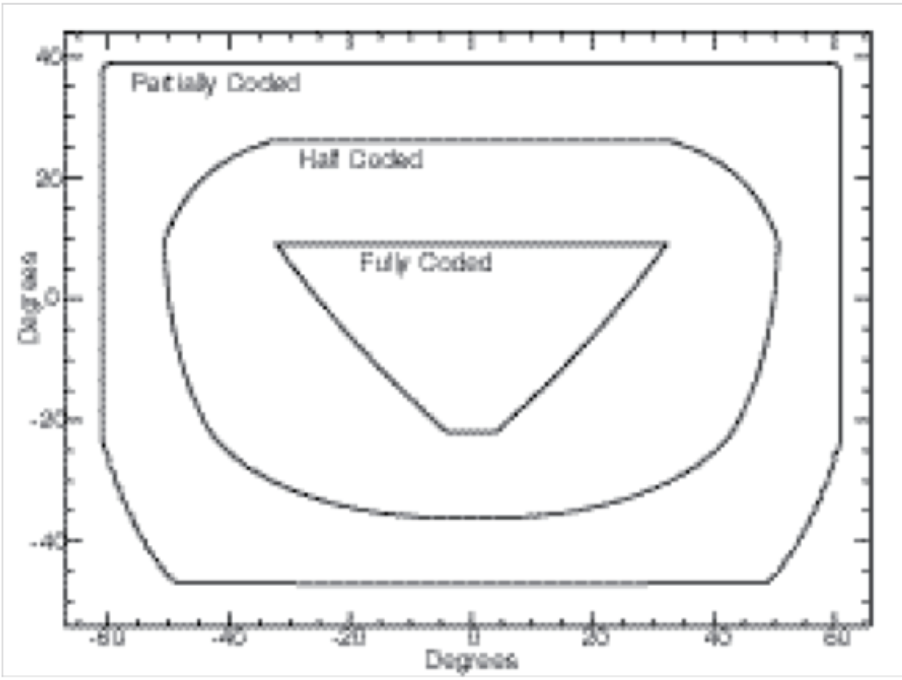

Figure 4.19: The FOV of the BAT with the 0%, 50% and 100%-coding counters (Barthelmy et al., 2005).

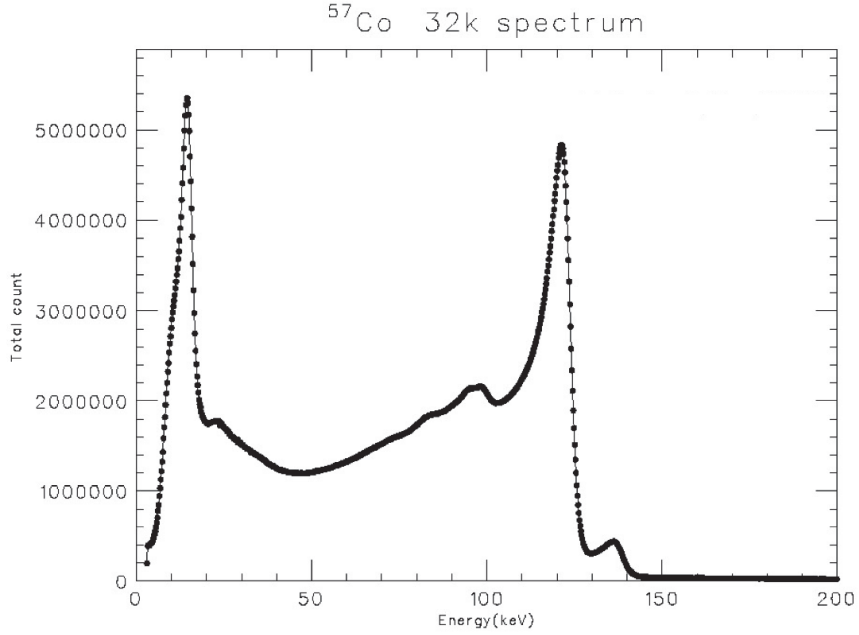

Figure 4.20: CZT spectrum of ^{57}Co (Barthelmy et al., 2005). The 14, 122, and 136 keV lines are detected. Energy resolution is ∼7 keV (FWHM) at 122 keV.

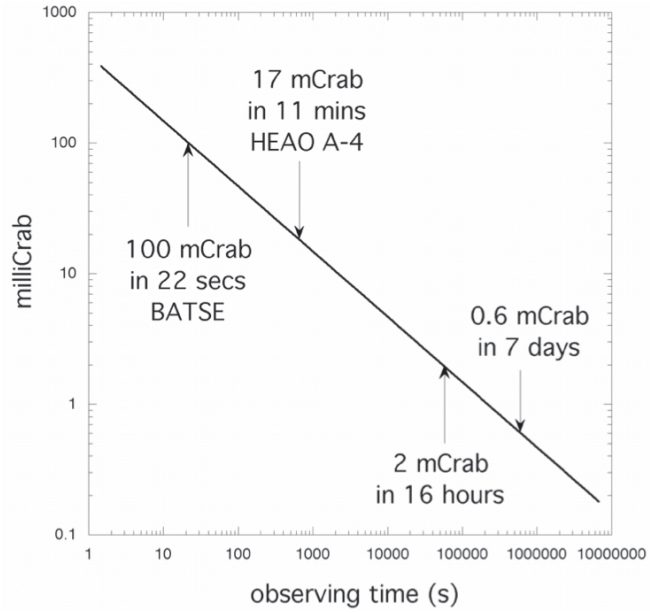

Figure 4.21: 5σ Detection sensitivity for the source with different fluxes as function of exposure time (Barthelmy et al., 2005).

Table 4.3: Specification of the BAT of the *Swift* satellite (Barthelmy et al., 2005).

Energy Range:	15–150 keV
Energy Resolution:	7 keV (at launch)
Aperture:	Coded mask, random pattern, 50% open
Detecting Area:	5240 cm^2
Detector Material:	CdZnTe (CZT)
Detector Operation:	Photon counting
Field of View:	1.4 sr (half-coded)
Detector Elements:	256 Modules of 128 elements/Module
Detector Element Size:	$4.00 \times 4.00 \times 2.00$ mm^3
Coded Mask Cell Size:	$5.00 \times 5.00 \times 1.00$ mm^3 Pb tiles
Instrument Dimensions:	2.4 m $\times$ 1.2 m $\times$ 1.2 m
Telescope PSF:	17 arcmin
Source Position Accuracy :	1–4 arcmin
Sensitivity :	$\sim 10^{-8}$ erg s^{-1} cm^{-2}
Number of bursts detected:	over 100 yr^{-1}

Chapter 5

SPECTRAL SOFTENING OF SWIFT J1753.5–0127

5.1 Observations and data reduction

5.1.1 Monitoring observations with *MAXI* and *Swift*

The monitor observation of Swift J1753.5–0127 has been performed by *MAXI* and *Swift*. The observation data of *MAXI* and *Swift* have been stored since Aug. 2009 and Feb. 2005, respectively. We used both data between Aug. 15th 2009 and Dec. 30th 2012 to investigate the ratio of the X-ray intensities between the 0.7-20 keV and 15-50 keV energy bands.

We extracted the GSC data from the event files processed with the *MAXI* standard analysis software (Sugizaki et al. 2011 and Nakahira et al. 2013 [1]). The GSC has been operated with the standard voltage of 1650 V and the reduced voltage of 1550 V, to abort to discharge on the electrodes of GSC. Thus, the event files include the data obtained by the GSC operated with voltage of 1650 V and 1550 V. We extracted the source photons from a circle centered at the target position with a radius of $2^\circ.0$ and the background photons from an annular region between an inner and an outer radius of $2^\circ.0$ and $3^\circ.0$ as shown in figure 5.1.

Because the various background components (hot pixel and photons from the sun and moon) in the SSC data are obstruction in the way of analysis (Tsunemi et al., 2010), we processed the SSC data from the event files as following order. We first discarded the hot pixel events using the *cleansis* ftool. To exclude photons from the sun or the moon, we accumulated events over a good time interval (Daikyuji et al., 2010). We used the GRADE012 events above 505 ch ($\sim$1.85 keV = Si edge) and the GRADE0 (Tomida et al., 2011) events below 505 ch. We extracted the source photons from a circle centered at the target position with a radius of $1^\circ.5$, and the background photons from a circle with a radius of $3^\circ.0$ excluding a circular region within $1^\circ.5$ from the target.

5.1.2 Pointing observations with the *Swift* XRT

Ten target-of-opportunity (ToO) observations with the *Swift* XRT summarized in table 5.1 were performed during the short-term variation around MJD [2] 56040. All observations were performed in the Windowed Timing (WT) mode to avoid pile up events (§ 4.2.2).

[1] http://repository.tksc.jaxa.jp/pl/dr/AA0061914004

[2] Modified Julian Date was introduced by the Smithsonian Astrophysical Observatory in 1954

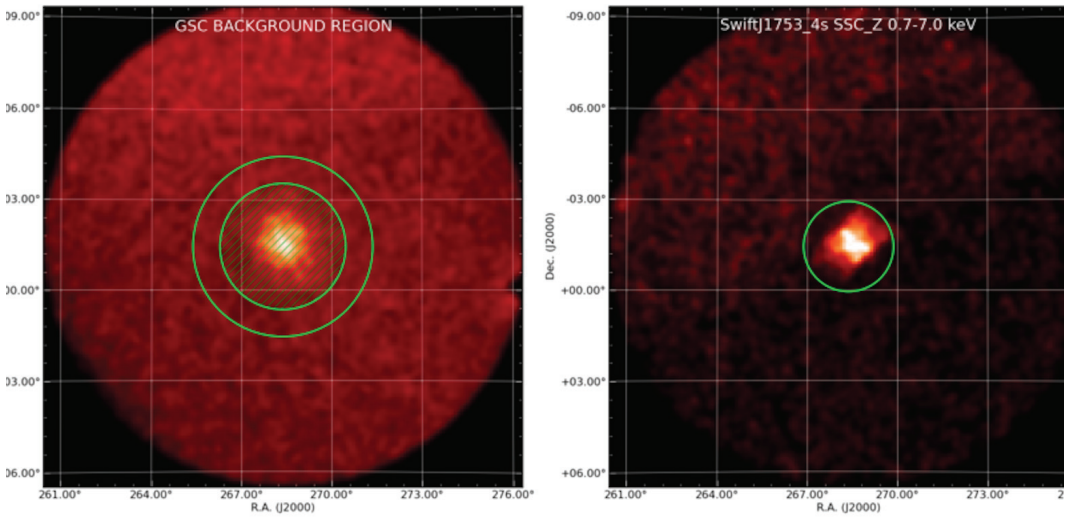

Figure 5.1: (Left) The image of Swift J1753.5–0127 with the GSC. (Right) The image with SSC. The hatched green circle is the source region and the concentric layer is the background region of GSC. The green circle is the source region of the SSC.

Table 5.1: The ToO data of Swift J1753.5–0127 by the *Swift* XRT.

Observation ID	UT	MJD	Duration [1]	Count Rate [2]	Mode
0003123022	April 20th 2012 T 07:35:59	56037	1.9	95.5±0.2 (98.8%)	WT
0003123023	April 22th 2012 T 06:07:02	56039	1.5	80.2±0.2 (99.3%)	WT
0003123024	April 24th 2012 T 17:24:55	56041	1.0	116.7±0.2 (99.1%)	WT
0003123025	April 26th 2012 T 09:44:50	56043	1.2	110.0±0.3 (99.0%)	WT
0003123026	April 28th 2012 T 16:21:19	56045	0.5	111.8±0.5 (98.8%)	WT
0003123027	April 30th 2012 T 14:44:35	56047	1.0	109.0±0.3 (98.8%)	WT
0003123028	May 2th 2012 T 22:56:59	56049	0.8	89.6±0.3 (99.1%)	WT
0003123029	May 3th 2012 T 18:07:13	56050	1.1	78.9±0.3 (98.8%)	WT
0003123030	May 6th 2012 T 11:51:15	56053	1.0	61.8±0.3 (98.8%)	WT
0003123031	May 8th 2012 T 05:37:11	56055	1.1	51.1±0.2 (98.8%)	WT

[1] Total exposure time for the *Swift* XRT (ks).
[2] Background-subtracted source count rate (cts/s). The parenthetic numbers indicate the ratio of the background-subtracted source count to the unsubtracted one.

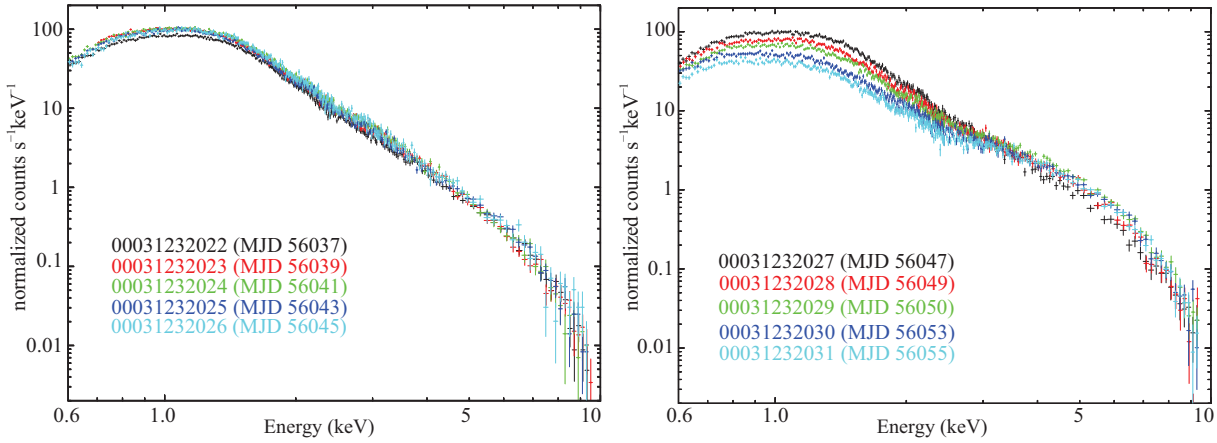

Figure 5.2: The count spectra observed during the ten *Swift* XRT ToOs during S4.

We extracted the XRT archival data using the web tools [3] which were provided by the UK Swift Science Data Center at the University of Leicester. Figure 5.11 shows the net spectrum observed by the *Swift* XRT. The calibration team of the *Swift* XRT recommends that users should analyze the data in the energy range of 0.6-10 keV with a systematic error of 3%, because there are still some problems in the calibration of the WT.

5.2 Light curves and hardness

In figure 5.3, we show the light curves in the energy ranges of 0.7–1.7 keV (SSC), 2–4 keV, 4–10 keV (GSC), and 15–50 keV (BAT), and the hardness ratio of 15–50 keV to 2–4 keV. Each time bin of the light curves is set to a day, which is long enough to obtain high signal to noise ratios. There are gaps in the GSC light curves between MJD 55529 and 55570, because the source was out of the FOV of the GSC during the period when the GSC FOV was close to the direction of the rotation axis of the ISS. The SSC data points were fewer than GSC, because the FOV of the SSC was narrower than that of the GSC.

The four short-term variation on MJD 55172 (Dec. 7th 2009), 55319 (May 3th 2010), 55620 (Feb. 28th 2011) and 56040 (Apr. 23th 2012) had the characteristic of a decrease of the hard X-rays (15–50 keV) in figure 5.3. Hereafter, we call the four events as S1 (MJD 55164–55180), S2 (MJD 55311–55327), S3 (MJD 55612–55628), and S4 (MJD 56032–56048), respectively. Furthermore, the increases of X-rays in the energy range between 0.7 and 1.7 keV were discovered lasting for a few tens of days and the variation of the increase is ∼ten times in the short-term variation of S4, as shown in figure 5.4. The increase in the energy range between 0.7 and 1.7 keV cannot be explained by the eclipse which have been introduced for explaining the short-term variations in Shaw et al., 2013. If the eclipse occurred in the short-term variation, the X-ray photons in the lower energy are easier to be absorbed by the materials than the X-ray photons in the higher energy. On the other hand, the state transitions can explain the increases of X-rays in the energy range between 0.7 and 1.7 keV, because the black body emission from the accretion disk in the energy range of 0.5–3 keV can increase during the state change from the low/hard to high/soft state. Thus, the cause of the short-term variation must not be eclipse.

The four short-term softening on S1, S2, S3 and S4 had the characteristic of a increase of

[3] http://www.swift.ac.uk/user_objects/

soft X-rays (2–4 keV) and a decrease of the hard X-rays (15–50 keV) in figure 5.3. The time scale of each softening was less than 40 days as shown in figure 5.5. The hardness during S4 shows that the spectrum is softer than that of the other times. The times of the observations by the *Swift* XRT are shown in figures 5.3 and 5.5.

To know the trend of the state change of Swift J1753.5–0127, we plotted a hardness intensity diagram (HID) using the light curves observed by the SSC, GSC and BAT. Figure 5.6 is the HID of Swift J1753.5–0127 showing the relation between the intensity in the 2–4 keV band and the hardness ratio of 15–50 keV to 2–4 keV. When the intensity in the 2–4 keV energy band increased, the X-ray spectra became softer. The data points for S1, S2, S3 and S4 all lie in the region where the hardness ratio is lower and the 2–4 keV intensity is higher. The HID between the hardness ratio (6–10 keV / 3–6 keV) and the intensity (2–15 keV) based on the PCA onboard *RXTE* during and after the outburst of 2005 (MJD 53500–55500) has been plotted by Soleri et al., 2013. Their HID shows the failed transition into the high/soft state during the outburst as shown in figure 3.4. The data points for the failed transition are softer than those of S1, S2, S3, and S4 in figure 5.6.

5.3 Spectral Analysis

5.3.1 Spectra observed by the *Swift* XRT in S4

We performed spectral analysis in S4, because the source was more frequently observed in S4 with the XRT than in the other periods. The spectral fits were performed with XSPEC version 12.7.1. We fitted the MCD model (§ 2.5.2) and its partially-Comptonized model (§ 2.6.2) with an interstellar absorption to all the XRT spectra.

Applying the tbabs *(diskbb + powerlaw) model

First, we adopted the standard model, the **diskbb** model (Mitsuda et al., 1984), for the thermal disk emission and the **powerlaw** model for the Comptonized emission. The use of the **diskbb** and **powerlaw** model is the most basic way to fit the X-ray spectrum of the black hole binaries. The **diskbb** model can reproduce the spectrum from an accretion disk consisting of multiple blackbody components. The **powerlaw** model is a simple photon power law. It was difficult to constrain the photon index (Γ) of the **powerlaw** model without any information above $\sim$10 keV. Therefore, we constrained Γ to lie within 1.8–3.0, which is reasonable for the hard tail of BHBs in the high/soft state (Remillard & McClintock, 2006). The spectral fittings were performed from 0.6 to 9.4 keV, the response file (swxwt0to2s6_20110101v015.rmf) was designated, and the arf files were generated in the web tools. A systematic error of 3% was taken into account, given the uncertainties of the response matrix [3].

We adopted the **tbabs** model and **wilm** abundance table for the interstellar absorption. The **tbabs** model is one of interstellar medium (ISM) absorption models. This model calculates the cross section for X-ray absorption by the ISM as the sum of the cross sections for X-ray absorption due to the gas-phase ISM, the grain-phase ISM, and the molecules in the ISM. We need to use the **wilm** abundance table to use the **tbabs** model. To estimate $N_{\rm H}$ we summed four XRT spectra on MJD 56037, 56039, 56041, and 56043, in which significant MCD components and absorption were present, and fitted a model to the summed spectrum.

[3] http://www.swift.ac.uk/analysis/xrt/spectra.php

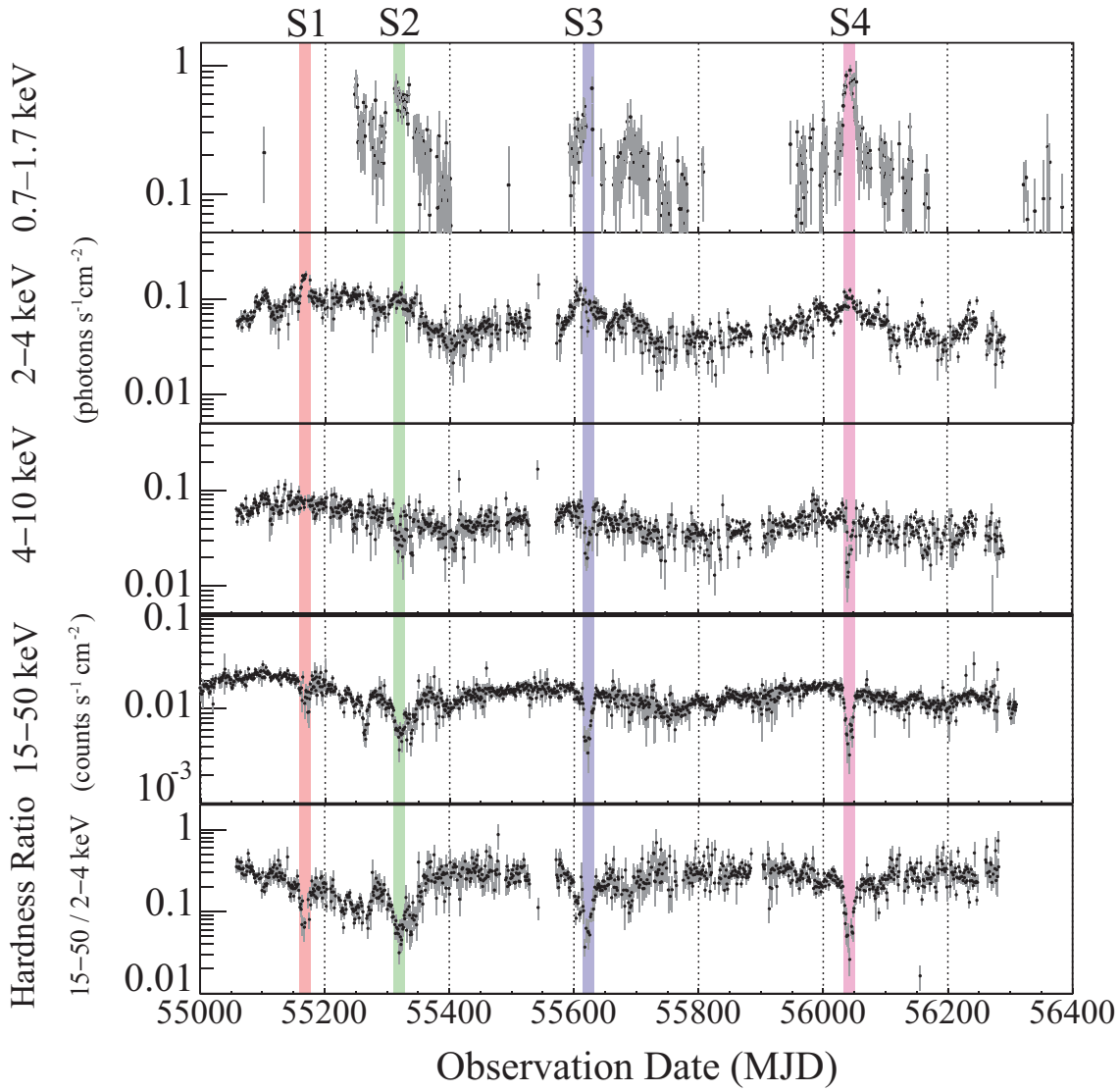

Figure 5.3: (Top) The light curves in the energy band of 0.7–1.7 keV, (second) 2–4 keV, and (third) 4–10 keV, and (fourth) 15–50 keV and (bottom) the hardness ratio of 15–50 keV to 2–4 keV from MJD 55000 to 56400. The light curves in the energy bands of 0.7–1.7 keV, 2–10 keV, and 15–50 keV were observed by the SSC, GSC and BAT, respectively. Hatched regions in red, green, blue and magenta are S1, S2, S3 and S4, respectively.

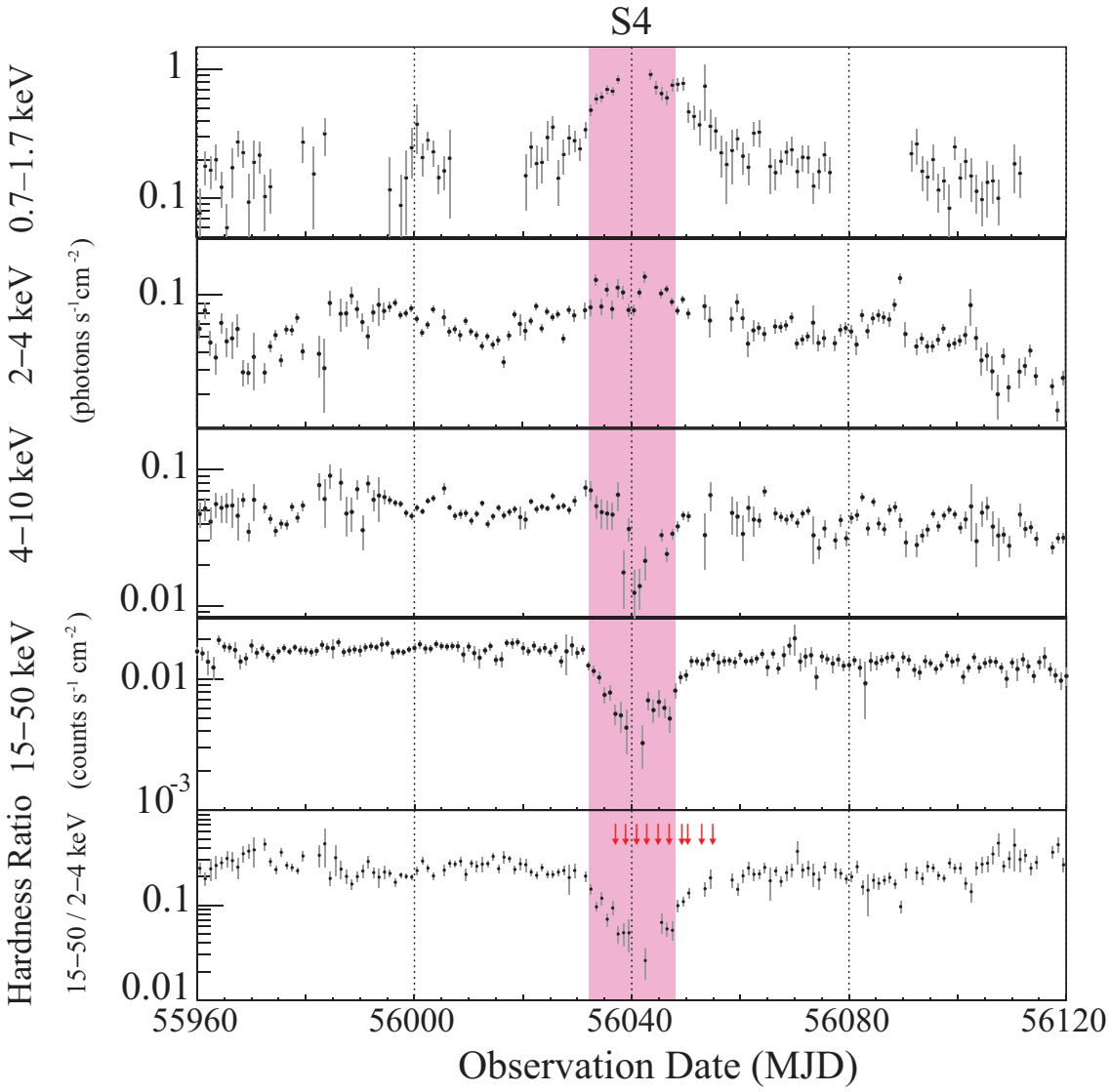

Figure 5.4: (Top) The light curves in the energy band of 0.7–1.7 keV, (second) 2–4 keV, and (third) 4–10 keV, and (fourth) 15–50 keV and (bottom) the hardness ratio of 15–50 keV to 2–4 keV during S4.

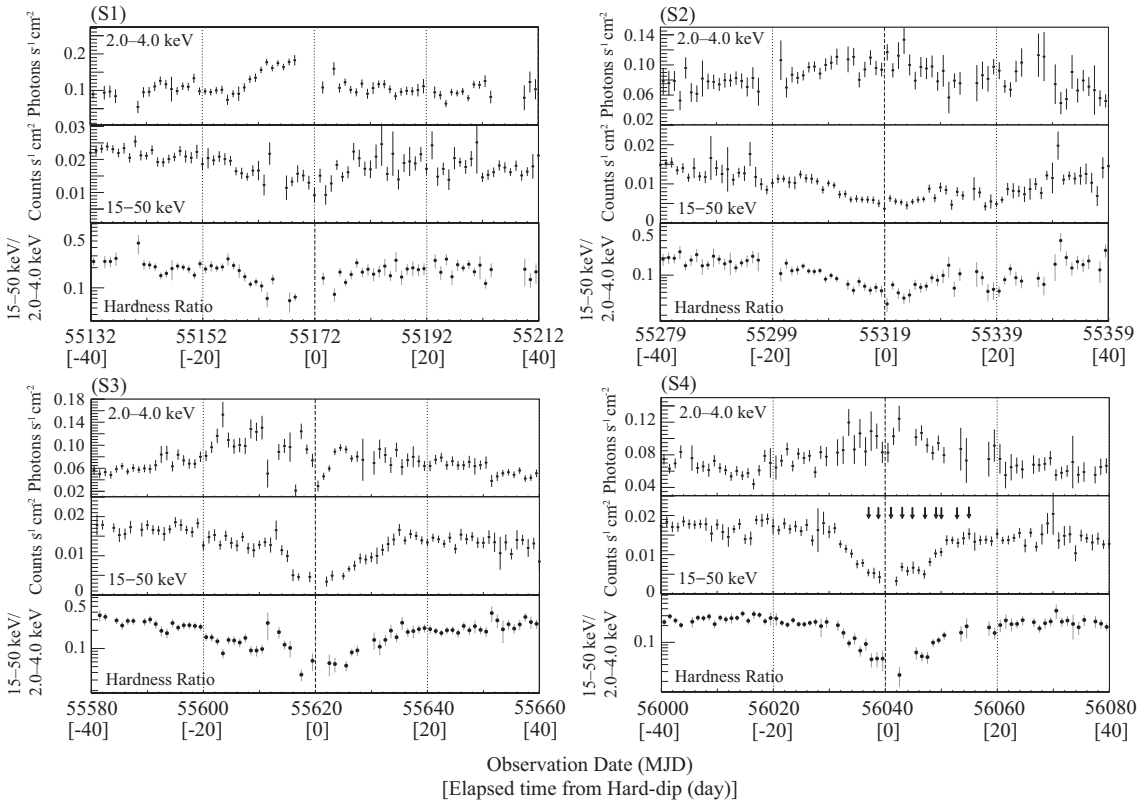

Figure 5.5: (Top) light curves in the energy bands of 2–4 keV, and (middle) 15–50 keV, and (bottom) the hardness ratio of 15–50 keV to 2–4 keV. The light curves and hardness ratio during S1 (top left), S2 (top right), S3 (bottom left) and S4 (bottom right). Origins correspond to the local minimum of the light curves in the energy range of 15–50 keV observed by the BAT. Arrows show the XRT observations in S4.

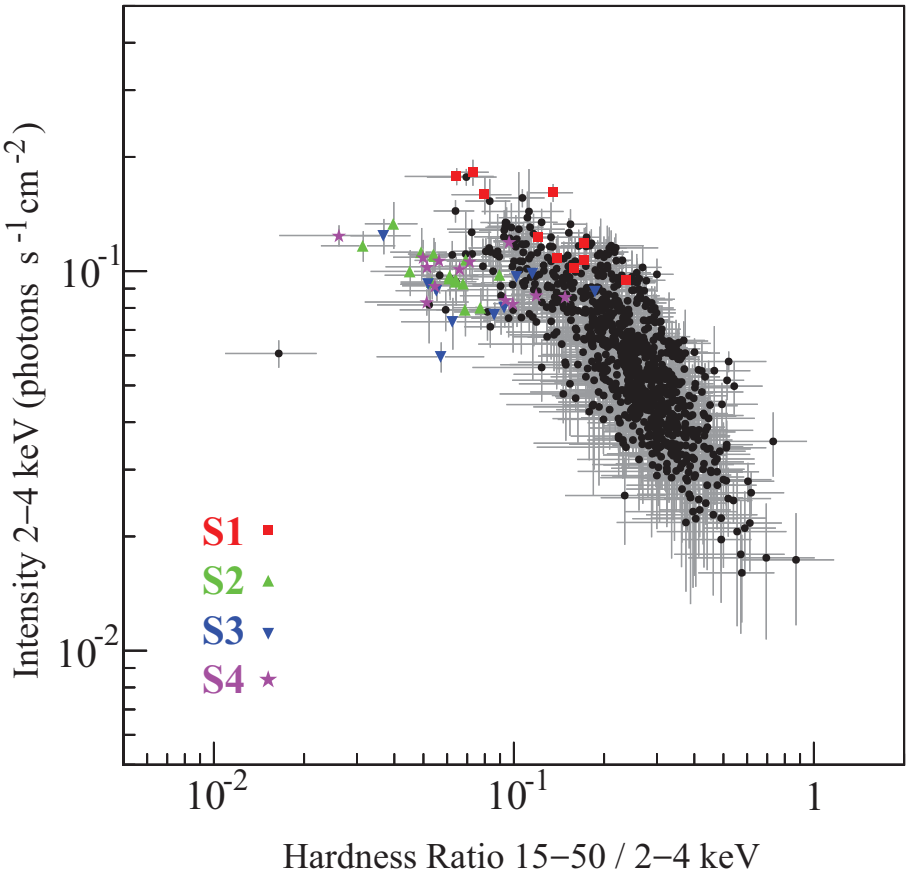

Figure 5.6: The X-ray hardness intensity diagram of Swift J1753.5–0127 since the launch of *MAXI*. Data are plotted in black and that in S1, S2, S3, and S4 are shown in red, green, blue, and magenta, respectively.

The model is written as a **tbabs *(diskbb + powerlaw)** in the XSPEC terminology. The estimated value of $N_{\rm H}$ was 2.8 $\times$ 10^{21} cm^{-2}, which is close to the value obtained in the previous work (Reis et al., 2009, Cadolle Bel et al., 2007 and Soleri et al., 2013). Fixing $N_{\rm H}$ to 2.8 $\times$ 10^{21} cm^{-2}, we then fitted the **tbabs *(diskbb + powerlaw)** model to all the XRT spectra. The best-fit models and the residuals are shown in figure 5.7. The best-fit parameters are listed in table 5.2. As can be seen from table 5.2 and figure 5.8, the model reproduced the data well. A powerlaw with a photon index of 2.1–3.0 and dominant soft component characterized the high/soft state of BHBs. The disk temperature gradually decreased during our XRT observations.

Applying the tbabs * simpl * diskbb model

In order to discuss the MCD flux precisely, we replace the **powerlaw** model with the **simpl** model (Steiner et al., 2009a) because the **simpl** model is more principle than the **powerlaw** model for the Comptonization. The **simpl** model is a phenomenological convolution model that converts a given fraction of the incident spectrum into a powerlaw for the Comptonized emission. This model is written as a **tbabs*simpl*diskbb** in the XSPEC terminology. We also obtained acceptable fits with this model for all the spectra with a systematic error of 3%. The best-fit parameters are listed in table 5.3. To fit the **tbabs*simpl*diskbb** model to the spectra, the value of $N_{\rm H}$ was estimated to be 2.0 $\times$ 10^{21} cm^{-2} in a similar way to the fitting the **tbabs *(diskbb + powerlaw)** model. The value is also similar to the value obtained in the previous work (Reynolds et al., 2010). Since **simpl** redistributes input photons to higher and lower energies, the energy range of the response matrix must be extended from 0.1 to 1000 keV. Figure 5.9 shows the fitting results. The best-fit **tbabs*simpl*diskbb** models are superposed and the residuals are shown in the lower panel of each figure. We will mainly discuss the best-fit parameters of the **tbabs*simpl*diskbb** model, because the **simpl** model can take into account the Comptonized photons more properly than the **powerlaw** model (Steiner et al., 2009b).

Figure 5.10 shows the time evolution of the fitting results in S4. The best-fit parameters appeared to reach a plateau between MJD 56037 and 56043. The best fit value of $T_{\rm in}$ gradually decreased from $\sim$0.4 keV to $\sim$0.2 keV from MJD 56047 to MJD 56055. The lowest value of $T_{\rm in}$ is close to that obtained by the Suzaku observation of the low/hard state in 2007 (Reynolds et al., 2010). However, a powerlaw with a photon index of 2.06 on MJD 56055 still characterized the high/soft state. These results suggest that the source is in the intermediate state. The values of $T_{\rm in}$ and the disk flux in the 0.01–10 keV energy range ($F_{\rm disk}$) changed from 0.48 to 0.22 keV and from 4.5 $\times 10^{-9}$ to 2.2 $\times 10^{-9}$ erg s^{-1} cm^{-2}, respectively. $F_{\rm disk}$ declined and $f_{\rm sc}$ increased from MJD 56045 to 56055, which indicates a state transition from the soft to hard state, as shown in figure 5.10.

To examine an existence of Fe Kα emission due to disk reflection, we added a broad gaussian to the model for the data based on MJD 56041, but the fits were not significantly improved, which was consistent with there being little enhancement in the raw spectra and few observations around 6 keV. Thus, we could not confirm the existence of the broad iron lines, which would be presumably due to the fitting methods: fitting the spectra ignoring the 4–7 keV band, for instance (Reis et al., 2009).

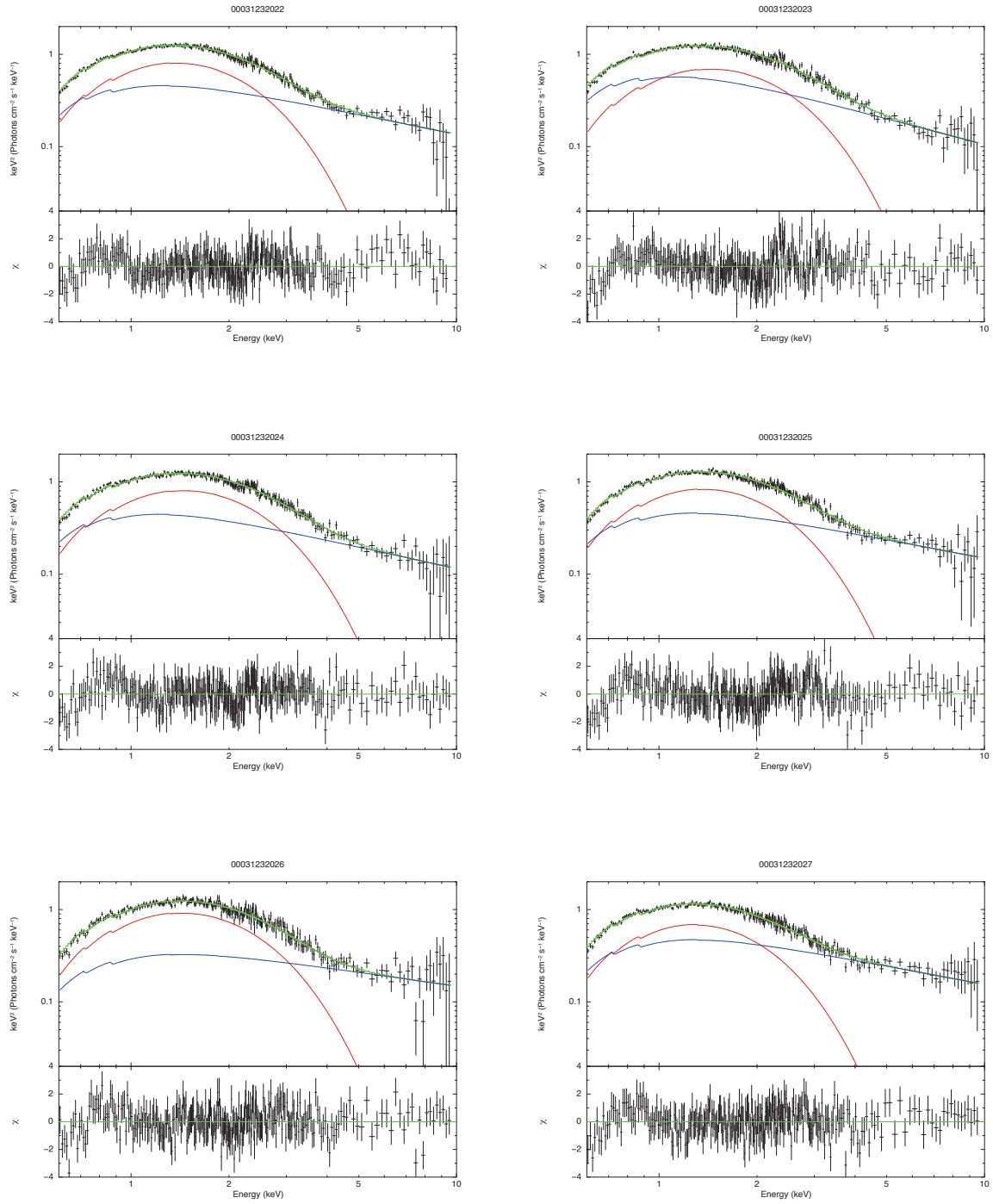

Figure 5.7: The spectra fitted to the **tbabs *(diskbb + powerlaw)** model. The black points, the red line and blue line show the X-ray spectral data, the **diskbb** and **powerlaw** component.

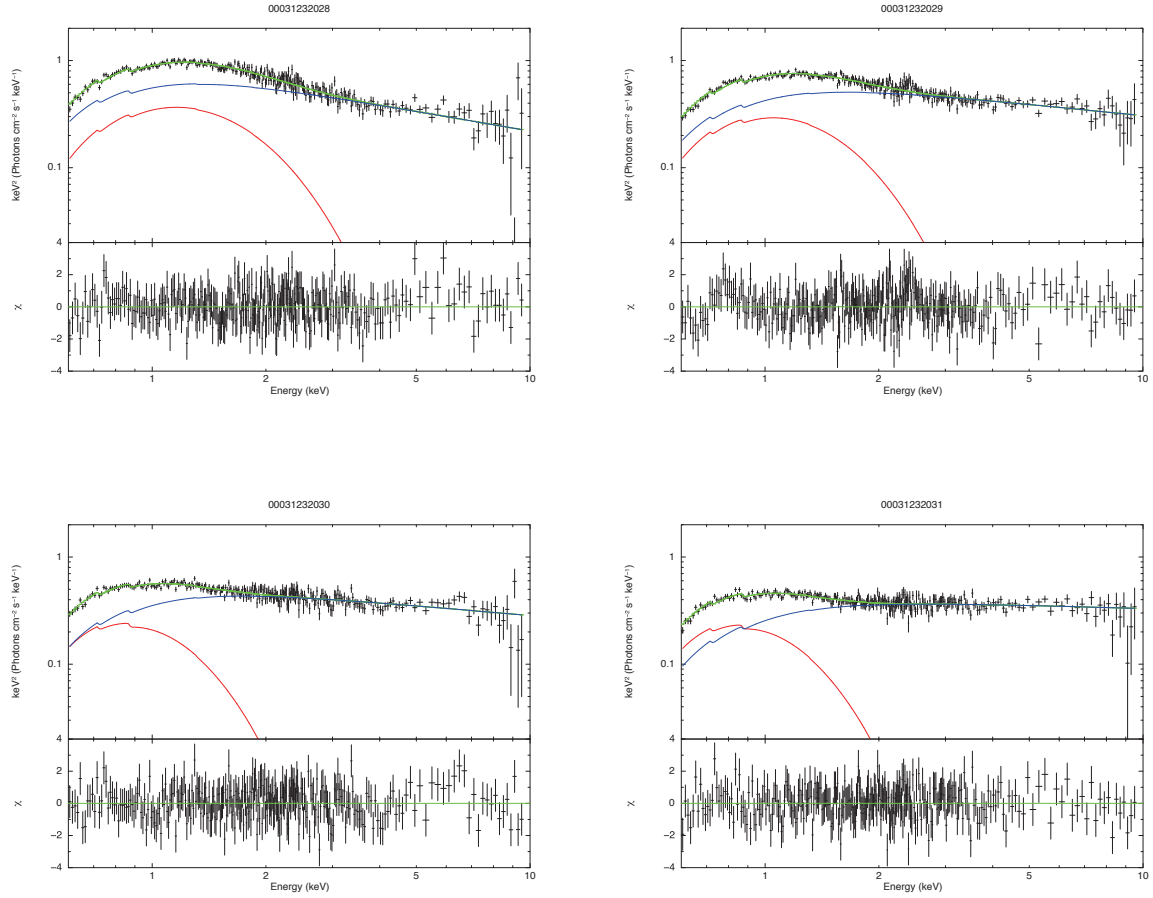

Figure 5.7: *Continued*

Table 5.2: The best-fit parameters of the **tbabs*(diskbb+powerlaw)** model of the Swift J1753.5–0127 spectra. The value of $N_{\rm H}$ was fixed to 2.8×10^{21} cm^{-2}.

MJD	$T_{\rm in}$ (keV)	$N_{\rm disk}$ [1] (10^3)	$F_{\rm disk}$ [2]	Observed flux [3]	Photon Index	Powerlaw Norm	χ^2/DOF
56037[4]	0.451 ± 0.006	$3.8^{+0.4}_{-0.3}$	3.41 ± 0.13	$2.902^{+0.010}_{-0.018}$	2.71 ± 0.04	0.70 ± 0.04	234/273
56039[4]	$0.484^{+0.010}_{-0.009}$	$2.4^{+0.3}_{-0.2}$	2.82 ± 0.11	$2.884^{+0.008}_{-0.15}$	2.93 ± 0.03	0.90 ± 0.03	297/273
56041[4]	0.487 ± 0.009	$2.7^{+0.3}_{-0.2}$	$3.27^{+0.12}_{-0.13}$	$2.862^{+0.008}_{-0.03}$	$2.78^{+0.04}_{-0.05}$	0.69 ± 0.04	216/273
56043[4]	$0.448^{+0.008}_{-0.007}$	4.1 ± 0.4	$3.54^{+0.15}_{-0.16}$	$2.983^{+0.011}_{-0.02}$	2.67 ± 0.05	0.70 ± 0.05	266/273
56045[4]	$0.478^{+0.010}_{-0.009}$	3.4 ± 0.4	$3.77^{+0.18}_{-0.19}$	$2.854^{+0.006}_{-0.04}$	$2.50^{+0.08}_{-0.09}$	0.47 ± 0.06	281/273
56047[4]	0.403 ± 0.008	5.4 ± 0.7	3.10 ± 0.19	$2.708^{+0.010}_{-0.018}$	2.66 ± 0.05	0.71 ± 0.05	242/273
56049[4]	0.338 ± 0.011	6.7 ± 1.5	1.9 ± 0.3	$2.553^{+0.006}_{-0.03}$	2.61 ± 0.05	0.90 ± 0.06	306/273
56050[4]	0.284 ± 0.008	$12.8^{+1.9}_{-1.8}$	$1.8^{+0.19}_{-0.18}$	$2.294^{+0.006}_{-0.03}$	2.35 ± 0.05	0.69 ± 0.05	268/273
56053[4]	0.201 ± 0.009	65^{+16}_{-11}	2.25 ± 0.16	$1.891^{+0.008}_{-0.04}$	2.30 ± 0.04	0.57 ± 0.03	271/273
56055[4]	0.201 ± 0.008	62^{+13}_{-10}	$2.16^{+0.12}_{-0.13}$	$1.694^{+0.005}_{-0.04}$	2.10 ± 0.04	0.41 ± 0.02	250/273

[1] Normalization of the **diskbb** model

[2] Flux of disk in the 0.01–10 keV energy range in the unit of 10^{-9}erg s^{-1} cm^{-2}

[3] Flux obtained from observed spectra in the 0.6–10 keV energy range in the unit of 10^{-9}erg s^{-1} cm^{-2}

[4] Observation date of the *Swift* XRT

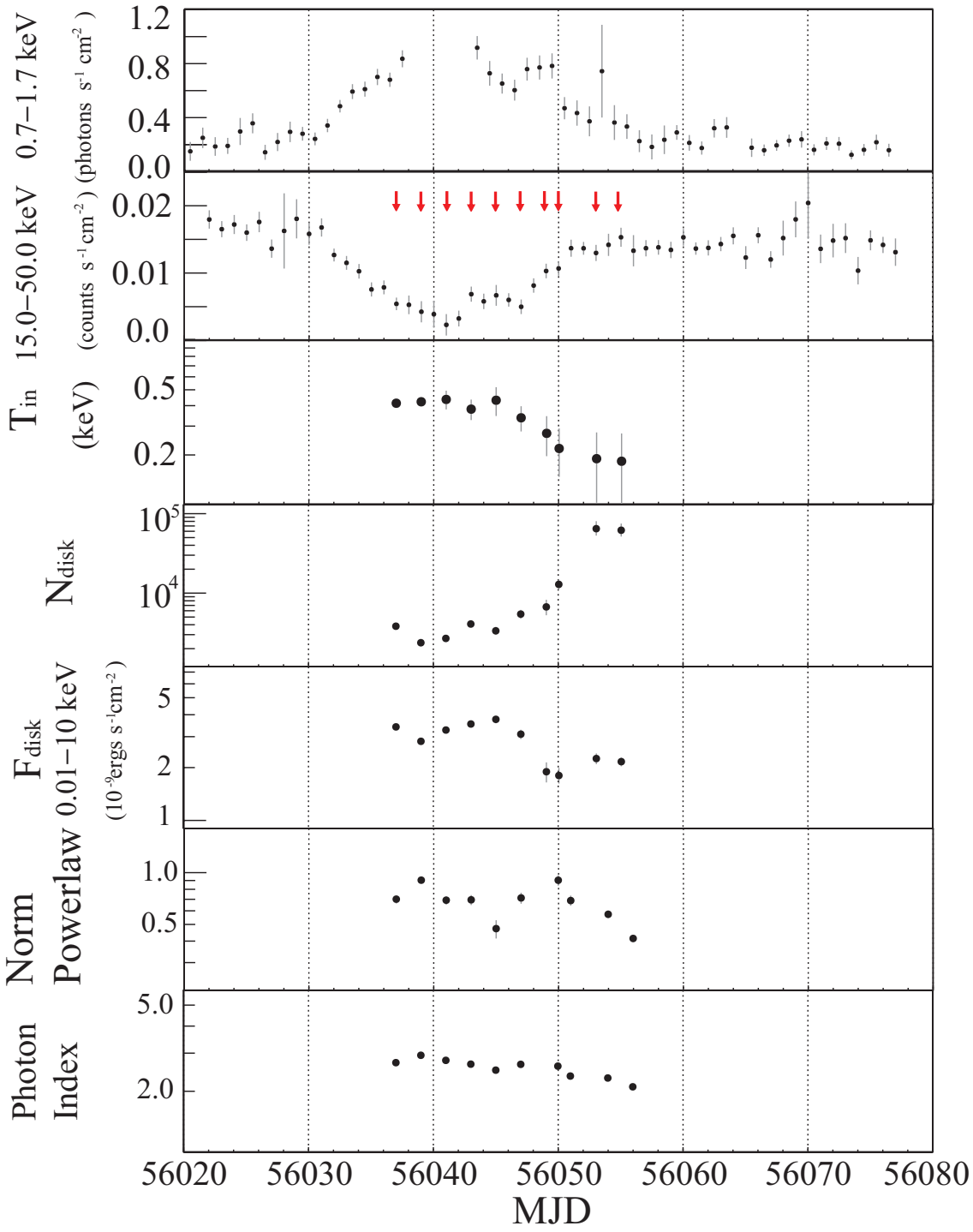

Figure 5.8: Time evolution of the best-fit parameters of the **tbabs*(diskbb+powerlaw)** model and X-ray intensity. From top to bottom, the intensity in 0.7–1.7 keV observed by the SSC, that in 15–50 keV observed by the BAT, $T_{\rm in}$, $N_{\rm disk}$, $F_{\rm disk}$, normalization of **powerlaw**, and photon index. Some error bars are hard to see, because they are smaller than the plotting symbols. Red arrows show the ten *Swift* XRT observations.

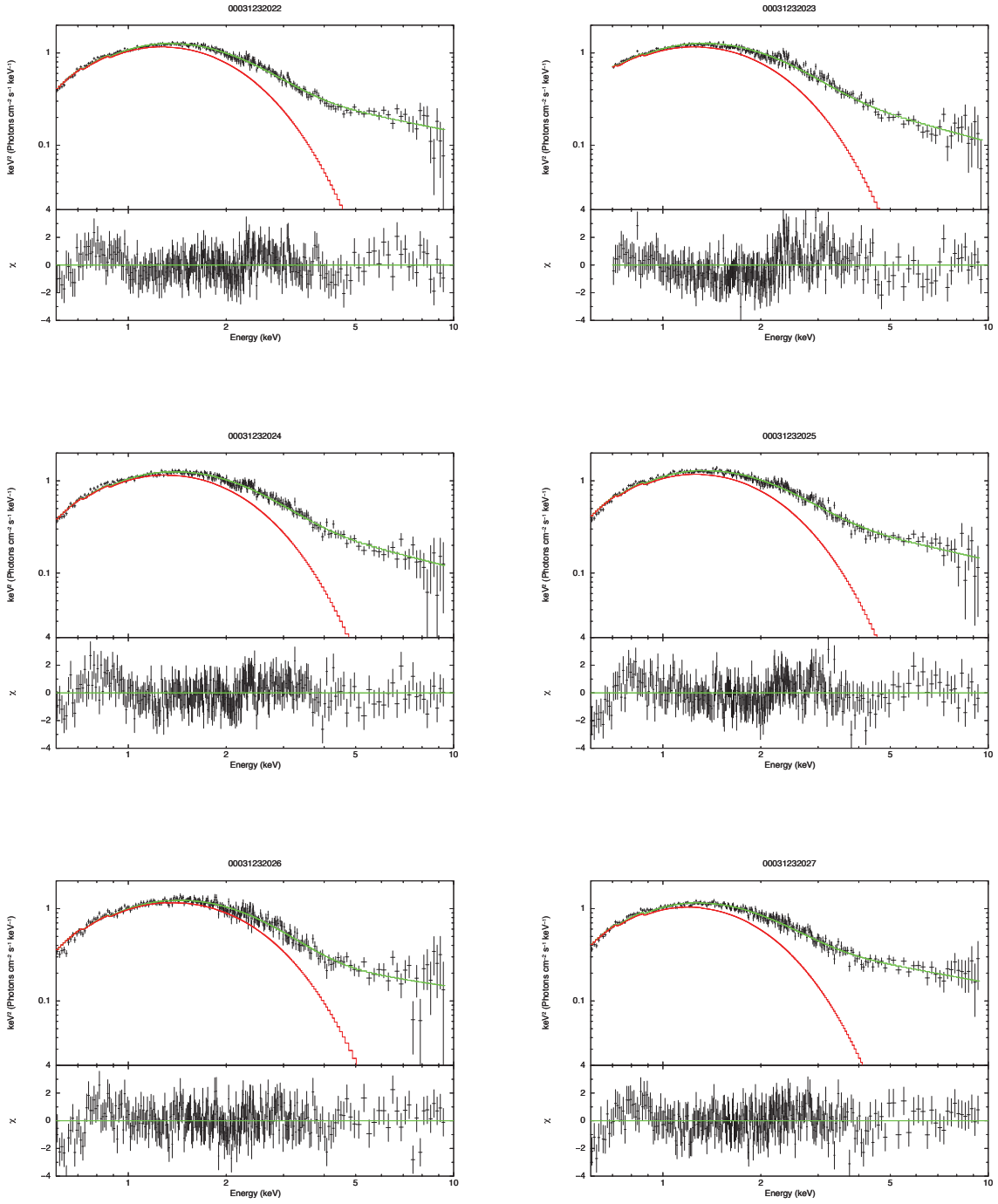

Figure 5.9: The spectrum of XRT shown in black. The best-fit **tbabs*simpl*diskbb** model and the **diskbb** component are shown as green and red lines, respectively. Residuals between the data and best-fit model are shown in the lower panel.

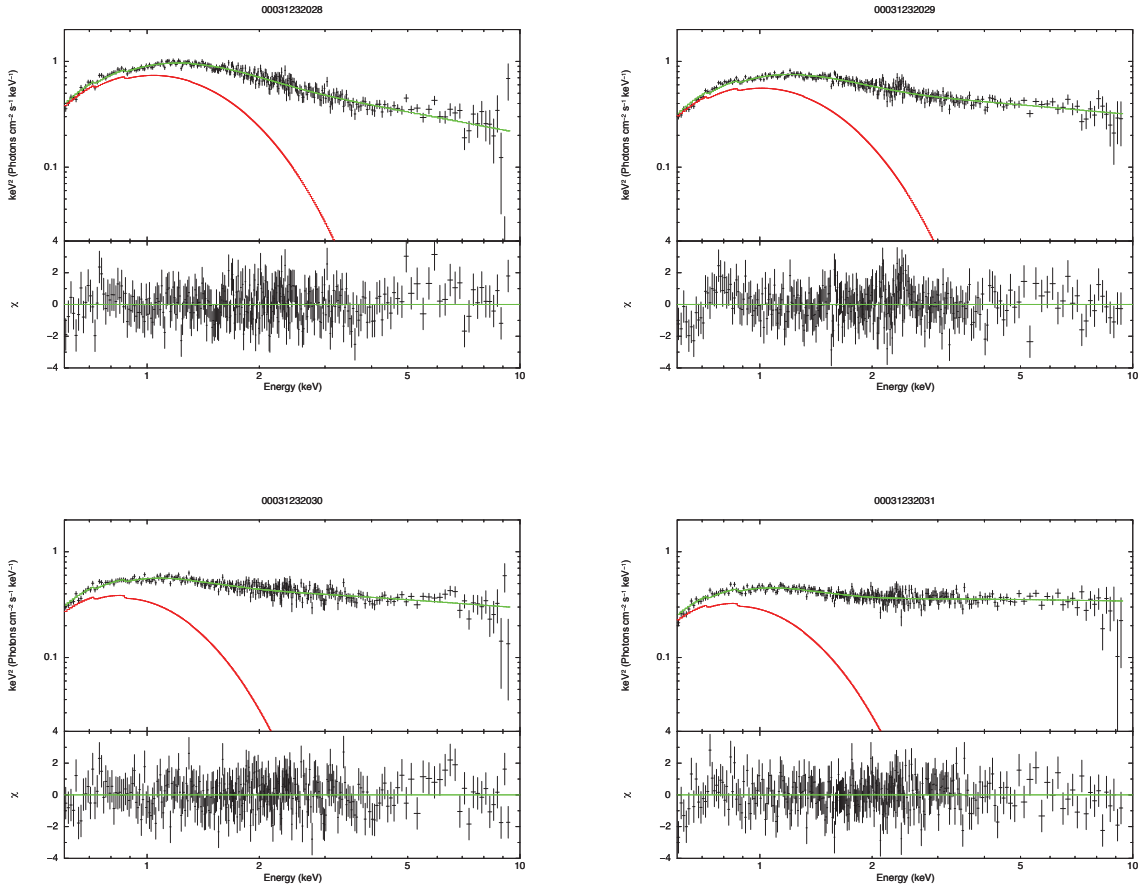

Figure 5.9: *Continued*

Table 5.3: The best-fit parameters of the **tbabs*simpl*diskbb** model of the Swift J1753.5–0127 spectra. The value of $N_{\rm H}$ was fixed to 2.0×10^{21} cm^{-2}.

MJD	$T_{\rm in}$ (keV)	$N_{\rm disk}$ [1] (10^3)	$F_{\rm disk}$ [2]	Observed flux [3]	Photon Index	$f_{\rm SC}$ [4]	χ^2/DOF
56037 [5]	0.429 ± 0.008	$6.50^{+0.5}_{-0.4}$	4.73 ± 0.04	$2.902^{+0.010}_{-0.018}$	2.72 ± 0.17	0.16 ± 0.03	271/273
56039 [5] [6]	0.435 ± 0.007	$5.9^{+0.5}_{-0.4}$	4.54 ± 0.04	$2.884^{+0.008}_{-0.15}$	$3^{0}_{-0.08}$	$0.2^{+0.009}_{-0.013}$	278/234
56041 [5]	0.443 ± 0.006	$5.5^{+0.3}_{-0.2}$	4.57 ± 0.04	$2.862^{+0.008}_{-0.03}$	$3.0^{0}_{-0.08}$	$0.193^{+0.010}_{-0.017}$	233/273
56043 [5]	$0.425^{+0.009}_{-0.010}$	$6.8^{+0.6}_{-0.5}$	4.80 ± 0.05	$2.983^{+0.011}_{-0.02}$	2.81 ± 0.19	$0.18^{+0.04}_{-0.03}$	276/273
56045 [5]	$0.478^{+0.012}_{-0.013}$	$4.0^{+0.4}_{-0.3}$	4.50 ± 0.05	$2.854^{+0.006}_{-0.04}$	2.5 ± 0.3	$0.12^{+0.05}_{-0.04}$	293/273
56047 [5]	$0.389^{+0.009}_{-0.010}$	$9.0^{+0.9}_{-0.7}$	4.44 ± 0.05	$2.708^{+0.010}_{-0.018}$	2.65 ± 0.16	$0.183^{+0.04}_{-0.03}$	249/273
56049 [5]	$0.308^{+0.012}_{-0.013}$	19 ± 3	3.71 ± 0.06	$2.553^{+0.006}_{-0.03}$	2.67 ± 0.09	$0.35^{+0.05}_{-0.04}$	309/273
56050 [5]	$0.293^{+0.010}_{-0.011}$	18^{+3}_{-2}	2.93 ± 0.05	$2.294^{+0.006}_{-0.03}$	$2.32^{+0.06}_{-0.07}$	0.33 ± 0.03	275/273
56053 [5]	$0.219^{+0.010}_{-0.011}$	53^{+13}_{-9}	2.63 ± 0.06	$1.891^{+0.008}_{-0.04}$	2.26 ± 0.05	$0.33^{+0.03}_{-0.02}$	272/273
56055 [5]	0.221 ± 0.009	43^{+9}_{-7}	2.19 ± 0.05	$1.694^{+0.005}_{-0.04}$	2.06 ± 0.05	$0.293^{+0.019}_{-0.018}$	260/273

[1] Normalization of the **diskbb** model
[2] Flux of disk in the 0.01–10 keV energy range in the unit of 10^{-9}er s^{-1} cm^{-2}
[3] Flux obtained from observed spectra in the 0.6–10 keV energy range in the unit of 10^{-9}erg s^{-1} cm^{-2}
[4] Scattered fraction
[5] Observation date of the *Swift* XRT
[6] The fitting range from 1.0 keV to 9.4 keV due to the uncertainty of the response below 1.0 keV

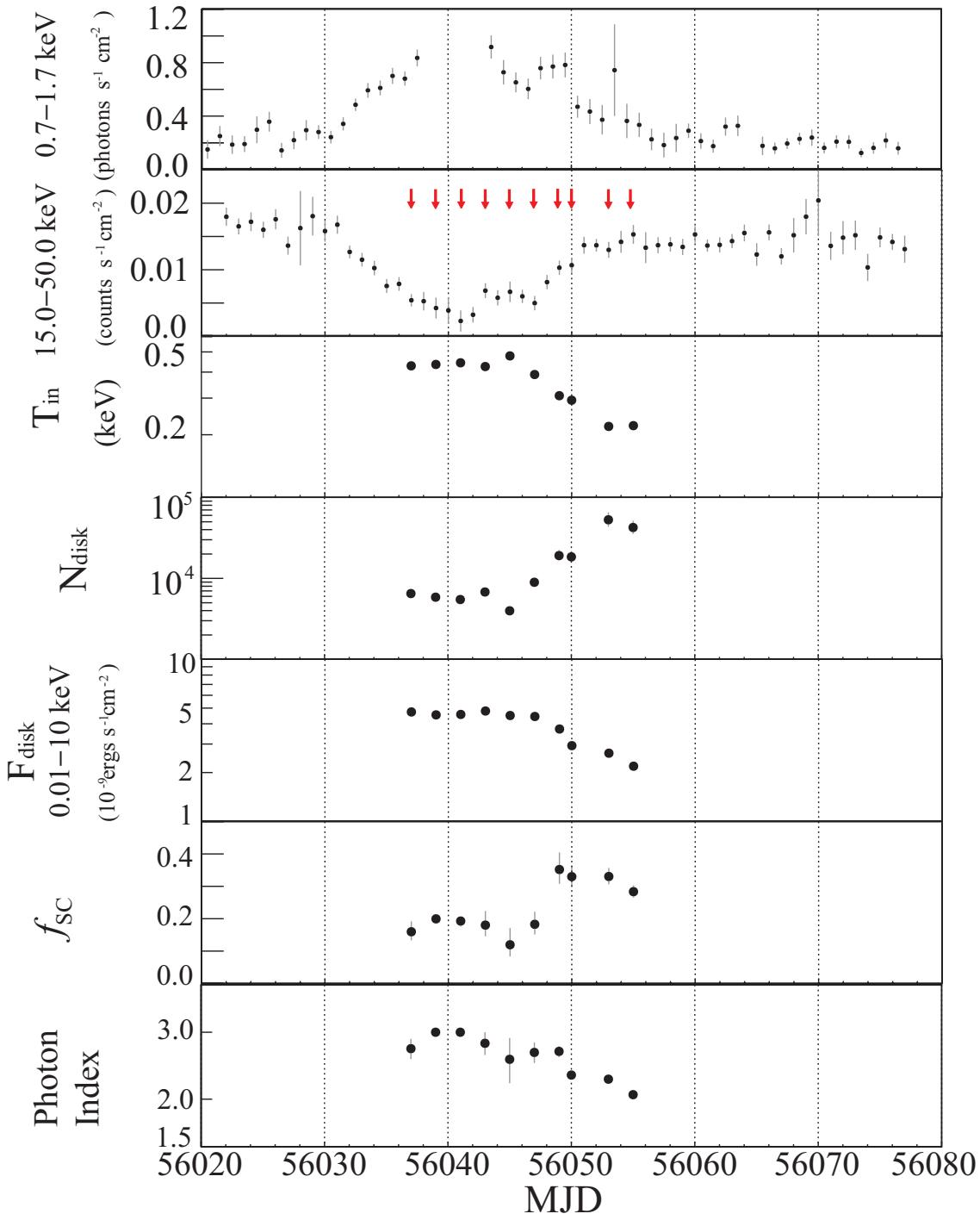

Figure 5.10: Time evolution of the best-fit parameters of the **tbabs*simpl*diskbb** model and X-ray intensity. From top to bottom, the intensity in 0.7–1.7 keV observed by the SSC, that in 15–50 keV observed by the BAT, $T_{\rm in}$, $N_{\rm disk}$, $F_{\rm disk}$, the scattered fraction ($f_{\rm sc}$), and photon index. The parameter $f_{\rm sc}$ indicates the rate of conversion of photons from black body emission into Comptonized photons. Some error bars are hard to see, because they are smaller than the plotting symbols. Red arrows show ten XRT observations.

Table 5.4: The data of the X-ray spectrum observed by *MAXI* during S2, S3 and S4.

		SSC		GSC	
Name	MJD	Duration [1]	Count Rate [2]	Duration [3]	Count Rate [2]
S2	55311-55327	7.1	0.415±0.009 (82.5%)	32.5	0.096±0.003 (47.4%)
S3	55612-55628	2.1	0.337±0.014 (82.9%)	46.1	0.089±0.003 (45.5%)
S4	56032-56048	5.4	0.37±0.1 (80.2%)	25.3	0.099±0.003 (51.2%)

[1] Total exposure time for the SSC (ks)
[2] Background-subtracted source count rate (cnt/s). The parenthetic numbers show the fraction of the source count rates to the total one.
[3] Total exposure time for the GSC (ks)

5.3.2 Spectra observed by *MAXI* in S2, S3 and S4

To investigate the repetitive nature of the short-term softening, we extracted the X-ray spectrum observed by *MAXI* during S2 and S3. Since the SSC data was lacking during S1, we did note extracted the X-ray Spectra during S1. The X-ray spectra in the short-term softening are summarized in table 5.4. Figure 5.11 shows the X-ray spectra during S2, S3 and S4.

To obtain the best-fit parameters in S2 and S3 that were not observed by the XRT, we analyzed the spectra observed by the SSC and GSC during S2 and S3 in the same way as for S4. First, to check if $T_{\rm in}$ and $F_{\rm disk}$ obtained from the SSC and GSC spectra are consistent with those from the XRT spectra, we fitted the **tbabs*(diskbb+powerlaw)** and **tbabs*simpl*diskbb** models to the spectra observed by the SSC and GSC in S4. Figure 5.12 shows the time average spectrum for 16 days. The best-fit parameters of the **tbabs*(diskbb+powerlaw)** and **tbabs*simpl*diskbb** models are listed in table 5.5. The difference between the observational results of the SSC and GSC and those of the XRT in S4 was within the error. The values of $T_{\rm in}$ and $F_{\rm disk}$ in S2 and S3, which are almost the same as those in S4 within error bars, are included in tables 5.2 and 5.3. These results show that the $T_{\rm in}$ and $F_{\rm disk}$ reach to $\sim$0.4 keV and $\sim 4\times10^{-9}$ erg s^{-1} cm^{-2} in S2 and S3 and the state changes of S2 and S3 are similar that of S4. There is the repetitive nature of the short-term softening due to the state change.

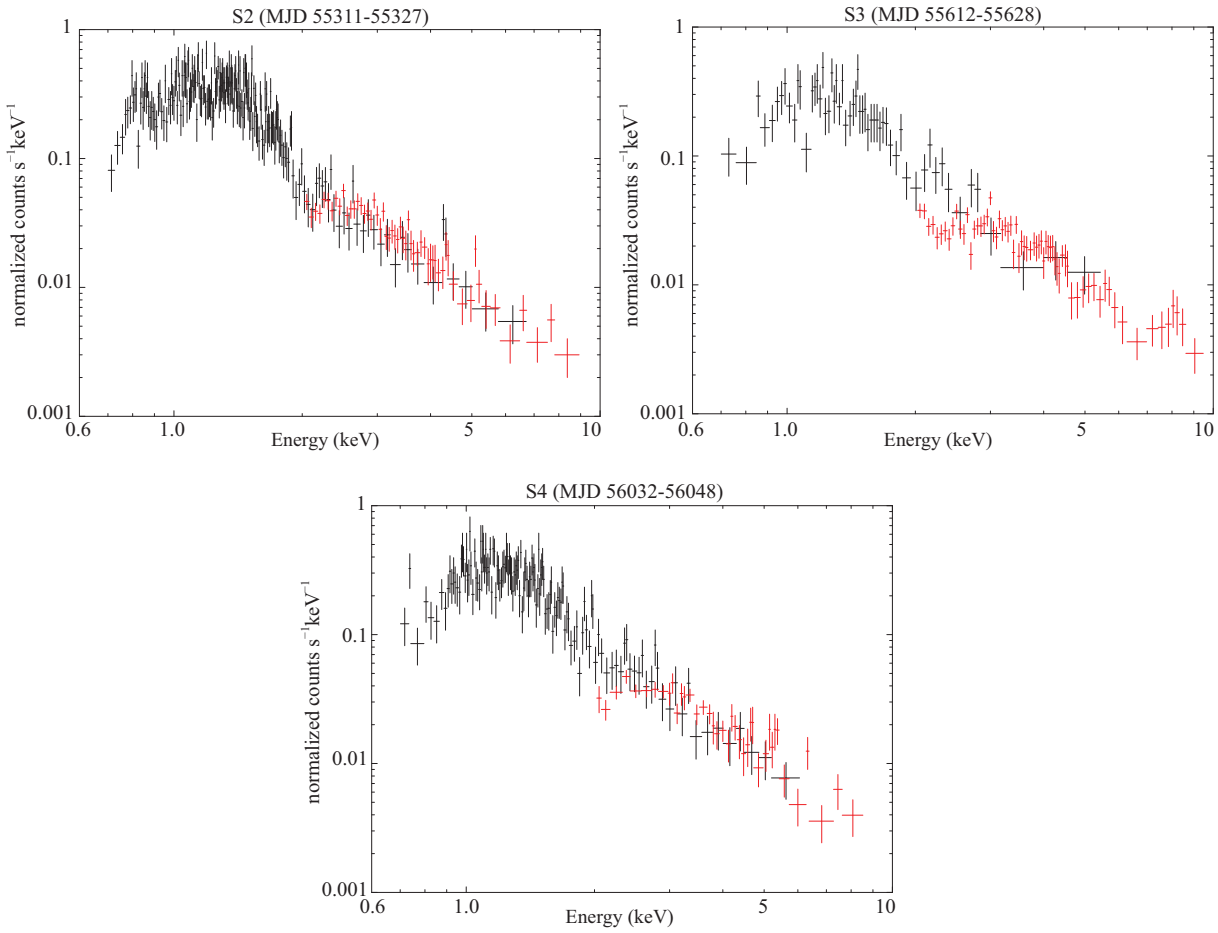

Figure 5.11: (Top-left) The count spectra observed by *MAXI* during S2. (Top-right) The spectra of S3. (Bottom) The spectra of S4. The data obtained by the SSC and GSC are plotted in black and red lines, respectively.

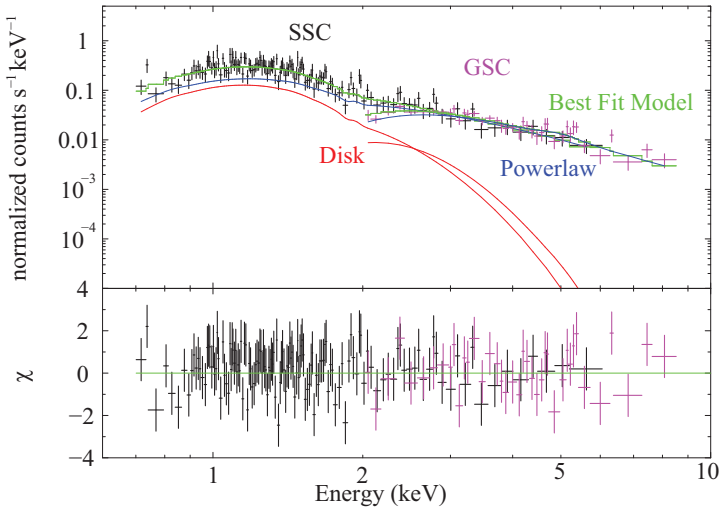

Figure 5.12: The spectrum observed by the SSC (black) and GSC (magenta) in S4. The best-fit model of **tbabs*(diskbb+powerlaw)**, the **tbabs*diskbb** component, and the **powerlaw** component are shown as green, red, and blue lines. Residuals between the data and best-fit model are shown in the lower panel.

Table 5.5: The best-fit parameters of the **tbabs*(diskbb+powerlaw)** and **tbabs*simpl*diskbb** models of the Swift J1753.5–0127 spectra.

tbabs*(diskbb+powerlaw)							
MJD	$T_{\rm in}$ (keV)	$N_{\rm disk}$ [1] (10^3)	$F_{\rm disk}$ [2]	Observed flux [3]	Photon Index	Powerlaw Norm	χ^2/DOF
S2 [4]	0.369 ± 0.017	13 ± 3	$5.10^{+0.8}_{-0.6}$	$2.95^{+0.02}_{-0.04}$	$2.3^{+0.3}_{-0.4}$	$0.43^{+0.26}_{-0.18}$	259/249
S3 [4]	$0.449^{+0.016}_{-0.03}$	$4.58^{+1.5}_{-0.7}$	$4.0^{+0.5}_{-0.3}$	$2.52^{+0.03}_{-0.18}$	$1.8^{+0.4}_{-0.5}$	$0.171^{+0.16}_{-0.014}$	135/120
S4 [4]	0.39 ± 0.04	5 ± 3	$2.5^{+1.0}_{-0.9}$	$2.59^{+0.12}_{-0.19}$	2.6 ± 0.3	0.8 ± 0.3	173/176
tbabs*simpl*diskbb)							
MJD	$T_{\rm in}$ (keV)	$N_{\rm disk}$ [1] (10^3)	$F_{\rm disk}$ [2]	Observed flux [3]	Photon Index	$f_{\rm SC}$ [5]	χ^2/DOF
S2 [4]	0.38 ± 0.03	12^{+4}_{-3}	5.3 ± 0.3	$2.95^{+0.02}_{-0.04}$	2.3 ± 0.5	$0.10^{+0.07}_{-0.04}$	262/249
S3 [4]	$0.45^{+0.02}_{-0.03}$	$4.6^{+1.6}_{-0.8}$	$4.2^{+0.3}_{-0.2}$	$2.52^{+0.03}_{-0.18}$	$1.8^{+0.4}_{-0.7}$	$0.074^{+0.04}_{-0.009}$	136/120
S4 [4]	$0.35^{+0.05}_{-0.06}$	12^{+12}_{-5}	3.9 ± 0.3	$2.59^{+0.12}_{-0.19}$	2.7 ± 0.4	$0.30^{+0.05}_{-0.06}$	173/176

[1] Normalization of the **diskbb** model
[2] Flux of disk in the 0.01–10 keV energy range in the unit of 10^{-9}erg s^{-1} cm^{-2}
[3] Flux obtained from observed spectra in the 0.6–10 keV energy range in the unit of 10^{-9}erg s^{-1} cm^{-2}
[4] Observation period of the SSC and GSC
[5] Scattered fraction

Chapter 6

DISCUSSION

6.1 Summary of results

The decrease of the light curve in the energy range between 15-50 keV of Swift J1753.5–0127 have been observed for a lasting 20 days. The short-term variation was analyzed with the *MAXI* and *Swift* data. We obtained following results from the data analysis.

1. The short-term spectral softening is characterized by an intensity dip of hard X-rays (15–50 keV) and an intensity hump of soft X-rays (0.7–4 keV) for a few tens of days in the low/hard state.

2. The spectral analysis shows that the X-ray spectra can be explained by the black body radiation from the accretion disk. The parameters of the accretion disk during the short-term spectral softening changes.

3. The short-term softenings were repeated forth times between Jun. 2009 and Oct. 2012.

6.2 Comparison with the state change of GX339-4

The state change is depending on the mass accretion rates which is defined by the binary systems (§ 2.3 and 2.6). The systems of GX339-4 is LMXBs and the mass accretion is provided by "Roche lobe overflow". The systems of Swift J1753.5–0127 is also LMXBs. GX339-4 is well known to be repeatable transients and its state changes are typical (Markert et al., 1973).

Figure 6.1 shows the light curve of GX339-4 during the state change. The light curves in the energy range of 2-4 keV and 15-50 keV have increased on MJD 55200 (Jan. 4th 2010). The light curves in the energy range of 2-4 keV and 15-50 keV reached to the peak on MJD 55290 (Apr. 4th 2010) and on MJD 55310 (Apr. 24th 2010) , respectively. The variations of the light curves in the energy range of 2-4 keV and 15-50 keV are magnified $\sim$ hundred times. The light curves in the energy range of 2-4 keV rose up to peak within $\sim$100 days. The time scale of the attenuation since the peak is $\sim$300 days and its fall time is $\sim$100 days. The time scale of the rise up and the fall time in the energy 15-50 keV band are $\sim$100 days and $\sim$50 days, respectively. The light curves of Swift J1753.5–0127 are shown in figure 5.4. The total periods of the short-term softening is $\sim$40 days in figure 5.5. The maximum variation of the light curve of Swift J1753.5–0127 is $\sim$10 times. The variations and periods during the state change of Swift J1753.5–0127 are smaller than that of GX339-4.

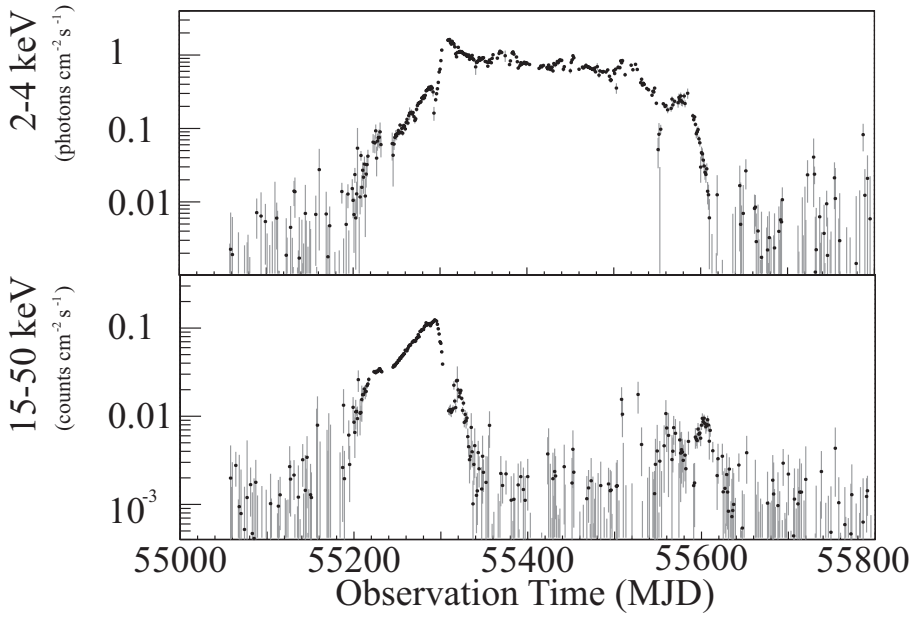

Figure 6.1: The light curve of GX339-4 in the energy range of 2-4 keV and 15-50 keV during the state change. The light curve in the energy range of 2-4 keV and 15-50 keV are observed by the GSC and BAT, respectively.

The X-ray spectroscopies of GX339-4 had been performed in many times since its discovery. The temperature of the accretion disk ($T_{\rm in}$) during the low/hard state is $\sim$0.2 keV(Zdziarski et al., 1998) and $T_{\rm in}$ during the high/soft state reaches $\sim$1.0 keV (Nandi et al., 2012). The energy flux of the accretion disk ($F_{\rm disk}$) in the low/hard and high/soft state are 0.01×10^{-9} erg cm^{-2} s^{-1} and 6.5×10^{-9} erg cm^{-2} s^{-1}, respectively (Nandi et al., 2012). The values of $T_{\rm in}$ and $F_{\rm disk}$ increased to five and hundred times during the state changes. In the case of Swift J1753.5–0127, the value of $F_{\rm disk}$ changed from 0.01×10^{-9} erg cm^{-2} s^{-1} to 0.05×10^{-9} erg cm^{-2} s^{-1}, and the value of $T_{\rm in}$ changes from 0.2 keV to 0.5 keV. The values of $T_{\rm in}$ and $F_{\rm disk}$ increased to two and five times during the state changes. The variation value of $T_{\rm in}$ and $F_{\rm disk}$ of Swift J1753.5–0127 during the short-term softening are much lower than that of GX339-4. The state change of Swift J1753.5–0127 might be much smaller than that of GX339-4.

6.3 State change during the short-term softening

Since the mathematical formula of the disk flux ($F_{\rm disk}$) can be written as $F_{\rm disk} \propto r_{\rm in}^2 T_{\rm in}^4$, the disk flux ($F_{\rm disk}$) is proportional to $T_{\rm in}^4$ when the accretion disk reaches to the ISCO. Figure 6.2 shows the plot of relation between $F_{\rm disk}$ and $T_{\rm in}$ of Swift J1753.5–0127 during the short-term softening. The data were fitted by $F_{\rm disk} \propto {T_{\rm in}}^{0.97\pm0.02}$. The lines corresponding to the powerlaw indexes of 1 and 4 are overlaid on figure 6.2. The accretion disk extending down to the ISCO in the low/hard state has been suggested (Reis et al., 2009). If $R_{\rm in}$ reaches the ISCO, the relation between $F_{\rm disk}$ and $T_{\rm in}^4$ is expected to be $F_{\rm disk} \propto T_{\rm in}^4$. However, the data during the short-term softening seem to follow the curve of $F_{\rm disk} \propto T_{\rm in}$, which suggests a truncated disk. These results imply that the mass accretion rate is insufficient to stabilize the inner edge of the disk at the ISCO, and there is a possibility that $R_{\rm in}$ is larger than the ISCO. The value of $f_{\rm SC}$

increased from 0.12 to 0.30 as $R_{\rm in}$ increased, suggesting that the number of the inverse-Compton scattering increased in the plasma around the accretion disk.

In the case of the state change of XTE J1817-330 which is typical BH source and well observed, the relation between $F_{\rm disk}$ and $T_{\rm in}$ were plotted in Cabanac et al., 2009. The $F_{\rm disk}$ during the high/soft state is proportionate to ${T_{\rm in}}^4$ and that during the low/hard state is proportionate to ${T_{\rm in}}^{(3/4)}$. The plots of the relation indicate the distribution changed when the eddington ratio (L/L_E) is over 1.5% (Cabanac et al., 2009). In the case of Swift J1753.5–0127, the bolometric luminosity (L) of the disk on MJD 56037 can be estimated to be $4.32\times10^{+37}$ erg s^{-1}, assumed that the distance is 8.5 kpc. The Eddington luminosity ($L_{\rm E}$) and the Eddington ratio ($L/L_{\rm E}$) can be obtained to be $1.25\times10^{+39}$ erg s^{-1} and 3.5%, assumed that the BH mass is 10 $M_{\odot}$. These results support that the state of Swift J1753.5–0127 changed from the low/hard to high/soft state and returned from the high/soft to low/hard state in the short-term. The values the Swift J1753.5–0127 distance and mass were reported to be from 5.9 kpc (Zurita et al., 2008) to 10 kpc (Cadolle Bel et al., 2007) and 6-10 $M_{\odot}$ (Reynolds et al., 2010). The variation of $L/L_{\rm E}$ is 1.6-5.8% The mass and the distance of various BHs is listed in table 2.1 and the values of Swift J1753.5–0127 are typical for a LMXB.

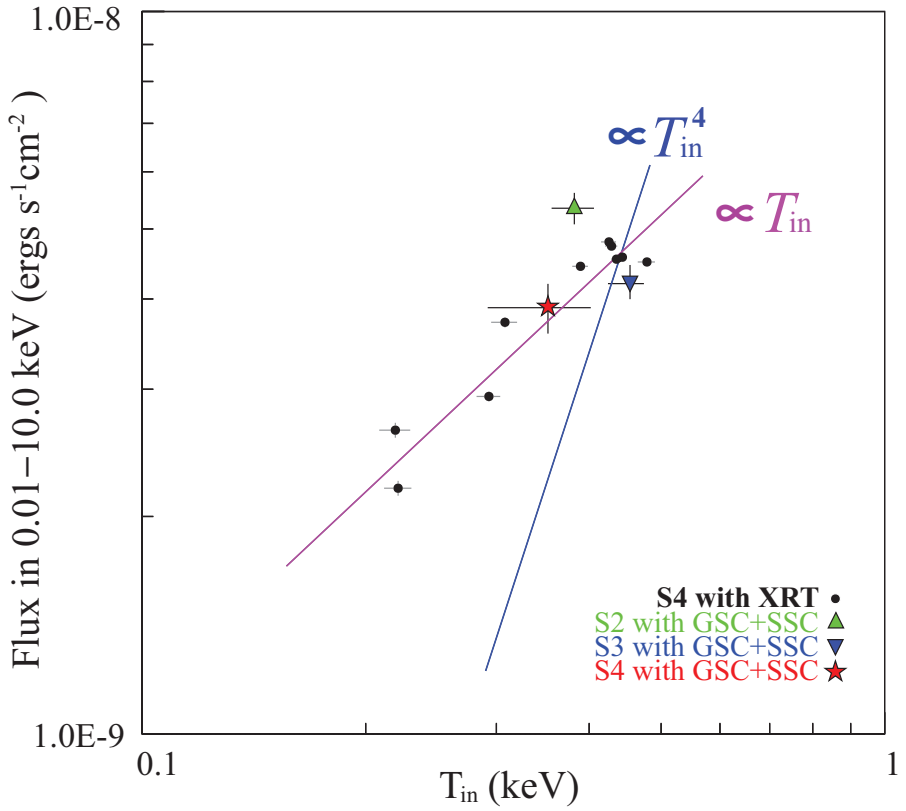

Figure 6.2: Relation between $F_{\rm disk}$ in the 0.01–10 keV energy range and $T_{\rm in}$ using the best-fit parameters for the short-term spectral softenings. Black points show the fitting results of S4 observed by the XRT. Green, blue, and red points show the fitting results for observations by the SSC and GSC in S2, S3, and S4, respectively. Magenta and blue lines show the powerlaw functions with an index of one and four, respectively.

6.4 The disk reaching to the ISCO

Because L/L_E is over 1.5% during the short-term softening, the high/soft state might be realized between MJD 56037 and 56047. $R_{\rm in}$ during the high/soft state typically reaches to and stay at the ISCO. $N_{\rm disk}$ obtained by the spectroscopy analysis was plateau in figure 5.10. By using the value of $N_{\rm disk}$ in the plateau, MJD 56037–56047, $R_{\rm in}$ is estimated as $R_{\rm in} \sim 70\pm3 \times (D$ / 10 kpc) $\times \cos^{-0.5} \theta$ km, where D is the distance to the source, and θ is the inclination angle. The true inner radius ($r_{\rm in}$) can be calculated as 1.18 $R_{\rm in}$ assuming the friction free boundary condition (Kubota et al., 1998) and a color hardening factor of 1.7 (Shimura & Takahara , 1995). Assuming that D is 8.5 kpc (Reynolds et al., 2010) and θ is 45°, we obtained $r_{\rm in} \sim$82 km. When the BH mass is 10 $M_\odot$ (Reynolds et al., 2010) and the BH does no spin, $r_{\rm in}$ would be close to the ISCO; although this is not yet conclusive due to the large uncertainties of the mass, θ and D. Reynolds et al. (2010) implied that the BH mass is smaller than 10 $M_\odot$ and the distance is larger 8.5 kpc. Although the parameters of MJD 56041 are close to those of the high/soft state, the observation exposure in the softening event is not enough to investigate the relation between $F_{\rm disk}$ and $T_{\rm in}$.

6.5 The change of mass accretion rates

Assuming that the accretion disk can be explained by the standard accretion disk model, $T_{\rm in}$ can be written as follows,

$$T_{\rm in} = \left(\frac{3GM\dot{M}}{8\pi R_{in}^3 \sigma_{\rm B}} \right)^{1/4}, \tag{6.1}$$

where the G is the gravitational constant, the $\dot{M}$ is mass accretion rate, the M is the BH mass, the $\sigma_{\rm B}$ is the Boltzmann constant. $T_{\rm in}$ is proportional to $R_{\rm in}$ as $T_{\rm in} \propto {R_{\rm in}}^{-3/4}$ when the $\dot{M}$ is constant. The relation between $T_{\rm in}$ and $R_{\rm in}$ of XTE J1817-330 were reported (Cabanac et al., 2009). During the low/hard state, the plots have the trend of $T_{\rm in} \propto {R_{\rm in}}^{-3/4}$. On the other hand, the trend of the high/soft state did not obey the equation of $T_{\rm in} \propto {R_{\rm in}}^{-3/4}$ and the $T_{\rm in}$ dramatically increased as $R_{\rm in}$ decreased. The index is much lower ($< -4/3$) and $T_{\rm in}$ heated up by the increase of $\dot{M}$. The $\dot{M}$ during the low/hard state was constant and started to increase when state changes from the low/hard to high/soft state.

We plot the relation between $T_{\rm in}$ and $R_{\rm in}$ in figure 6.3. We fit the powerlaw model to the data during the short-term softening and the value of the index is obtained to be -0.64±0.03. When the state changes from the low/hard state into the high/soft state, $R_{\rm in}$ and $\dot{M}$ are changed at same time. The index is larger than $-3/4$ and minus, which means that $\dot{M}$ decrease as $R_{\rm in}$ decrease. The value of $\dot{M}$ can be changed by the bolometric luminosity of the accretion disk because of the radiation pressure. The L on MJD 56037 can be estimated to be 4.32E+37 erg s^{-1}, assuming that the distance is 8.5 kpc and the BH mass is 10 $M_\odot$. Cabanac et al. (2009) reported that $\dot{M}$ switched when $L/L_{\rm E}$ is over $\sim$1.5%. The orbital periods of the binary system of Swift J1753.5–0127 is reported to be 3.23 hrs and is the third shortest of all the BHBs (Zurita et al., 2008). The efficiency of the accretion is reported to be generally lower and thus the luminosity is also lower during the high/soft state (Knevitt., 2014). The slightly change of the luminosity may be change $\dot{M}$ and define the periods of the short-term softening.

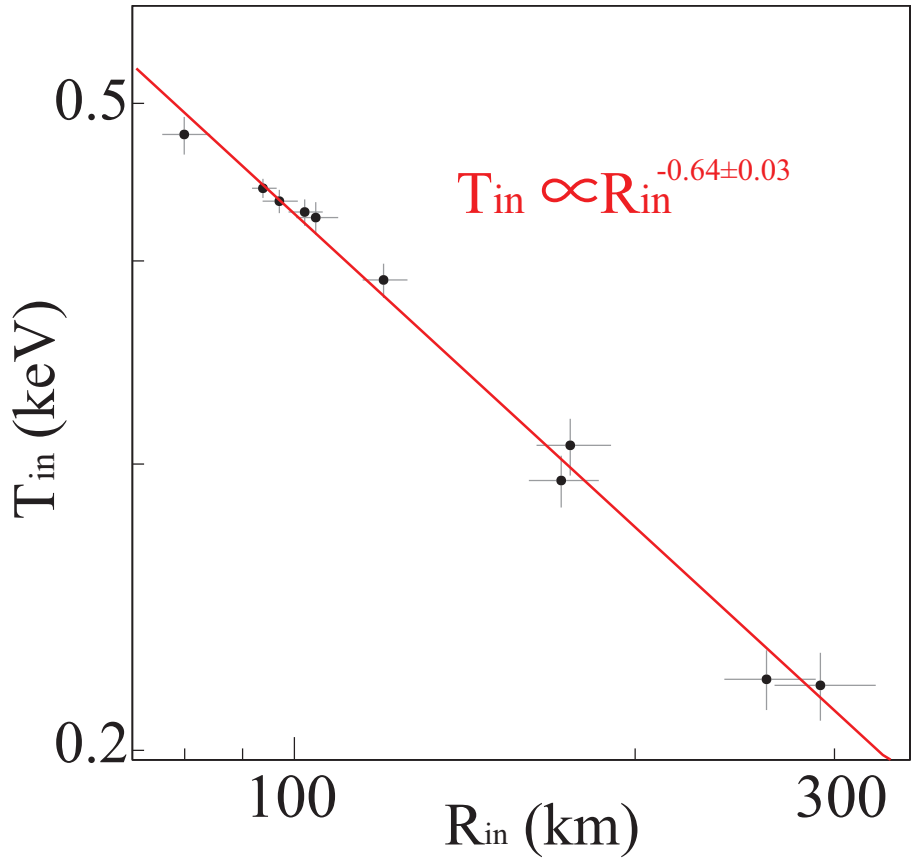

Figure 6.3: The relation between the $T_{\rm in}$ and $R_{\rm in}$. The red line show the powerlaw models with the index of -0.64±0.03.

6.6 Future works

We revealed that the state of the X-rays spectra change during the short-term softening. Fitting continuum model to the X-rays spectrum could offer the radiation parameters, but we could not conclude the structure transition of the accretion disk. The information of the geometry variation of the accretion disk and the Corona during the state change could reveal the advection of the energy and materials between the disk and Corona. The X-rays polarization may open window to reveal the disk and Corona geometrical structures (§ 2.8.1).

In the future, the *PRAXyS* mission which is the first astronomy satellite for the X-rays polarimetry may observe Swift J1753.5–0127. To detect the polarization fraction of 1%, the exposure is needed to be over 300 ksec. The *PRAXyS* polarimeter can observe the X-rays polarization of the short-term softening. Because the X-rays polarization fraction is depending on the inner radius (§ 2.8.1), the structure transition will reflect the X-rays polarization and degree as a function of X-rays energy.

Chapter 7

CONCLUSION

We have analyzed the data on the X-ray binary BH Swift J1753–0127 to reveal the origin of the short-term (about 20 days) flux variation appeared in the 15–50 keV energy band. We analyzed the data taken with *MAXI* and *Swift*, mainly focusing on the data below 2 keV, and obtained the following results and conclusion.

1. During the short-term flux variation, we discovered the increase of flux in the 0.7–1.7 keV (short-term softening), concluding that the flux variation originated in the state transition rather than the eclipse.

2. The X-ray spectra in the state transition were reproduced by a multi-color disk black-body component of the accretion disk and its inverse-Comptonized component. The temperature (T_{in}) and the energy flux ($F_{\rm disk}$) of the accretion disk changed from 0.48 to 0.2 keV and 4.8×10^{-9} to 2.2×10^{-9} erg s^{-1} cm^{-2}, respectively. The derived inner most radius of the accretion disk ($R_{\rm in}$) from $T_{\rm in}$ and $F_{\rm disk}$ at the peak of the short-term softening was closest to the black hole, while that at the end of the softening was far.

3. The data showed $F_{\rm disk} \propto T_{\rm in}^{0.97\pm0.02}$, not obeying the relation of the standard disk $F_{\rm disk} \propto T_{\rm in}^{4}$. This implies that $R_{\rm in}$ changed during the short-term softening.

We conclude that the short-term variation originated in the state transition from low/hard state to high/soft-like state immediately followed by the opposite transition.

REFERENCES

Abramowicz, M. A., Chen, X., Kato, S., Lasota, J.,, Regev, O., 1995, ApJ, 438, 37

Barthelmy, S. D., Barbier, L. M., Cummings, J. R., Fenimore, E. E., Gerhels, N., Hullinger, D., Krimm, H. A., Markqardt, C. B., Palmer, D. M., Parsons, A., Goro, S., Suzuki, M., Takahashi, T., Tashiro, M., & Tueller, J, 2005, Space Sci. Rev., 120, 143

Bardeen, M., J., Press, H., W., & Teukolsky, A., S., 1972, Apj, 178, 347

Bolton C. T., 1972, Nature, 235, 271

Burrows, N. D., Racusin, J., Morris, C., D., Roming, P., Chester, M., Verghetta, La, R., Markwardt, B., C., & Barthelmy, D., S., 2005, Atel #547

Cabanac, C., Fender, R. P., Dunn, R. J. H., KÖrding, E. G., 200 9, MNRAS, 396, 1415

Cadolle Bel, M. *et al.* 2007, ApJ, 659, 549

Corral-Santana, J. M., Casares, J., Muñoz-Darias, T., Rodríguez-Gil, P., Shahbaz, T., Torres, M. A. P., Zurita, C. & Tyndall, A. A., 2013, Science, 339, 1048

Cui, W., Heindl, A. W., Swank, H. J., Smith, M. D., Morgan, H. E., Remillard, R. & Marshall, E. F., 1997, ApJ, 487, 73

Cui, W., Feng, Y., X., Zhang, S., N., Bautz, M., W., Garmire, G., P. & Schulz, N., S., 2002, ApJ, 576, 357

Daikyuji, A., Yamauchi, M., Tsunemi, H., Kimura, M., Kitayama, H., Tomida, H., Matsuoka, M. & MAXI Team, 2010, Proceedings of 4th International MAXI Workshop, 'In Orbit Performance of the MAXISSC 1' Tokyo, Japan, 2010

Dotani, T., Inoue, H., Mitsuda, K., Nagase, F., Negoro, H., Ueda, Y.k Makishima, K., Kubota, A., Ebisawa, K., Tanaka, Y., 1997, ApJ, 485, 87

Durant, M., Gandhi. P., Shahbaz. T., Fabian. A., Miller. J., Dhillon, V., S., Marsh, T., R., 2008, ApJ, 682, 45

Esin, A., A., McClintock, J. E., Narayan, R., 1997, ApJ, 489, 865E,

Fabian, A. C., Rees, M. J., Stella, L., White, N. E., 1989, MNRAS, 238, 729

Frank, J., King, A., & Raine, D. J., 2002, Accretion Power in Astrophysics: Third Edition (Cambridge: Cambridge Univ. Press)

Han, S., & Kang, H., 2002, JKPS, 40, 820

Halpern, P., J., 2005, Atel #549

Kawaguchi, T., ApJ, 2003, ApJ, 593, 69

Kato, S., Fukuke, J., & Mineshige, S., 2008, Kyoto University Press, Black-Hole Accretion Disks Towards a New Paradigm

Kalogera, V., Baym, G., 1996, ApJ, 470, 61

Knevitt, G., Wynn, G. A., Vaughan, S., Watson, M. G., 2014, MNRAS, 437, 3087

Kozlowski, M., Jaroszynski, M. & Abramowicz M., 1978, A&A, 63, 209

Kuulkers, E. *et al.* 2013, A&A, 552, 32

Kuznetsov, S. I., Gilfanov, M. R., Churazov, E. M., Sunyaev, R. A., D'Yachkov, A. V., Khavenson, N. G., Novikov, B. S., Kremnev, R. S., Goldoni, P., Goldwurm, A., Laurent, P., Paul, J., Roques, J.-P., Jourdain, E., Bouchet, L., Vedrenne, G., 1999, AstL, 25, 351

Kubota, A., Tanaka, Y., Makishima, K., Ueda, Y, Dotani, T, Inoue, H. & Yamaoka, K., 1998, PASJ, 50, 667

Kubota, A., Done, C., 2003, MNRAS, 353, 980

Makishima, K., Maejima, Y., Mitsuda, K., Bradt, H. V., Remillard, R. A., Tuhoy, I. R., Hoshi, R. & Nakagawa, M., 1986, ApJ, 308, 635

Makishima, K. *et al.* 2000, ApJ, 535, 632

Gierliski, M., Zdziarski, Andrzej A., Poutanen, J., Coppi, Paolo S., Ebisawa, K., Johnson, W. Neil, 1999, MNRAS, 309, 496

Markert, T. H.; Clark, G. W.; Lewin, W. H. G.; Schnopper, H. W.; Sprott, G. F, 1973, IAUC, 2483, 1

Matsuoka, M. *et al.* 2009, PASJ, 61, 999

Mihara, T. *et al.* 2011, PASJ, 63, 623

Miller, J. M., Homan, J. & Miniutti, G., 2006, ApJ, 652, 113

Mitsuda, K. *et al.* 1984, PASJ, 36, 741

Nakahira et al., 2013, JSSIJ, 2, 29

Nandi, A., Debnath, D., Mandal, S., Chakrabarti, S., K., 2012, A&A, 542, 56

Negoro, H. *et al.* 2009, Atel #2341

Negoro, H. *et al.* 2010, Atel #2873

Negoro, H. *et al.* 2011, Atel #3300

Negoro, H. and MAXI team, 4th international MAXI Workshop Proceedings, 2010, 63

Oda, M., Gorenstein, H., Gursky, H., Kellogg, E., Schreier, E., Tananbaum, H., & Giacooni, R., 1971, ApJ, 166, 10

Palmer, M. D., Barthelmey, D. S., Cummings, R. J., Gehrels, N., Krimm, A. H., Markwardt, B. C., Sakamoto, T. & Tueller, J., 2005, Atel #546

Paczynski, B., 1974, A&A, 34, 161

Patterson, J., et al., 2005, PASP, 117, 1204

Ramadevi, C. M. & Seetha, S., 2007, MNRAS, 378, 182

Reis, R. C., Fabian, A. C., Ross, R. R. & Miller, J. M., 2009, MNRAS, 395, 1257

Remillard, R., A. & McClintock, Jeffrey, E. 2006, ARA&A, 44, 49

Reynolds, M., T., Miller, Jon, M., Homan, Jeroen, and Miniutti, Giovanni, 2010, APJ, 709, 358

Rybichi, B., G., and Ligthman, P., A., 1979, WILEY-VCH Verlag GmbH & Co. KGaA, Weinheim, Radiative Processes in Astrophysics

Sarkar, R., Chakrabarti, S. K. & Nandi, A., 2008, AIPC, 1053, 215-218

Schnittman, Jeremy, D., & Krolik, Julian, H., 2009, ApJ, 701, 1175

Shimura, T., and Takahara, F., 1995, ApJ, 445, 780

Shakura, N. I. & Sunyaev, R. A., 1973, A&A, 24, 337

Shaw, A. W. *et al.* 2013, MNRAS, 433, 740

Soleri, P. *et al.* 2013, MNRAS, 429, 2, 1244

Steiner, J., F., Narayan, R., McClintock, Jeffrey, E. & Ebisawa, K., 2009, PASP, 121, 1279

Steiner, J., F., McClintock, Jeffrey, E., Reillard, Ronald, A., Narayan, Ramesh & Gou, Lijun, 2009, ApJ, 701, 83

Sugizaki, M. *et al.* 2011, PASJ, 63, 635

Tamagawa, T.; Hayato, A.; Asami, F.; Abe, K.; Iwamoto, S.; Nakamura, S.; Harayama, A.; Iwahashi, T.; Konami, S.; Hamagaki, H, 2009, NIMPA, 608, 390

Tomsick, J., Nowak, M., Parker, M., Miller, J. M., Fabian, A. C., Harrison, F., Bachetti, M., Barret, D., Boggs, S. E., Christensen, F., Craig, W. W., Forster, K., Fuerst, F., Grefenstette, B., Hailey, C. J., King, A. L., Madsen, K., Natalucci, L., Pottschmidt, K., Ross, R. R., Stern, D., Walton, D., Wilms, J., Zhang, W., 2014, ApJ, 780, 10

Tomida, H. *et al.* 2011, PASJ, 63, 397

Torres, M. A. P., Steeghs, D., Garcia, M. R., et al. 2005a, ATEL 551

Torres, M. A. P., Steeghs, D., Blake, C., et al. 2005b, ATEL 566

Tsunemi, H., Tomida, H., Katayama, H., Kimura, M., Daikyuji, A., Miyaguchi, K., Maeda, K. & MAXI Team, 2010, PASJ, 62, 1371

Ueno, S., Matsuoka, M., Kawasaki, K., Tomida, H., Suzuki, M., Ishikawa, M., Adachi, Y., Itamoto, Y., Mihara, T., Kohama, M., Sugizaki, M., Nakagawa, Y. E., Yamamoto, T., Tsunemi, H., Kimura, M., Kawai, N., Morii, M., Sugimori, K., Yoshida, A., Yamaoka, K., Nakahira, S., Negoro, H., Ishiwata, R., Miyoshi, S., Ozawa, H., Nakajima, M., Ueda, Y., Isobe, N., Eguchi, S., Hiroi, K., Katayaymai, H., Ebisawa, K., 2009, Proceedings of Science, 011, The Extreme Sky: Sampling the Universe above 10 keV

Weisskopf, M., C., Cohen, G., G., Kestenbaum, H., L., Long, K., S., Novick, R., Wolff, R., S., 1976, ApJ, 208, 125

Webster, B. L, Murdin, P., 1972, Nature, 235, 37

Yoshikda, T., 2011, ISAS, A Statistical Study of Long-Term X-ray Variabilities of Ultraluminous X-ray Sources and Galactic Black Hole Binaries

Yoshikawa, A., Tamagawa, T.,Iwahashi, T., Asami, F., Takeuchi, Y.,Hayato, A.,Hamagaki, H., Gunji, T., Akimoto, R., Nukariya, A., Hayashi, S., Ueno, K., Ochie, A., and Oliveira, R., 2012, JINST, 7, C06006

Yuan, F., Quataert, E., and Narayan, R., 2003, ApJ, 598, 301

Zdziarski, A., A., Poutanen, J., Mikolajewska, J., Gierlinski, M., Ebisawa, K., Johnson, W., N., 1998, MNRAS, 301, 435

Zurita, C., Durant, M., Torres, M. A. P., Shahbaz, T., Casares, J. & Steeghs, D., 2008, ApJ, 681, 1458

Acknowledgement

This thesis for a doctoral dissertation were supported by many people. I will appreciate people who supports me to study the astrophysics. Especially My Ph. D. adviser, Dr. T. Tamagawa, has educated me for five years. I have been also supported by many scientist in the Tamagawa laboratory. The education for me is not their job but they have supported me to study the black hole and write my thesis. I will and must appreciate scientist who supports me, mentioning their names. It was very valuable experience for me to study with them or be educated by them.

Dr. Tamagawa encouraged me to study the instrument for X-ray polarization observation and to think logically the phenomenon. I have grew up to be a scientist with his education. I have freely study without any economic problem for three years, because I have been adopted as a research fellow of the Japan society for the promotion. When I wrote the document for the fellow application, he showed me the way to explain easily and clearly own study to reader.

Dr. S. Yamada is also adviser for my research fellow and doctoral dissertation. He led me to study black hole and to analyze the observation data. My the program and the data analysis are affected by his techniques. His character is calm and kind for teaching and leading me to study. It is particular time to study the black hole with Dr. Yamada. I have to apologize for not including the study of Cyg X-1 into this thesis.

Dr. S. Nakahira suggested me to analyze the short-term softening of Swift J1753.5-0127 and advised me to work for MAXI. The analysis results are summarized in the refereed paper of Publication of the Astronomical Society of Japan. He advised me to analyze the light curves in the energy range of 15-50 keV and 2-20 keV and to fit the model to the X-ray spectra.

Dr. H. Noda is a senior associate whom I talk frankly. In particular, his character is very open mind and gentle. His advice for my Ph. D. thesis is very objective and balanced. He actively supported me to study the black hole, to write the thesis and to make presentation. In particular, for last three months, he supported me to complete my thesis.

The education of Dr. A. Hayato, Dr. T. Yuasa and Dr. W. Iwakiri were very careful, fine and severe for constructing my thesis, for last a few months. Their education taught me what needs to obtain Doctor of Philosophy degree. If there was not their education, I could not obtain the degree. Teach of Dr. T. Kitaguchi were also very careful, fine and severe, but he never give up supporting me to study. Dr. S. Katsuda also suggests and supports me to study the astrophysics.

For nice peoples, I want to write her and him names with some memories. I have met many people supporting, helping, advising, leading, encouraging me. Dr. Chris Done is professor in the department of physics of the Durham university. She taught me to analyze the X-ray spectrum of Cyg X-1 when I stayed at the Durham university. Dr. Joanne Hill-Kittle, Dr. Jahoda Keith M., and Dr. Kevin Black are staff in the NASA's goddard space flight center (GSFC). Ms.

Hannah Marlowe is Ph. D. student of the Iowa university. They are co-worker of the GEMS mission. They help me to study the X-ray polarimeter in GSFC. Dr. A. Harayama is my senior associate since the astro club in the undergraduate. Mr. S. Nakamura is my senior associate and his character is open mind. Dr. S. Konami is my senior associate since the astro club in the undergraduate and leads tamagawa-labo students. Dr. T. Iwahashi is the senior associate who teach the techniques of experiments. Dr. F. Asami is also my senior associate since the astro club in the undergraduate and she drank with me sometimes. Ms. R. Yoshii is also my senior associate since the astro club in the undergraduate. Mr. M. Ota was an employee who joined the labo in the same year and competed amongst each other. Ms. Y. Takeuchi is my junior fellow in the labo. Mr. K. Kaneko is also my good junior fellow. I am sorry to have done some attack to you. You know, it was joke. Mr. K. Iwata, Mr. Y. Itaka, Mr. Y. Okamoto, Mr. K. Miyagawa, Ms. M. Kubota, Mr. Z. Endou and Mr. K. Nishida, are also good junior fellows. Ms. Judith A. Hamburg is a women who had lend me a room of her house, while I worked at NASA. There were many troubles during my visiting her house, but they were good memories. Dr. H. Otsu and Dr. K. Yoneda drank and ate, watching the football games on TV. The time was good and was relaxing.

For my girl friend, I thank you to your understanding and to your patience against my color.

For my parents, I will write my gratitude. My parents understand and receive my color and career. Sometimes, I do the selfish jerk that is impolite for my family and I am always doing stupid apology.

Last, I will thank for an X-ray astrophysics society and wish the development of astrophysics.

When I wrote this acknowledgment, I had brought back to memories of my lives in ”high energy astrophysics laboratory (tamagwa-labo) at RIKEN”. The reason why I choose this tamagawa-labo was for developing the X-ray polarimeter of GEMS mission and for observing world first X-ray polarization from black holes. The GEMS mission ”was” the project of the first satellite designed to observe the X-ray polarization of many kind of astro-objects. The GEMS mission was canceled in 2011 because the NASA’s budget is not enough to complete the mission. I should note that there was no big problem about our X-ray polarimeters. Before I get the bachelor degree of Tokyo University of Science (TUS), I wanted to choice the doctoral program on the radio astronomy at National Astronomical Observatory of Japan (NAOJ). I needed long time to decide to choice career options. When I passed the entrance test of NAOJ, my mother had highly recommend me the way because NAOJ was very famous for her. However, I choose developing X-ray polarimeter with Tamagawa-san, because the importance of the GEMS mission in the astrophysics was very interesting for me. At that time my mother was disappointed a little bit. At last, my mother have understood and finally celebrated my choice. There is a specially impressive memory of my choosing career for me. When I told my choice to members of Tamagawa-labo at meeting, he said ”I did not know that you choose my laboratory” with a laugh in spite of his instructions ”tell yoshikawa’s career choice at meeting”. I have wondered that this accident (or his rough handling) might make up good relationship between Tamagawasa-san and me. There were too much good memories to write in this acknowledgment.